Dissertation

Ultra-thin Germania and Germania-Silica films

Growth, structure and reactivity

Im Fachbereich Physik der Freien Universität Berlin
eingereichte Dissertation zur Erlangung des Grades
Doktor der Naturwissenschaften (Dr. rer. nat.)
vorgelegt von

Alexander Benedikt Fuhrich M.Sc.

aus Datteln

Berlin 2019

Die hier vorliegende Arbeit wurde am Fritz-Haber-Institut der Max-Planck Gesellschaft in der Abteilung Chemische Physik unter Anleitung von Prof. Dr. Hans-Joachim Freund, in der Spektro-Mikroskopie Arbeitsgruppe von Dr. Thomas Schmidt, angefertigt.

1. Gutachter: Prof. Dr. Hans-Joachim Freund
2. Gutachter: Prof. Dr. Paul Fumagalli

Tag der Disputation: 06.11.2019

Abstract

This thesis presents a specto-microscopical study on the preparation of ultra-thin germania and germania-silica films on a Ru(0001) single crystal support and the discussion of their chemical reaction with molecular hydrogen. The two-dimensional GeO_2 and GeO_2-SiO_2 films were investigated by synchrotron based spectro-microscopy applying microscopy, diffraction and spectroscopy.
For a calibration of the deposited germanium amount, the growth of germanium on bare Ru(0001) was studied in-situ by LEEM, LEED, XPEEM and XPS. The germanium films were grown at 540 K in UHV. This demonstrated that, at first, a (2x2) germanium layer is formed and further germanium growth leads to the formation of a coexisting (3x3) germanium structure. Afterwards a second layer is formed, however before the (3x3) phase is completely closed. Further germanium growth leads to the formation of three-dimensional germanium islands. Germanium grows at 540 K in UHV on bare Ru(0001) in a Stranski-Krastanov growth mode.
The germanium film oxidation was studied in real-time and in-situ. The formation of a partially closed GeO_2 layer on top of a closed GeO_2 monolayer was found. Furthermore the oxidation of a 0.6 nm thick germanium film is presented. As a result, it was found that a closed GeO_2 monolayer on Ru(0001) is formed and that excess GeO_x desorbs at temperature above 770 K.
Another part of this work is the preparation of ultra-thin mixed GeO_2-SiO_2 films on Ru(0001). Different preparation recipes are presented showing that the crystallinity of the initially deposited film has a significant influence on the final film. The addition of germania or silica to a crystalline film leads to the coexistence of two separated oxides. The non-connected germania desorbs at temperatures above 970 K. Different silica to germania ratios were prepared. An amount of nominal 0.5 ML germanium was dispersed in 1.5 ML silica matrix. Only crystalline germania-silica films could be prepared. Germania containing silica leads to lower crystallization temperatures compared to pure silica.
Finally the effect of hydrogen treatments on the GeO_2 and GeO_2-SiO_2 films were studied in real-time LEEM. Whereas hydrogen completely reduces the GeO_2 film. The reduced germanium segregates on the bare Ru(0001) surface.
The hydrogen treatment on the mixed GeO_2-SiO_2 films shows two steps. In the first step the hydrogen removes oxygen with a binding energy of 529 eV. This step is not visible in LEEM. In a second step the hydrogen treatment leads to a partial reduction of the germanium in the silica matrix, the silica is not reduced. However, the Si2p core level shifts by 0.2 eV. The GeO_2-SiO_2 films can be reoxidized. The reoxidized films are similar to the initial films. Furthermore, the low energy electron beam influences the chemical reaction and enhances locally the reduction of GeO_2 by hydrogen.

Zusammenfassung

In dieser Arbeit wird eine spektro-mikroskopische Studie über die Präparation ultradünner Germania und Germania-Silika Filme auf einer Ru(0001) Unterlage präsentiert und deren chemische Reaktion mit molekularem Wasserstoff diskutiert. Für diese Arbeit wurden zweidimensionale GeO_2 und GeO_2-SiO_2 Filme mit synchrotronbasierter Spektro-Mikroskopie untersucht, wobei Mikroskopie-, Beugungs- und Spektroskopiemethoden angewendet wurden.
Für eine Kalibrierung der aufgedampften Germaniummenge wurde das Wachstum von Germanium auf reinem Ru(0001) mit LEEM, LEED, XPEEM und XPS in-situ untersucht. Die Germaniumfilme wurden bei 540 K im UHV aufgewachsen. Dabei zeigte sich, dass erst eine (2x2) Germaniumstruktur gebildet wird und weiteres Germaniumwachstum zur Bildung einer koexistierenden (3x3) Struktur führt. Anschließend bildet sich eine zweite Lage aus, jedoch bevor die (3x3) Phase komplett geschlossen ist. Weiteres Germaniumwachstum führt zur Bildung von dreidimensionalen Germaniuminseln. Daher wächst Germanium bei 540 K in UHV auf reinem Ru(0001) in einem Stranski-Krastanov-Wachstum. Die Germanium Oxidation wurde in Echtzeit und in-situ untersucht. Es zeigte sich die Bildung von einer partiell geschlossenen Lage GeO_2 auf einer geschlossenen GeO_2 Monolage. Ferner wird die Oxidation einer 0.6 nm dicken Germaniumschicht gezeigt. Es zeigte sich, dass das überschüssige GeO_X bei Temperaturen oberhalb von 770 K verdampft und sich eine geschlossene GeO_2 Monolage auf Ru(0001) bildet.
Ein weiterer Teil dieser Arbeit betrifft die Herstellung ultra-dünner gemischter GeO_2-SiO_2 Filme auf Ru(0001). Es zeigte sich, dass ein entscheidender Einfluss auf den finalen gemischten GeO_2-SiO_2 Film die Kristallinität des zuerst aufgedampften Films ist. Das Hinzufügen von Germania oder Silika zu einem kristallinen Film führt zur Koexistenz zweier unabhängiger Oxide. Das nichtgebundene Germania desorbiert bei Temperaturen oberhalb von 770 K. Es wurden verschiedene Germania zu Silika Verhältnisse präpariert. Eine Germaniummenge von nominell 0.5 ML wurde auf 1.5 ML Silika verteilt. Es konnten nur kristalline Germania-Silika Filme hergestellt werden. Germania führt zu einer niedrigeren Silika Kristallisationstemperatur gegenüber reinem Silika.
Abschließend wurde an den GeO_2 und GeO_2-SiO_2 Filmen eine Wasserstoffbehandlung durchgeführt, die in Echtzeit in LEEM untersucht wurde. Die GeO_2 Filme werden durch Wasserstoff vollständig reduziert. Das reduzierte Germanium segregiert auf dem reinen Ru(0001). Die Wasserstoffbehandlung bei GeO_2-SiO_2 Filmen verläuft in zwei Schritten. Zuerst entfernt der Wasserstoff Sauerstoff mit einer Bindungsenergie von 529 eV. Dieser Schritt ist nicht sichtbar im LEEM. In einem zweiten Schritt wird das Germania in der Silikamatrix partiell reduziert. Das Silika wird hingegen nicht reduziert. Jedoch verschiebt sich das Si2p Kernniveau um 0.2 eV durch die Wasserstoffbehandlung. Die GeO_2-SiO_2 Filme können reoxidiert werden. Die reoxidierten Filme sind identisch mit den ursprünglichen Filmen. Des Weiteren zeigte sich ein großer Einfluss des niederenergetischen Elektronenstrahls auf die chemische Reaktion. Der Elektronenstrahl führt zu einer lokalen Verstärkung der Reaktion.

Contents

1 Introduction **1**

2 Spectro-microscopy **5**
2.1 The SMART microscope and LEEM III . . . 6
2.1.1 The SMART microscope . . . 6
2.1.2 Aberrations and space charge . . . 11
2.1.3 LEEM III . . . 11
2.1.4 Setup and vacuum . . . 13
2.2 LEED theory . . . 14
2.3 Photoeffect . . . 17
2.3.1 Theoretical aspects . . . 17
2.3.2 XPEEM and radiation effects . . . 21
2.4 Model systems and thin film growth . . . 22
2.4.1 Model systems for catalysis . . . 22
2.4.2 Thin film growth . . . 22

3 Germanium growth on Ru(0001) **25**
3.1 Ge on Ru(0001): LEED and LEEM comparison . . . 27
3.2 Adsorption of molecular oxygen on Ge/Ru(0001) at room temperature 37
3.3 Germanium deposition on 3O-(2x2)-Ru(0001) . . . 38
3.4 Interpretation . . . 42
3.5 Conclusion . . . 45

4 Ultra-thin GeO_2 films on Ru(0001) **47**
4.1 Formation of GeO_2 on Ru(0001) - in real-time . . . 47
4.1.1 Interpretation . . . 54
4.2 Oxidation of 0.6 nm thick germanium on Ru(0001) - a case study . . 56
4.2.1 Interpretation . . . 62
4.3 Germania on Ru(0001) . . . 63
4.3.1 Interpretation . . . 68
4.4 Conclusion . . . 69

5 Preparation and thermal stability of ultra-thin germania-silica films on Ru(0001) **71**
5.1 Germania with silica on top . . . 72
5.1.1 SiO_X on (2x2)-GeO_2 . . . 72
5.1.2 SiO_X on GeO_X/3O-(2x2)-Ru(0001) . . . 77
5.1.3 Interpretation . . . 81

5.2 Silica with germania on top 83
5.2.1 Preparation “A” and “B” 84
5.2.2 Preparation “C” 92
5.2.3 Low temperature crystallization of germania-silica at 820 K . 94
5.2.4 Interpretation 95
5.3 Conclusion 97

6 Effects of H_2 exposure on ultra-thin GeO_2 and GeO_2-SiO_2 films 99
6.1 Germania 101
6.1.1 Hydrogen treatment of germania 101
6.1.2 Interpretation 106
6.2 Germania-Silica 108
6.2.1 Hydrogen treatment of germania-silica 108
6.2.2 Reoxidation of germania-silica films 115
6.2.3 Interpretation 117
6.3 Conclusion 121

Bibliography 123

Curriculum Vitae 141

Selbstständigkeitserklärung 145

1 Introduction

Ultra-thin oxide films on metal single crystal supports enable an elegant approach to study insulating material compounds with electron based surface science methods [1]. Many different 2D materials can be prepared successfully and form hexagonal network structures like graphene [2], silicene [3] and germanene [4]. Two-dimensional compounds can be prepared like hexagonal boron nitride [5] or molybdenum disulfide [6]. Also 2D oxides have been studied, such as iron oxides [7] or silica [8] and germania [9]. Those well-defined thin oxide films can be used as model systems for catalysts with a reduced complexity compared to industrial catalysts [10]. Heterogeneous catalysis has been intensely studied since decades [11] [12]. The understanding of its fundamental mechanisms is still unsatisfactory due to their high complexity [11]. Industrial catalysts are mainly powders to increase the surface area. Furthermore mesoporous structures like zeolites are used for many chemical reactions [13]. For tuning of the chemical properties of mesoporous structures the control of the pore size is the important part [14]. New zeolite structures offer new chemical properties, therefore germanium containing zeolites are studied [15] [16] [17].

Analogous to silica, germania forms crystalline and vitreous structures [18]. The glass transition temperature of germania is much lower compared to silica [19]. Also mixed germania-silica glasses have been widely studied since decades, the refractive index and density increase approximately linearly with the germania mole fraction [20]. Germania-silica glass can be prepared by a sol-gel technique and drying of the gel [21]. The germania-silica glass consists of individual GeO_4 and SiO_4 tetrahedra [21]. The tetrahedral building units form a corner linked network [21]. The glass network consists of Ge-O-Ge, Si-O-Ge and Si-O-Si bonds [21]. The GeO_4 tetrahedral building units are similar to pure GeO_2 glass which leads to a misfit of the SiO_4 tetrahedral building units [21]. However, those structures are hard to study on an atomic level. In contrast to powders, single crystal surfaces under UHV (ultra high vacuum) conditions are very well-defined and accessible to theory and to surface science methods like STM, LEEM, LEED, XPS, IRAS and others [10]. The present work mainly uses the synchrotron based spectro-microscope SMART for experiments. This aberration corrected and energy filtered LEEM/PEEM instrument enables real-time and in-situ studies of conductive samples on a mesoscopic scale with a high surface sensitivity [22] [23], combining at the same location methods like LEEM, LEED, μ-XPS, XPEEM, angular-resolved PES [22].

The research of ultra-thin germania and mixed germania-silica films on metal supports is rather new. This work presents the first spectro-microscopic studies on

ultra-thin germania and germania-silica films on Ru(0001) surfaces. For the current thesis, detailed studies of silica on different metal single crystals and also germania films preceded. Therefore, the ultra-thin silica and germania films will be introduced briefly. The structures of the silica monolayer and bilayer are known for different metal supports [24]. On Mo(112) surface a silica monolayer grows in a c(2x2) structure with a long range order which was the first ultra-thin silica film on a metal support [25]. The properties of the silica depend strongly on the metal support. The silica bilayer can be prepared on different metal supports like Ru(0001) [26], Pd(111) [27] and Pt(111) [28]. On Ru(0001) the monolayer and the bilayer phases exist while on the Pt(111) and Pd(111) surface only the vitreous bilayer was found. The silica monolayer and bilayer differ by the interaction with the support, the monolayer is chemisorbed and the bilayer is physisorbed [26]. The well-ordered silica bilayer on Ru(0001) surfaces consists of two layers of six-member rings with two SiO_4 tetrahedral building units on top of each other [29]. This crystalline silica bilayer can be transformed by annealing into the vitreous phase [30] [31] [32]. The structural prediction of Zachariasen [33] could be proved by atomically resolved STM images of the vitreous silica on Ru(0001) [34]. The metal support influences the silica by the misfit [35] and its affinity to oxygen [36]. On the Ru(0001) surface the silica system has been intensely studied with different methods like STM [8], AFM [37] and IRAS [8]. On a mesoscopic scale the silica mono- and bilayer were studied by LEEM, LEED, XPEEM and μ-XPS [26]. In 2018 a new silica polymorph on Ru(0001) was found [38] with a very complex LEED pattern. This so called “zigzag” phase is partially chemisorbed and partially physisorbed to the substrate [38]. Further details of the silica system can be found elsewhere in [26] [39].

A possible vitreous ultra-thin germania-silica phase would improve the understanding of the crystalline-vitreous transition and may have a different ring-size distribution compared to vitreous silica and germania bilayer films. Here atomically resolved measurements on a possible vitreous germania-silica film are required. However the activation energy for the crystalline-vitreous transition can be determined by spectro-microscopy, according to the measurements for silica [32].

Ultra-thin germania films can be seen as an analogue to silica films because of the similar structural and chemical properties [19]. The structure of a germania monolayer on Ru(0001) was studied with STM and LEED-IV and completed by DFT calculations [9]. The found structure is similar to the silica monolayer but the orientation of the tetrahedral building unit is rotated by 30°[9]. Two silica tetrahedral building units are facing each other and form a perfect hexagon where the germania tetrahedral building units are rotated by 30°with respect to each other. The position of the germanium atoms is similar to those of the silicon atoms[19]. Each six member ring of germania contains an oxygen atom on the ruthenium surface [9]. The interfacial oxygen can be tuned for silica films on Ru(0001), the O-rich and O-poor silica [32].

The structure of the germania bilayer was calculated by DFT and the coexistence of the germania mono- and bilayer on Ru(0001) was observed by STM [19]. The crystalline bilayer and monolayer of germania show a (2x2) LEED pattern [19] and the silica mono- and bilayer as well [26]. DFT calculation predicts a lower stability for the germania bilayer structure compared to the silica bilayer [40]. The germania bilayer structure differs from the structure of the silica bilayer by a larger variation of the Ge-O-Ge bond angle [40] [19]. This tendency can be found by comparing the Ge-O-Ge angular distribution of germania glass with the Si-O-Si angular distribution of silica glass [19]. The two germania GeO_4 tetrahedral building units are not pointing with 180°with respect to each other [19] like in the SiO_4 tetrahedral building units. This leads to a buckling of the germania bilayer film [19].

Silica is a support for catalytically active materials [41]. Ultra-thin silica films with catalytically active materials are model systems for heterogeneous catalysts [42] [43]. Mixed ultra-thin germania and germania-silica films are model systems for silica-supported germania catalyst. Germanium dioxide is used as a catalyst for the PET (polyethylene terephthalate) synthesis [44]. Ultra-thin models were prepared with Al containing silica on Ru(0001) [45] and with transition metals like Ti [46] and Fe [47] [48]. As model systems for zeolites, iron silicates have been studied with different surface science methods like LEEM/PEEM [48], XPS [48] and STM [47]. Chromium was added to ultra-thin silica films as a direct surface science model for the Phillips (Cr/SiO_2) catalyst [43]. The Phillips (Cr/SiO_2) catalyst is used in the large-scale production of polyethylene [49]. The mixed silica films differ by structure and chemical properties. Aluminum replaces silicon atoms according to Lowenstein‘s rule [50]. In contrast to the homogeneous aluminum distribution, iron oxide forms a FeO like bottom layer [48]. Ti containing silicates segregate into a pure silicate and Ti-silicate phase [46].

Spectro- microscopy can be used for studying surface reactions [51] [52] [53] [54]. The formation of water in physically confined space, underneath the silica bilayer, was studied by spectro-microcopy [55], TPD and IRAS [56]. Furthermore, a theoretical study of Marx [57] predicts that chemical reactions in physically confined space are independent of the material used for the walls producing the confinement. Germania would be a good candidate for the chemical modification of the silica bilayer to prove this statement. The structural properties of silica and germania show only small differences [19]. However, germania and silica have different activation energies for the reduction by hydrogen. The activation energy for the GeO_2 reduction by hydrogen is 18.4 kcal/mol [58] in contrast to 85 kcal/mol for SiO_2 [59]. During the hydrogen treatments of a silica bilayer, the silica is not reduced by the hydrogen, but the interfacial oxygen is removed [55]. In contrast, for germania a reduction is expected under similar reaction conditions used in [55]. For the mixed germania-silica films a different behavior between pure germania and silica could be expected, e.g. due to the implementation of Ge into the Silica matrix, the mixed film might be inert to hydrogen.

2 Spectro-microscopy

In this chapter a theoretical and experimental overview of the used experimental techniques and the fundamental physical effects is presented. The Low-Energy-Electron Microscope (LEEM) was invented in the early 1960s [60] [22]. The LEEM technique is based on work of the 1930s, the thermionic electron emission microscopy (TEEM), the photo emission electron microscopy (PEEM) and the mirror electron microscopy (MEM) [22]. This microscopy approach was developed parallel to the transmission electron microscopy (TEM) and secondary electron microscopy (SEM) which were developed by Ernst Ruska and co-workers [22]. By the development of UHV techniques in the 1960s, a new view of surface science was opened and it was possible to study clean surfaces [22]. This afforded the rise of surface science and LEEM/PEEM technique [22]. The x-ray photo emission electron microscopy (XPEEM) was developed after the synchrotrons of the second and third generation were available with intense soft x-rays [22]. By using XPEEM, the chemical information of a selected area can be received [22]. By LEEM/PEEM, it is possible to study surfaces with a high surface sensitivity and large field of views in the micrometer range [22]. The high surface sensitivity is caused by inelastic mean free path length of the used electron energy according the universal curve [22]. Every LEEM microscope can image both the real and the reciprocal space [22]. By combining real space and reciprocal space imaging, the experiment contains information about the structure and morphology of the sample [22]. By using photoelectrons, the chemical information of a selected area can be received additionally [22].

In LEEM and LEED the surface is illuminated by low energy electrons with a possible kinetic energy range of 0 - 1000 eV, typically 0 – 70 eV, where the reflectivity is reasonable high [22]. The illumination is perpendicular to the surface, also the reflected beam used for imaging (so-called “bright field mode”) [22]. The sample surface must be conductive to avoid charging [22]. A rough surface would lead to distortions of the image because the reflected electrons will be reflected at different angles and the electric field in front of the surface will become inhomogenous [22]. These are main limitations for the sample system. For PEEM the photon source has a main influence on the image quality [22]. A high flux photon source is required; therefore an undulator insertion device at the synchrotron light source of the Helmholtz Center Berlin for Materials and Energy (HZB) is used whereby the photon energy is tunable [61].

The present work was done with two microscopes: The high resolution SMART (Spectro- Microscope with Aberration correction for many Relevant Techniques) microscope of the Fritz-Haber-Institute installed at the BESSY II synchrotron light source and a commercial "ELMITEC LEEM III" microscope (without aberration correction and energy filter).

2.1 The SMART microscope and LEEM III

2.1.1 The SMART microscope

The SMART microscope is a aberration corrected spectro-microscope with an unique Ω type energy filter with an energy resolution of 180 meV [61]. The lateral resolution of the SMART microscope is 2.6 nm in LEEM [62] and 18 nm in XPEEM [63]. A comparable lateral resolution is also reached by other aberration corrected and energy filtered spectro-microscopes [64]. The worse lateral resolution in XPEEM can be explained by a space charge effect due to the high peak intensity because of the short pulsed structure of the exciting x-ray beam [63]. The SMART microscope combines imaging, spectroscopy and diffraction modes in one setup [61]. The operating modes of the SMART microscope can be divided into two groups depending of the used electrons [61]: the first group is based on photoemission and the second group by imaging reflected and scattered electrons. The first group includes X-ray photo emission electron microscopy (XPEEM), (micro-spot-) x-ray photo emission spectroscopy (μ-XPS) mode and angular resolved photo emission spectroscopy (ARPES). Furthermore also photoelectron diffraction (PED) is possible by imaging the k-space [22]. By using synchrotron light and tuning the polarization of the light more imaging modes are possible. The photon energy and the polarization of the synchrotron radiation can be set by the undulator and the monochromator. By scanning the photon energy at different polarizations and detecting the electrons at the secondary electron edge, the near edge x-ray absorption fine structure (NEXAFS) of an element can be measured [22]. NEXAFS allows the measurement of the orientation of a molecule on the surface [22]. For magnetic samples, x-ray magnetic circular dichroism (XMCD) can be observed [22].
For the second group: the sample is illuminated by electrons from the electron gun [61]. In the (bright-field) LEEM mode the 00 beam of the LEED pattern is imaged [22]. By imaging the reciprocal space, the LEED pattern of the sample is observed [22]. It is also possible to image with superstructure spots of the LEED pattern by tilting the electron beam, the so-called "dark field LEEM". By using an aperture in the electron gun, a specific area can be selected. With this selection, a LEED pattern of a micrometer size area can be measured (μ-LEED). A widely used technique is the measurement of IV- curves (intensity-voltage, LEED-IV, LEEM-IV). For LEEM-IV, the (local) reflectivity of the sample is measured depending on the kinetic energy of the electrons (using one selected LEED spot) and thereby of the wavelength of the electrons according to the wave - particle dualism [65] [22]. An additional technique is the spot profile analysis of LEED spots (SPA-LEED) [66].

Figure 2.1 shows a scheme of the SMART microscope. The microscope can be separated in different parts. The first part is the objective with the sample and the magnetic objective lens. In the objective lens there are deflectors and stigmators. The next element is an electrostatic lens with a deflector in front of the beam separator. The sample is illuminated by low energy electrons from the electron gun or by monochromatic soft x-rays from the synchrotron. In the case of the illumination by photons, the emitted electrons from the sample are accelerated through the objective lens. The electron are deaccelerated towards the sample and after the reflection the electrons are accelerated.

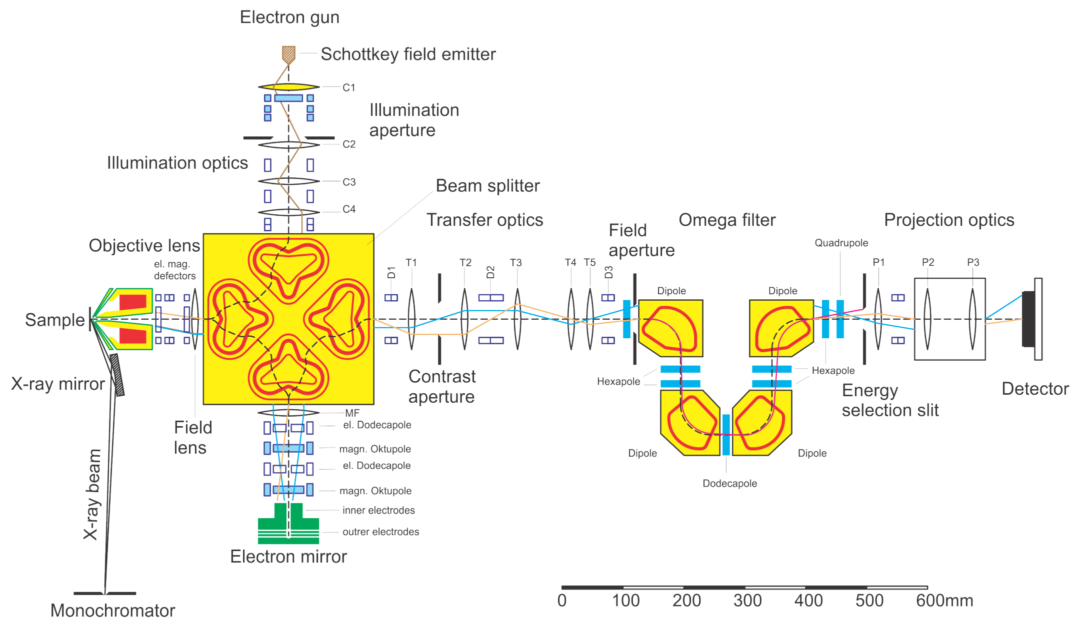

Figure 2.1: Sketch of the SMART spectro-microscope. The sample is illuminated by x-rays from the synchrotron or by electrons from the electron gun. The emitted or reflected electrons are moving through the objective lens and the unique beam splitter to the tetrode mirror. After the mirror, which compensates the spherical and chromatic aberration, the electrons are moving through the transfer optics to the Ω- energy filter and imaged on the screen (according to [67]).

The second part is the beam splitter. The beam splitter of the SMART microscope is very unique. The special shape and arrangement of the coils lead to an aberration-free transmission up to the second order [68]. This type of an electron beam splitter is self-compensating for the expected aberrations [68]. The transmission is free of dispersion up to the first order [68]. The dispersion free transmission is important otherwise beams with slightly different energies are not illuminated on the mirror axis [68]. The reflected electrons are transmitted again through the beam splitter.

The third part is the tetrode electron mirror for the aberration correction. The tetrode electron mirror compensates the spherical aberrations, caused by acceleration of the electrons between the sample surface and the objective lens and rotational symmetry of the objective lens [69]. The mirror consists of several electron optical

elements, such as electrostatical dodecapoles and magnetic octupoles, for deflection of the electron beam and for the correction of the astigmatism [69]. The electron mirror itself consists of three electrodes u0 to u2 And the lens u3 is also part of the mirror. The back electrode u0 produces a spherical field and the potential of u0 must be higher than the potential of the sample for providing the reflection of the electrons. The focusing is done by the electrodes u1 and u2. The electron mirror images the image plane back to the beam splitter edge and makes a 1:1 image [69]. The backfocal plane is imaged to the mirror plane. The mirror introduces spherical and chromatical aberrations with the opposite sign to compensate the aberrations of the objective lens [69].

The fourth part is the transfer optics [70]. It consists of five electrostatic lenses T1 – T5 with associated deflectors. The transfer optics images the back focal plane to the contrast aperture plane. Behind the first transfer lens T1 there is the back focal plane of the objective lens with the contrast aperture. By imaging the back focal plane of the objective lens, the reciprocal space is imaged. Also the magnification is change by the transfer optics. The transfer optics images the sample to the fixed entry image plane of the energy filter and also the back focal plane into the image slit plane of the energy filter. This is required for the different imaging modes of the microscope.

Behind the fifth transfer lens, there is the Ω energy filter [71]. The energy filter consists of four magnetic dipole elements, six hexapoles, one dodecapole (used as two quadrupoles and one hexapole) and finally two quadrupoles (to defocus the dispersive plane perpendicular to dispersion direction) [71]. In the dispersive plane of the Ω energy filter, there is a slit for selecting the energy of the electrons. The symmetry of the Ω energy filter eliminates second order aberrations [72]. The dispersion of the Ω energy filter is 35 μm/eV [22] and the energy resolution is 180 meV [61]. For the XPS mode the dispersive plane is imaged, therefore an aperture in the image plane in front of the Ω filter is necessary which on the one hand limits aberration and on the other hands allows for selection of the probed surface area. The design of the Ω energy filter does not affect the image quality [71].

Behind the Ω filter there is the projector, consisting of three electrostatic lenses. The imaging system is a two channel plates combined with a phosphorus screen and a fast CCD camera. The advantage of this image system is the fast image acquisition, so it is suitable for wobbling lenses. A major disadvantage is the noise of the detector and the bypassed electron detection. The electrons from a sample are amplified by the channelplates and converted into photons at the phosphorus screen [22]. The light is detected by the CCD camera and converted again into an electrical signal. However, direct electron detection is possible [73]. The main advantage of the direct electron detector is the outstanding sensitivity and the low noise level, but presently the detector is slow compared to the used channelplates and the detector are not bakeable which is unfavorable for UHV [73].

The fifth part is the electron gun. The electron source is a Schottky field emitter with an energy spread of around 0.3 eV [22]. A narrow energy spread is important to minimize the chromatic aberration even though it is corrected by the electron mirror. The Schottky field emitter is a ZrO coated W(100) tip that is heated to 1800 K [22]. In front of the source there is the illumination optics consisting of three electrostatic lenses and deflectors. The illumination must be parallel and perpendicular to the surface. For parallel illumination, the electron beam is focused in the back focal plane of the objective lens that is on the illumination side of the beam separator. Directly behind the extractor there is an aperture for selecting a specific area on the sample for μ-LEED.

The SMART microscope operates at -15 kV. The sample potential is -15 kV and the microscope is on ground potential. The electrons are very slow on the sample surface (0 - a few 100 eV). The electrons in the imaging column are on -15 kV except of the mirror. If the sample potential is higher or equal to -15 kV plus the work function difference between sample and field emitter, the electrons cannot penetrate the sample and are reflected in front of the surface. All electrons are reflected because of the missing inelastic scattering; this imaging type is called mirror electron microscopy (MEM) and it is very sensitive to local work function changes, especially at the MEM to LEEM transition. At the MEM-LEEM transition a part of the electrons has enough energy to penetrate into the crystal potential, leading to a reduction of the reflected intensity; so slight variations of the work function are visible. If the electron energy is higher than the potential of the sample, the electrons penetrate and interact with the sample. A part of the electrons are scattered inelastically. For LEEM, only the elastically reflected electrons are imaged in the bright field LEEM mode. The ratio between reflection and inelastic scattering depends on the electron energy, the crystal structure and the electronic structure of the sample. This dependency can be measured and plotted as the so-called LEEM-IV curves. Only electrons at 15 keV pass the energy filter. The acceleration in the homogeneous electric field in front of the sample leads to non-moving spots in the LEED pattern during changing the sample potential, i.e. variation of the kinetic electron energy.

The photo emission experiments were performed at the synchrotron radiation facility BESSY II of the Helmholtz Zentrum für Materialien und Energie (HZB). The BESSY II design is an electron storage ring of the third generation and optimized for the generation of soft x-ray synchrotron light. [74] The design is based on an electron source and a linear accelerator (LINAC) as a pre accelerator for the electrons [74]. The LINAC consists of cavity resonators [74]. In the cavity there is a standing high frequency electromagnetic wave which amplifies the electromagnetic field gradient for accelerating the electrons. The frequency of the cavity defines the temporal pulse length of the electron bunches [74]. The accelerated electrons are deflected into the synchrotron. In the synchrotron, the electrons are accelerated to the final energy (at BESSY II 1.7 GeV) [74]. Afterwards the electrons are deflected into the storage ring where undulators and bending dipole magnets are installed as sources for synchrotron light. Hexapoles and quadrupoles focus the electron beam.

The electron beam consists of bunches, the reason for the pulsed synchrotron light. A light pulse takes 20 picoseconds. These bunches are continuously losing electrons due to intrabeam interactions and collisions. The BESSY II synchrotron is normally operated in the so-called "top-up mode" with a nearly constant ring current [74]. In the top-up mode the lost electrons in the storage ring are refilled. This mode has the advantage to the user that the intensity of the x-rays is constant. The SMART microscope is located at an undulator source with a micrometer spot on the sample. The x-ray spot size on the sample surface is 30 μm $\times$ 10 μm. The undulator is a device of permanent dipole magnets in which the static magnetic field alternates along the length of the undulator. The electrons are forced to an oscillating trajectory. At the turning point of the oscillating trajectory, the synchrotron light is emitted. The light is tangentially emitted. Due to the periodicity of the undulator, the light is amplified by interference and so the light is very intense, coherent and nearly monochromatic. The wavelength of the light is aligned by the distance of the upper and lower array. The polarization is tuned by the shift of the upper and lower array [74]. In the undulator spectrum, there are different harmonics, but only odd harmonics give intensity. Higher harmonics give higher photon energies but lower intensities. To monochromatize the synchrotron light a plane grating monochromator (PGM) is used [74]. There are two different gratings available with different energy resolutions and photon fluxes. The final alignment of the beam is done by a refocusing mirror in front of the measurement chamber. A detailed overview of the properties and applications of synchrotron radiation can be found in [74].

The time structure of the light pulses leads to pulsed electron bunches with the same time structure in the microscope [63]. These electron bunches cause a space charge effect in the aberration corrector [63]. In the aberration corrector, which is a tetrode mirror, the electrons are reflected so that the spherical aberration of the objective lens is corrected [63]. If the electron density in space and time is too high, there is an intrabeam interaction that leads to a blurry image [63]. In the operation of the microscope, it is necessary to reduce the photon flux as much as possible to avoid this effect but still having enough intensity. A low photon flux reduces also beam damage effects. In contrast to the pulsed electrons in XPEEM the electron distribution in LEEM is continuous which avoids the space charge effect [63].

2.1.2 Aberrations and space charge

According to Scherzer all space charge free electron lenses with a rotational symmetry have always spherical and chromatic aberrations [75]. These aberrations are limiting factors of the resolution of all electron microscopes. In 1946, Scherzer published several proposals to overcome these aberrations [76]. A spherical aberration corrected electron microscope has a high lateral resolution combined with a higher transmission. A larger angle is accepted for a sharp image. Therefore, it is possible to use larger apertures for the same sharpness of the image in comparison to a non-corrected microscope. The resolution limit of an electron microscope is described by [72]:

$$d = \sqrt{d_d^2 + \frac{d_s^2}{4} + d_c^2} \tag{2.1}$$

Where d_s and d_c are the radii of the disks of confusion [72]. The factor $d_d = 0.61\lambda/\sin\alpha$ is described by the diffraction limit [72]. The spherical and chromatic aberrations are corrected simultaneously by the tetrode mirror of the SMART microscope [72] [69]. The design of the tetrode mirror was developed by Preikszas and Rose [69]. The Omega filter is correcting up to the second order aberration[72]. The overall correction is higher. For the spherical aberration the correction is [72]:

$$d_s^{(5)} = C_{SS} \sin^5 \alpha \tag{2.2}$$

And for the chromatic aberration [72]:

$$d_C^{(3)} = C_{CC} \left(\frac{\Delta E}{E}\right)^2 \sin\alpha \tag{2.3}$$

The overall correction of the SMART microscope for the spherical and chromatic aberration is [72]:

$$d_{SC}^{(4)} = C_{SC} \frac{\Delta E}{E} \sin^3 \alpha \tag{2.4}$$

The aberration correction leads to a higher lateral resolution and transmission [72] [63], which can decrease the acquisition time.

2.1.3 LEEM III

The experiments of this work were partially performed at a commercial "ELMITEC LEEM III" microscope. Therefore, this microscope type is briefly presented. Figure 2.2 shows a scheme of the LEEM III microscope. The basic design was suggested by Veneklasen and Telieps / Bauer proved the design [77] [22]. The microscope does not have an aberration corrector and an energy filter. Figure 2.2 shows a scheme of the "LEEM III" microscope. On the left side, there is the electron gun with a Schottky field emitter and three magnetic electron lenses C1-C3. The magnetic Y-shape 60° beam splitter is in the middle in front of the objective lens (OL) and the sample.

The reflected electrons are transmitted through the beam splitter. The imaging column consists of five magnetic electron lenses where P1 and P2 is the projector.

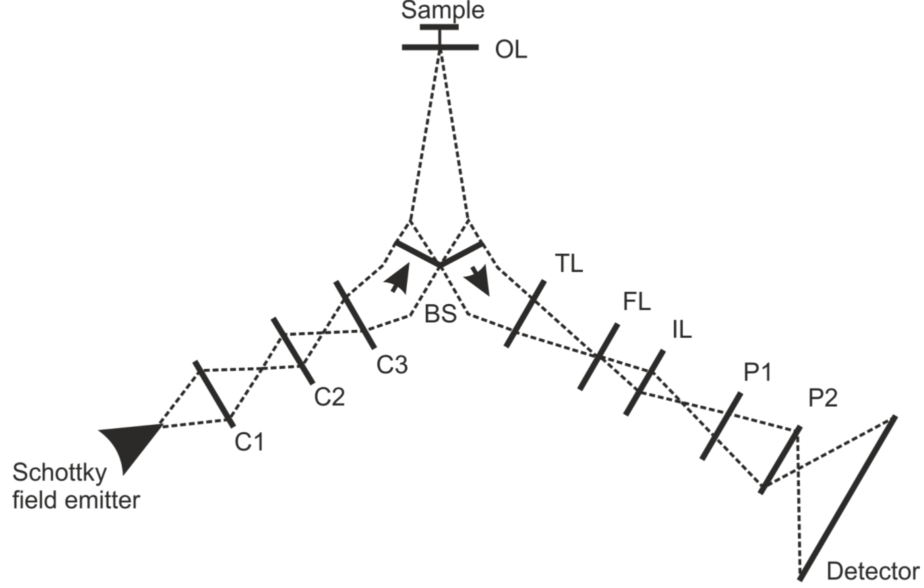

Figure 2.2: Scheme of the "LEEM III" microscope. On the left site is the electron gun with a Schottky field emitter and the lenses C1-C3. The beam splitter (BS) is magnetic Y-shape type. The sample is illuminated by the elctrons through the objective lens (OL). The imaging column consists of the lenses TL-P2. The image is projected (P1-P2) to the detector.

The last lens C3 focuses the electron beam into the back focal plane of the objective lens for a parallel illumination of the sample. The mirrored back focal plane is behind the transfer lens TL where the contrast aperture is located. The imaging column consists of five magnetic lenses.

The lateral resolution of the LEEM III microscope depends on the used voltage. The current I for the magnetic lenses and deflectors at different operating high voltages (U_{OLD} and U_{NEW}) can be approximately calculated by the following equation (neglecting the remanence of the coils):

$$I_{NEW} = I_{OLD}\sqrt{\frac{U_{OLD}}{U_{NEW}}} \tag{2.5}$$

A very useful voltage is 15 kV. This voltage provides a good compromise between resolution and stability. When exposing the sample to reactive gases like oxygen, the danger of arc overs is drastically decreased at 15 kV in comparison to 20 kV. The demonstrated lateral resolution at 15 kV is around 12 nm compared to 8 nm at 20 kV. The worse lateral resolution derives from the voltage dependency of the aberrations. All experiments that use the electron gun can be performed at both microscopes.

2.1.4 Setup and vacuum

A photo of the "ELMITEC LEEM III" microscope and a scheme of the measurement chamber are shown in Figure 2.3. The measurement chambers of the Elmitec LEEM III and of the SMART are comparable to the experimental features. The measurement chamber is designed for in-situ and real-time experiments. The evaporators point to the measurement position of the sample under a grazing angle of 20° (SMART) and 16° (LEEM III), respectively. Several evaporators can be attached to the measurement chamber. For this work, commercial EFM3s electron beam evaporators from "FOCUS GmbH" with ion suppressor were used [78]. The ion suppressor is required to avoid the acceleration of ions to the negatively charged sample. The evaporators are mounted in a separately pumped z-hub which allows fast exchanges of the evaporators. The temperature of the sample is measured by a high temperature W-5%-Re / W-26%-Re thermocouple, which is spot-welded on the sample cartridge. The thermocouple is in contract with the backside of the sample. The sample can be heated up to 2000 K by electron bombardment. Additionally, at the SMART an infrared pyrometer is installed with an absolute measurement accuracy of 10 Kelvin. The sample is mounted on a transferable cartridge, which contains the thermocouple and the filament for heating. The cartridge is placed on guide bars on a special manipulator. The electric contacts are done with tungsten or rather (for the thermocouple) tungsten rhenium springs. The manipulator has to fulfill some requirements: movement of +/-1 mm in x- and y-direction; adjustment of the sample tilt up to 3° in each direction; high mechanical stability for many minutes including small backlash.

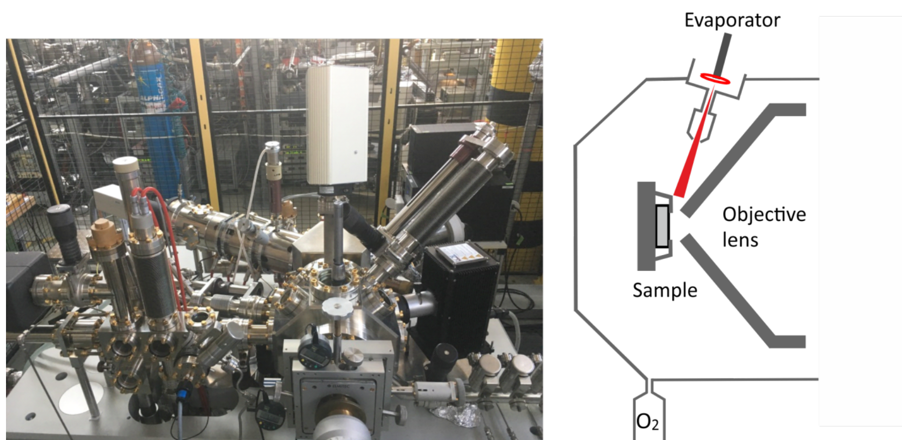

Figure 2.3: Photo of the "Elmitec LEEM III" (left) and a scheme of the main chamber of the used LEEM microscopes (right). The sample is positioned in front of the objective lens by a manipulator. The evaporators point towards the sample in measurement position. The possibility of dosing different gases into the chamber is given.

The low-energy electron microscopes operate under ultra-high vacuum (UHV) conditions, which are necessary to prevent contamination of the sample. The base pressure of the microscopes is $2 \cdot 10^{-10}$ mbar. The pressure measurement is done by Bayard-Alpert hot-cathode ionization gauges [79]. The in-situ and real-time experiments are possible up to $5 \cdot 10^{-6}$ mbar gas atmospheres. For in-situ experiments with simultaneously used synchrotron light a maximum pressure of 10^{-7} mbar is possible. The pressure in the electron gun and in the beam splitter must be as low as possible because the electrons can ionize residual gas molecules. This positively charged residual gas ions are accelerated to the negatively charged sample, where these particles disturb the experiment by contamination. The pumping system consists of an oil-free membrane rough pump to prevent oil contaminations of the vacuum and the sample. The pressure range for the high and ultra-high vacuum is pumped by turbo molecular pumps. For the ultra-high vacuum also ion getter pumps and titanium sublimator pumps are used. To reach a high lateral resolution, it is necessary to reduce vibrations to a minimum. Therefore ion getter pumps are very suitable because they have no moving parts and therefore vibration-free operation.

2.2 LEED theory

In this part the used physical effects should be discussed. For the understanding of the imaging formation in photoemission and reflection microscopy, the knowledge of the interaction of photons and slow electrons with condensed matter is fundamental. For LEEM, some interactions are common, like the propagation of electrons in the sample [22]. In mirror microscopy, the electrons are not penetrating into the sample; the electrons are interacting with electric field modifications caused by the sample morphology and local potential [22]. The LEEM and LEED technique is very surface-sensitive [22]. Due to the strong electron-solid interaction, a free electron is strongly scattered inelastically. Low energy electrons excite plasmons and phonons in the solid [22]. A part of the interaction is electron-electron interaction. The inelastic mean free path of electrons in solids for electrons with energy of 30-100 eV is minimal according to the universal curve of inelastic mean free path [80]. Elastically scattered electrons mostly come from the first surface layers of the crystal lattice [22]. In synchrotron based photo emission spectroscopy or XPEEM the surface sensitivity can be tuned by the kinetic energy of the emitted electrons [22].

For the understanding of a LEED pattern, the kinematic LEED theory is sufficient [22]. The Low-Energy-Electron Diffraction gives information about the symmetry of the crystal and the periodicity [81] [82]. Hence, it is not possible to get an analysis of the unit cell itself by measuring a LEED pattern at specific electron energy. An individual LEED pattern is not unique because of the missing phase information. By analyzing a LEED pattern the distances and periodicity can be determined and the size of a superstructure [82]. The number of atoms per unit cell of a superstructure cannot be determined from a single LEED pattern [82]. Therefore a dynamic LEED analysis of the so-called "LEED-IV" curves is necessary [82].

In the kinematic scattering theory, the surface is divided into columns [83]. The electron is described by a plane wave because the distance between the source and the surface is large in comparison to the distance between the atoms [83]. The wave function of the scattered electron is given by [83]:

$$\Psi\left(\boldsymbol{K}, \boldsymbol{k_i}\right) = \sum_n \Psi_n^{unit}\left(\boldsymbol{K}, \boldsymbol{k_i}\right) e^{i\boldsymbol{Kr(n)}} \tag{2.6}$$

Where n is the number of the unit cell, k_i the initial wave vector and the final wave vector k_f.
The description of diffraction on surfaces can be done by the sum of electron wave functions from the initial wave vector k_i to the final wave vector k_f. According to the Laue condition, where $K = k_i - k_f$ is the scattering vector, the amplitude of the unit cell n is described by [83]:

$$\Psi\left(\boldsymbol{K}, \boldsymbol{k_i}\right) = \sum_n f\left(\boldsymbol{n}, \boldsymbol{K}, \boldsymbol{k_i}\right) e^{i\boldsymbol{Kr(n)}} \tag{2.7}$$

The term $f\left(\boldsymbol{n}, \boldsymbol{K}, \boldsymbol{k_i}\right)$ is the so-called "structure factor" [83]. The structure factor depends on the initial and the final electron wave vector. The structure factor combines the electron wave coming from the surface atom at $r(n)$ and all underlying atoms in the column perpendicular to the surface [83]. In the scattering experiment, the square value of the scattered wave function is measured [83].

$$I\left(\boldsymbol{K}, \boldsymbol{k_i}\right) = \left|\Psi\left(\boldsymbol{K}, \boldsymbol{k_i}\right)\right|^2 = \left|\sum_n f\left(\boldsymbol{n}, \boldsymbol{K}, \boldsymbol{k_i}\right) e^{i\boldsymbol{Kr(n)}}\right|^2 \tag{2.8}$$

The unit cells can have different scattering properties due to films growth, super structures or defects (crystal steps). In the kinematic LEED theory, the scattering from all unit cells is approximately equal [83]. The intensity $I(\boldsymbol{K}, \boldsymbol{k_i})$ separates into [83]:

$$I\left(\boldsymbol{K}, \boldsymbol{k_i}\right) = F\left(\boldsymbol{K}, \boldsymbol{k_i}\right) \cdot G\left(\boldsymbol{K}\right) \tag{2.9}$$

Where $F\left(\boldsymbol{K}, \boldsymbol{k_i}\right)$ describes the form factor [83]:

$$F\left(\boldsymbol{K}, \boldsymbol{k_i}\right) = \left|\Psi_n^{unit}\left(\boldsymbol{K}, \boldsymbol{k_i}\right)\right|^2 \tag{2.10}$$

and $G\left(\boldsymbol{K}\right)$ the lattice factor [83]:

$$G\left(\boldsymbol{K}\right) = \left|\sum_n f e^{i\boldsymbol{Kr(n)}}\right|^2 \tag{2.11}$$

The form factor depends on the value $|K|^2 \propto \sqrt{E}$ of the wave vector [83]. The dependence of $F\left(\boldsymbol{K}, \boldsymbol{k_i}\right)$ on the parallel component is weak. The form factor describes the absolute intensity of the spot. The shape of the spot is given by the lattice factor.

Each crystal lattice can be described by vectors in real space and also by the corresponding reciprocal lattice [84]. The basis vectors b_i in the reciprocal lattice can be constructed by the vectors a_i in real space [84]:

$$b_1 = 2\pi \frac{a_2 \times a_3}{a_1\left(a_2 \times a_3\right)}, b_2 = 2\pi \frac{a_3 \times a_1}{a_1\left(a_2 \times a_3\right)}, b_3 = 2\pi \frac{a_1 \times a_2}{a_1\left(a_2 \times a_3\right)} \tag{2.12}$$

The vectors a_i define the unit cell in real space. The perpendicular vectors b_i define the corresponding unit cell in the reciprocal lattice. The unit cell is the smallest cell in the lattice. By a periodic shift of this unit cell, the crystal lattice can be described completely [84].

The Bragg equation describes the constructive interference of waves with a crystal lattice [84]. The Bragg law is valid for electron and x-ray diffraction at single crystals [84]. The Bragg equation describes the diffraction in real space; the diffraction in k-space is described by the Laue equation [84]. The Bragg equation is given by [84]:

$$2d \sin\theta = n\lambda \tag{2.13}$$

Where λ is the wavelength of the incoming electron or x-ray wave. n is the diffraction order and θ is the scattering angle. d describes the distance between the lattice planes.

The Ewald sphere is used as a descriptive presentation of the origin of the LEED pattern and the corresponding reciprocal space [85]. The Ewald sphere for the LEED geometry is shown in Figure 2.4. The incoming beam is perpendicular to the crystal surface. A spot is only visible if the scattered beam k' is on the Ewald sphere, so the scattered beam fulfills the Bragg equation [85]. The vector addition of the incoming beam and the scattered beam gives the scattering vector G [85]. The radius of the Ewald sphere depends on the electron wavelength [85].

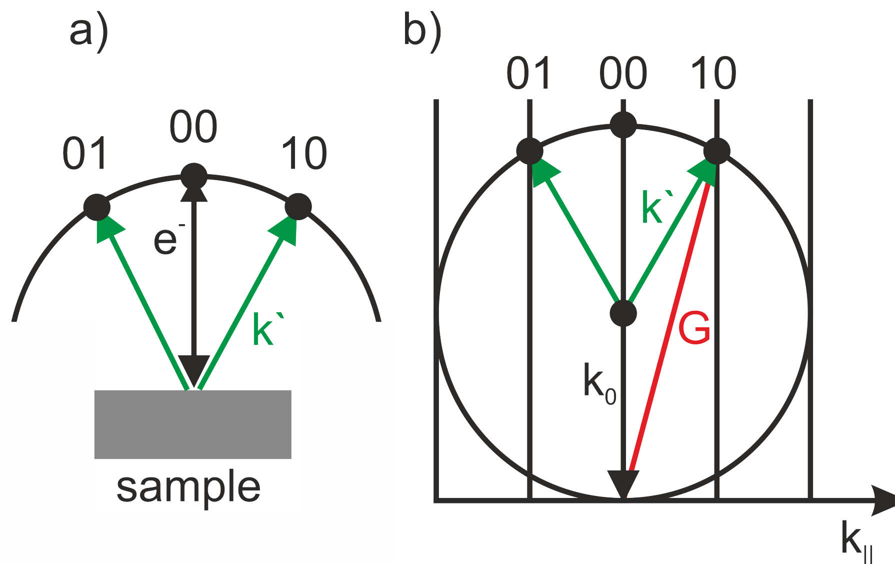

Figure 2.4: Ewald sphere construction to visualize the scattering from a surface. a) shows the LEED geometry in real space and b) shows the corresponding Ewald's sphere. The initial beam k_0 is scattered to k', the reciprocal lattice vector is given by $\mathbf{G}$. So a diffraction spot is only visible if the scattered vector is on the sphere of the Ewald construction. The radius r of the Ewald sphere is defined by the de Broglie wave length of the initial electron $r = k_0 = 2\lambda^{-1}$.

2.3 Photoeffect

2.3.1 Theoretical aspects

The photo effect is fundamental for many operation modes in synchrotron-based spectro-microscopy like XPEEM, XPS and ARPES [22]. The explanation of the photo effect was given by A. Einstein in 1905 [86]. By using synchrotron radiation, it is possible to image photo electrons with an energy-filtered PEEM. The photo-emission spectrum contains three types of electrons [22]: a) electrons from valence or core levels, b) Auger electrons and c) secondary electrons. Mainly core level electrons are used for imaging. The secondary electrons enable a work function contrast. The modern theory of photoemission phenomena is based in the one-step model [22]. The process from photo-excitation, the electron transport to the surface and the transmission through the surface barrier to the detector are described in one single model [87] [22]. The modern theory of the photo effect starts with Fermi's Golden rule [22]:

$$T_{if} = \frac{2\pi}{\hbar} \left| \langle f \left| H_{int} \right| i \rangle \sum_n \frac{\langle f \left| H_{int} \right| n \rangle \langle n \left| H_{int} \right| i \rangle}{\epsilon_i - \epsilon_n} \right|^2 \delta \left(\epsilon_f - \epsilon_i - \hbar\omega \right) \tag{2.14}$$

Fermi's Golden rule gives the transition probability T_{if} per unit time up to the second order from the initial state $i(\Psi_i)$ of the system with energy ϵ_i to the final state $f(\Psi_f)$ with energy ϵ_f [22]. This can happen directly or via a virtual state $n(\Psi_n)$ [22]. The virtual state will be represented by the Hamiltonian H_{int} [22]. By choosing the wave functions and the Hamiltonian, which describe the system (states and interaction with the electromagnetic wave) best, the problem is solved, but in real systems this is generally too complex [22]. For soft x-ray XPS and XPEEM, it is sufficient to use a nonrelativistic approximation, because the photon energy is usually below 1 keV, which is very small compared to the mass of the electron (511 keV) [22]. The transition between the final and initial state is described by the transition matrix element M_{fi} [87] [88]:

$$M_{fi} = \langle \Psi_f \left| H_{int} \right| \Psi_i \rangle \tag{2.15}$$

H_{int} is a small perturbation due to the incident photons. The description of the Hamiltonian can be done by introducing the vector potential $\boldsymbol{A}$ of the external electric field and the momentum operator $\boldsymbol{p}$ [87].

$$H_{int} = \frac{e}{mc} \boldsymbol{A} \cdot \boldsymbol{p} \tag{2.16}$$

Where e is the charge of the electron, m the mass and c the speed of light. The vector potential $\boldsymbol{A}$ can be written as a planar wave.

$$\boldsymbol{A} = A_0 \sigma e^{i(\omega t - \boldsymbol{q} \cdot \boldsymbol{r})} \tag{2.17}$$

$\boldsymbol{q}$ is the photon momentum and $\boldsymbol{r}$ is the coordinate, σ is the polarization of the photon. In the dipole approximation the vector potential $\boldsymbol{A}$ is constant, this simplifies the matrix element to [87]:

$$M_{fi} = \langle \Psi_f \left| \boldsymbol{\sigma} \cdot \boldsymbol{p} \right| \Psi_i \rangle \tag{2.18}$$

The allowed transition from the initial to the final state is described by the selection rules of the photoemission [87]. The transition matrix element must not be zero; this is only given for specific quantum numbers [87]. The resulting dipole selection rules for photo excitation are [88]:

$$\Delta L = \pm 1 \qquad \Delta m_l = 0, \pm 1 \tag{2.19}$$

For the angular momentum quantum number L and the total magnetic quantum number, the spin-orbit coupling is described by the combined angular quantum number [88]:

$$J = L + S \tag{2.20}$$

with the spin quantum number S.

For photoemission from core levels the binding energy E_B is given by [22]:

$$E_B = \hbar\omega - E_{kin} - \phi \tag{2.21}$$

$\hbar\omega$ is the photon energy, E_{kin} is the kinetic energy of the photoelectron and ϕ is the work function of the sample. The beamline UE49-PGM at BESSY II, where the SMART microscope is located, can reach photon energies between 90 eV and 1900 eV. Therefore, it is possible to excite at least one core level of any element, except for hydrogen and helium [89]. Due to the tunable photon energy, the kinetic energy of the electrons can be selected to maximize the cross section of the photoionization or for changing the surface sensitivity according to the mean free path of the photo electrons [89] [22]. It is also possible to probe surface states [22]. By changing the polarization of the synchrotron radiation, different photo emission effects can be studied like dichroism effects in magnetic systems [22]. The binding energy is usually referenced to the Fermi level of the system. The photoelectron spectrum contains electrons from different interactions from photons with solids. The secondary electrons are electrons that have been inelastically scattered. Due to the inelastic scattering, the kinetic energy is low [22]. The photoelectron spectrum contains secondary electrons in the background.

The photoemission leads to the ionization of the atom. According the Koopmans' theorem the energy levels are constant during the first ionization [90]. The observed binding energy is equal to negative orbital energy ϵ. Other electrons can change their energy levels during the photoemission of one electron. This leads to a relaxation. The binding energy of the emitted electron is the energy difference between the $(n-1)$ electron of the final state and the n-electron of the initial state [90].

$$E_B = E_f(n-1) - E_i(n) \tag{2.22}$$

Initial and final state energy contribute to the binding energy of the electrons. Therefore the initial and final state effects should be briefly discussed and their contributions to the observed photoemission spectra [90].

The initial state is the ground state of the atom [90]. Chemical bonds change the ground state and the binding energy of the initial state, the so-called chemical shift [90]. For the first approximation all core level states have the same chemical shift [90]. A shift in the binding energy can also be related to final state effects, the contribution depends of the bond character [90].

Final state effects are related to the relaxation of the electronic states, due to the missing electron, influences the observed binding energy [90]. The relaxation lowers the binding energy. The difference of the observed binding energy is dependent on the atomic relaxation energy and on the extra-atomic relaxation energy [90]. The atomic relaxation results from the rearrangement of the outer shell electrons [90]. The extra-atomic relaxation is dependent on the material properties like electrical conductivity.

For conductive samples, holes can be screened by electrons from other atoms. In insulating materials electrons may become polarized by a core hole [90]. The multiplet splitting and shake-up satellites are also final state effects [90]. The origin of the multiplet splitting is the interaction of core holes with unpaired electrons in the outer shell [90]. If an outgoing electron loses kinetic energy, the electron can excite a valence electron to an unoccupied state and a shake-up satellite is observed [90]. The shake-up satellites are observed at higher binding energies than the core level ground state, due to the transition into an excited state and hereby lower kinetic energy [90]. Shake-down peaks are observed at lower binding energies [90]. The energy loss contributes mainly to the background [90]. In the photoemission spectrum, plasmon peaks can be observed [90].

The observed line shape and width result from many effects [90]. The individual factors are the analyzer and used x-ray source [90]. The Ω energy filter of the SMART microscope has an energy resolution of 180 meV [61], which causes an instrumental line broadening. The transmission function of the analyzer is typically a Gaussian function [90]. The natural line shape can be described by a Lorentzian function and the observed peak is the convolution of both functions [90] [88]. The initial width of the used x-ray beam influences the width of the observed XPS peak [90]. Furthermore, the observed peak width depends on the lifetime of the core hole and satellite features [90]. The natural lifetime of the probed state is caused to the Heisenberg's uncertainty principle [90]. The lifetime of the holes decreases by the higher binding energies [90]. The lifetime of core levels depends on the Auger transition rate of the probed core level [90]. The emission from core levels is narrow and nearly symmetric [90]. The superposition of lines with different chemical shifts leads to an inhomogeneous line broadening [90]. The line shape can be influenced by different final energy states due to spin-orbit coupling or multiplet coupling [90]. Also vibrational excitations contribute to the line shape. The Doppler broadening of the XPS peak contributes also to the final peak [88]. Inelastically scattered electrons also contribute to the line width [90]. This effect is small compared to the lifetime effect. The inelastically scattered electrons have a lower kinetic energy [87]. These electrons contribute mainly to the background of the spectrum. An inhomogeneous charging of the sample can also contribute to the line shape [87]. This effect plays a role in semiconductors or insulators. The observed peak is a convolution of many effects, which contribute differently to the line shape and width.

Auger electrons are a further contribution to the photo emission spectrum [66] [87]. The Auger effect describes a radiation free transition in an atom [90]. A photon excites an electron that is emitted. The excitation can also be done by an electron which is typical for Auger electron spectroscopy (AES) [90]. This caused vacancy is filled by an electron of the same atom but from an outer shell. The released energy is used to emit an electron from an outer shell, the so-called Auger electron.

Another possibility for the energy transfer is the emission of a photon instead of the Auger electron. The fluorescence is negligible of hole energies below 1 keV [90]. In contrast to photo electrons, Auger electrons of one transition have a kinetic energy which is independent of the excitation energy [90].

2.3.2 XPEEM and radiation effects

A highlight of the SMART microscope is the XPEEM mode, the imaging of core levels with a lateral resolution of 18 nm [63]. The imaging of core levels is possible due to the Ω type energy filter, which is unique for such synchrotron-based spectro-microscopes [22]. In order to enable the imaging, the intensity has to be quite high compared to integrating experiments [22]. So the used probing wave e.g. electrons or photons can influence the sample and therefore the measurement itself. Electron-stimulated (ESD) and photon-stimulated desorption (PSD) can be induced [91] [92]. Chemical bonds can be broken by the radiation, which is a common observed effect in synchrotron based μXPS and XPEEM. Especially synchrotron light is very intense compared to a standard x-ray lab source with aluminum cathode [22]. Photon-stimulated desorption is a limitation for synchrotron-based XPEEM and μXPS [22]. The electron energies used in LEEM (10 - 40 eV) can excite valance electrons which can lead to electron-stimulated desorption (ESD) [91] [93]. The first model of the electron-stimulated desorption is the Menzel-Gomer [94] and Redhead model [95]. The Menzel-Gomer and Redhead model describes desorption of adsorbates by slow electrons. In the model, the incoming electron excites the adsorbate by a Frank-Condon transition from the ground state to antibonding state that leads to desorption [94]. A detailed analysis of radiation-induced effects in synchrotron-based XPEEM can be found in [96]. A detailed review of the effects of low-energy electrons on condensed matter can be found in [97].

Residual gas can be cracked by the electrons from LEEM which can lead to chemical reactions on the sample [98]. Due to these effects, the measurement time must be as short as possible and the vacuum must be very good. XPEEM scans of different core levels at the same position to measure the element distribution are critical for photon-induced effects. Due to the low image intensity in the small field of views (4 - 12 μm) long acquisition times are necessary. Furthermore, the use of higher photon fluxes to reduce the acquisition times leads to a space charge effect in the electron mirror of the microscope. Choosing lower photon fluxes causes stability issues for the sample manipulator and the beam position. The finding of a good compromise is necessary for making good XPEEM images without radiation induced effects.

2.4 Model systems and thin film growth

2.4.1 Model systems for catalysis

The understanding of a real catalyst is very difficult and real catalysts are not suitable for many surface science techniques [99]. Model systems for real catalysts are very important to understand the working principle of real catalysts [10]. Model systems allow the research of many relevant effects of heterogeneous catalysis with a reduced complexity and the access to surface science techniques [10]. Many surface science techniques are operating in UHV, however working catalysts operate at high pressures up to a few hundred bars, the so-called ‘pressure gap’ [100].

One main problem is to understand and control the charge transfer in catalysis [101]. A very suitable concept is using ultra-thin oxide films on single crystals as model systems. The oxides have a wide band gap range from strong insulators to semiconductors. This band gap is fundamental for the charge transfer. The electronic properties of the oxide film can be tuned by doping or adding nanoparticles [101]. By doping oxides, the morphology can change, too. The charge transfer can be controlled by the size and shape of nanoparticles. Ultra-thin oxide films allow the studying with surface science techniques [10]. Due to the small thickness of a few nanometers, the charging is dramatically reduced.

For heterogeneous catalysis, the interaction between metals and supports is fundamental for the catalytic activity and selectivity [101] [102]. Understanding the strong metal support interaction (SMSI) [102] is fundamental for the understanding of heterogeneous catalysis. Therefore, the preparation and characterization of ultra-thin films on metals are basic steps for the studying of operating model catalysts [101].

2.4.2 Thin film growth

The understanding of thin films growth is fundamental for the preparation of ultra-thin films on metal supports. Macroscopic and microscopic descriptions of the growth of thin films must be distinguished [103]. The models of the macroscopic descriptions require that the growth is in the thermodynamical equilibrium and the growth event happens close to that equilibrium [103]. In the thermodynamical equilibrium the desorption and adsorption must have the same rate [103]. Therefore, for the description of the growth of thin films, it is necessary to describe also the kinetics because crystal growth is a non-equilibrium kinetic process [103].

One common categorization of the crystal growth was done by E. Bauer in 1958 [104] [105]. There are three basic growth types [106] [103]:

- Frank-van der Merve (layer-by-layer)
- Stranski-Krastanov (wetting layer plus three-dimensional islands)
- Volmer-Weber (three dimensional island growth)

Figure 2.5: Scheme of different thin film growth modes: a) Frank-van der Merve, b) Stranski-Krastanov c) Volmer-Weber (according to [106])

The growth mode is given by the difference of the free surface energy of the substrate σ_S, of the adsorbate σ_A and of the interface energy σ_i between the substrate and the adsorbate [107]:

$$\Delta\sigma = \sigma_A + \sigma_i - \sigma_S \tag{2.23}$$

If $\Delta\sigma > 0$, there is the growth of islands (Volmer-Weber). The surface energy of the adsorbate and of the growing film is larger than the surface energy of the substrate. In this case, the thermodynamical equilibrium will be reached if the wetting of the substrate is as small as possible. The layer-by-layer growth is the case of $\Delta\sigma < 0$. In this case, the surface energy of the adsorbate and the film is smaller than the surface energy of the substrate. There will be a wetting layer formed. The intermediate case is the Stranski-Krastanov growth [106]. In this case, the adsorbate wets the substrate. Due to strains in the growing layer, the surface energy is maximizing during the growth and the film will grow in islands. This growth type happens if the lattice mismatch is large which induces the strain in the adsorbate.

Figure 2.6 shows schematically some processes on the surface during film growth in combination with the Ehrlich-Schwöbel barrier according to [106]. First, the adatom is deposited. On the surface, the kinetic energy of the atom is transferred as adsorption energy to the crystal [108]. The adatom diffuses on the surface. Two adatoms form a dimer, three a trimer. These dimers are the initial process for island formation. The surface diffusion depends on the vibrational frequency of the adatom, substrate temperature and the potential energy of the diffusion barrier. If the adatom diffuses to an atomic step, the diffusion is inhibited. It is also possible that an adatom jumps above a terrace step, if the adatom has enough energy. There are two possibilities, the step-down diffusion and the terrace diffusion. The downward diffusion can be disturbed by the atomic step, this barrier is the so-called "Ehrlich-Schwöbel barrier". This barrier was observed first on self-diffusion of tungsten on tungsten by Ehrlich in 1966 with a field ion microscope [109] and theoretically described by Schwöbel [110]. Adatoms have a stronger bonding at an atomic step, if the adatom diffuses from the lower terrace. This can be understood by a rough approximation, the adatom has more next neighbors than at the terrace. This results in an undulating surface potential with energetically favored places like bridge or on top sides. The atomic step is a barrier if the energy E_{ES} is much larger than the diffusion energy E_{diff}. In this case, the Ehrlich-Schwöbel barrier influences the growth to island formation. This is the so-called "random growth", the adatoms stay on the terrace, on which the adatom arrives on the surface [111]. The coverage of each layer is Poisson distributes and a complete coverage is impossible.

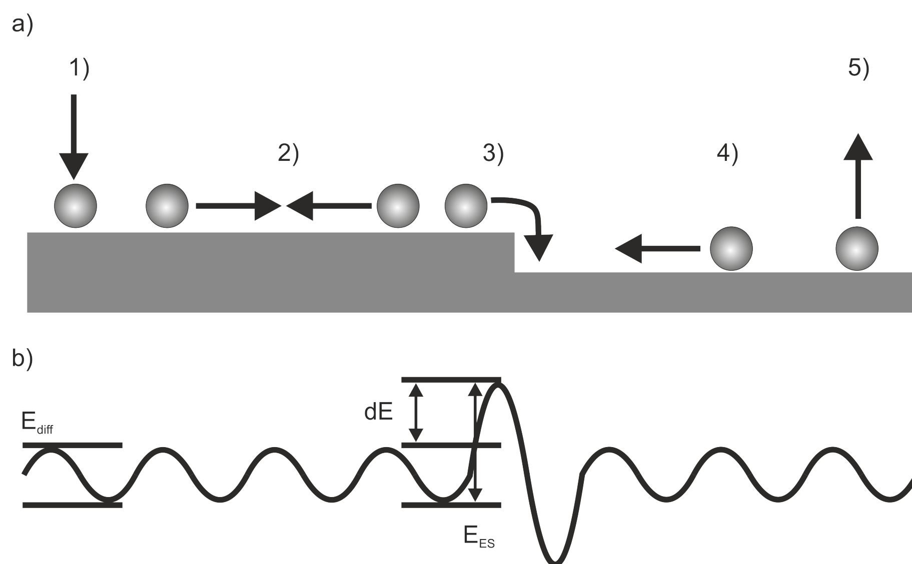

Figure 2.6: a) Processes involved in thin film growth: 1) deposition, 2) nucleation, 3) step-down diffusion, 4) terrace diffusion, 5) desorption b) Ehrlich-Schwöbel barrier (according to [106])

3 Germanium growth on Ru(0001)

The study of the germanium growth on Ru(0001) is essential for the preparation of well-defined ultra-thin germania films in LEEM. The growth of germanium is the starting point of the preparation of ultra-thin germania films on Ru(0001). In this chapter the growth of germanium on bare and oxygen covered Ru(0001) will be presented. A highly reproducible method is required to calibrate the germanium amount on ruthenium and for having a reliable preparation recipe of the ultra-thin germania films. The focus of the this thesis is on the oxides: germania, germania-silica and the hydrogen reaction of those, therefore the growth of germanium is studied briefly. The growth of germanium was studied in real-time at elevated temperatures in UHV by spectro-microscopy applying LEEM and LEED. For chemical information and for the understanding of the LEEM contrast synchrotron based XPEEM and XPS were used. At 540 K temperatures in UHV germanium grows on the bare Ru(0001) surface in large domains with a size of a few hundred nanometers. However, on the 3O-(2x2)-Ru(0001) surface the germanium partially oxidizes during room temperature deposition. Here, the GeO_X forms small domains in the range of the resolution of the microscope. The diffusion of the partially oxidized germanium is inhibited at room temperature. Silicon partially oxidizes on 3O-(2x2)-Ru(0001) comparable with germanium [32]. The formation of small oxide domains of a few nanometer size on 3O-(2x2)-Ru(0001) is also known for silicon in the standard preparation recipe of silica mono- and bilayer on Ru(0001) [32].

The results of this work were generated on the Ru(0001) surface. The crystal structure is hexagonal closed packed (hcp) with lattice parameters a=4.28 Å and c=2.71 Å [112]. Ruthenium is widely used for many different synthesis in heterogeneous catalysis [113] [114] [115] [116] [117]. The Ru(0001) surface has a high affinity to oxygen [118] and forms well-ordered adsorbate structures with oxygen like the 3O-(2x2)-Ru(0001) surface [119] [120]. Oxygen chemisorbs on Ru(0001) and adsorbs on the hcp hollow sits [121]. In the present work only the 3O-(2x2)-Ru(0001) and bare Ru(0001) were used. There are additional the p(2x2)-1O [121], p(2x1)-2O [122] and (1x1)-4O [123] oxygen terminated surfaces. A detailed overview of the properties for the Ru(0001) substrate and O-adlayers in relation to the preparation of ultra-thin silica films can be found in [32] [26].

For the growth study of germanium on Ru(0001), it is fundamental to prepare a clean and smooth Ru(0001) surface. The used Ru(0001) crystal has a miscut smaller than 0.2°. A small miscut of the crystal is required for large terrace sizes, which are essential for LEEM measurements.

The ruthenium crystal was cleaned by several Ar^+ sputtering and annealing cycles, based on the cleaning steps suggested in [124]. The Ar^+ sputtering was performed with an ion energy of 1.5 kV for 10 min with a current of 1 μA. The first annealing step after the sputtering was done in $1 \cdot 10^{-6}$ mbar O_2 for 10 min at 1170 K. Afterwards, the sample was annealed for 10 min in UHV at 1420 K. Finally the ruthenium sample was flashed in UHV for one minute at 1520 K. The annealing in oxygen atmosphere after the sputtering has a high efficiency for removing contamination like carbon layers due to induced defects in the chemically very stable carbon lattice. At induced defects by sputtering, the oxygen can oxidize the carbon which desorbs at the high temperatures. This preparation recipe leads to smooth terraces up to micrometer in size after several repetitions. Finally, XPS measurements at the Ru3d line do not show any contaminations. The main contamination is carbon, other contamination are possible like molybdenum from the sample cartridge due to arc overs. The LEED spots are very sharp which indicate high long-range ordering of the surface. In LEEM the surface appears smooth and clean. The growth experiments were performed directly after flashing the crystal to avoid adsorption of residual gas on the surface.

The so-called germanene [4], a two dimensional honeycomb germanium structure was found on different metal single crystals like Pt(111) [125], Al(111) [126] [127], Ag(111) [128] [129] and Cu(111) [130]. Germanene can be seen as an analogue of graphene or silicence [4]. On the Ru(0001) surface different 2D honeycomb structures have been grown like graphene [131] [132] and boron nitrite [5]. For germanium on Ru(0001), the adsorption structure was studied between 313 K and 333 K by STM [133]. The structure was determined by Fourier transformation of STM images [133] [134] [135] and by this, a $\sqrt{21} \times \sqrt{21}$ R10.9° was found. At such temperatures germanium grows in a Stranski-Krastanov growth mode [133]. On the Ge wetting layer, germanium adatoms can migrate large distances. By DFT calculations the minimal adsorption energy was found for the $\sqrt{21} \times \sqrt{21}$ R10.9° that corresponds to 1/7 ML coverage [134], referred to the (1x1) unit cell of the Ru(0001). In the $\sqrt{21} \times \sqrt{21}$ R10.9° structure, germanium forms trimers [136]. A slightly higher adsorption energy was calculated by DFT for the (2x2) and (3x3) structure [134]. The (2x2) structure has 1/2 ML and 1/4 ML coverage and the (3x3) structure has coverage of 1/9 ML [134]. For Ge on Ru(0001) the adsorption energy increases with increasing coverage. However, the formation of buckled germanene, grown at around 470 K, was observed on Al(111) [137] and Au(111) [4]. On Al(111) germanene can form a (3x3) unit cell [126]. Also coexisting germanene phases are reported on Al(111) [129]. However, the formation of germanium surface alloys is reported on Al(111) [138] and as an interpretation of the Ge/Pt(111) structure [139].

Recently, there are no studies concerning the germanium growth on Ru(0001) at elevated temperatures and on a mesoscopic scale. At elevated temperatures, the expected domain size is larger due to an increased surface diffusion. For studying thin-film growth in LEEM, it is necessary to grow well-ordered domains that are much larger than the resolution limit of the microscope. Therefore, the domain size must be 50 nm - 100 nm for LEEM measurements. The germanium was deposited in UHV by e-beam evaporation from a tungsten crucible. At 540 K desorption of germanium was not observed nor the diffusion into the ruthenium bulk.

3.1 Ge on Ru(0001): LEED and LEEM comparison

The structure evolution of germanium during the growth on Ru(0001) at 540 K in UHV ($1 \cdot 10^{-10}$ mbar) is presented in LEED sequence of figure 3.1. Figure 3.1a shows the initial (1x1) LEED pattern of the clean and smooth Ru(0001) surface. In contrast to a back view LEED apparatus, where the inelastically scattered electrons contribute to the homogeneous background and are partially high passed filtered by a so-called suppressor grid, there inelastic electrons are imaged as a diffuse cloud on the right side, due to the electron optics (dispersive beamsplitter) and the missing energy filter of the used standard LEEM microscope. During the Ge deposition a weak and blurry (2x2) LEED pattern is observed (see figure 3.1b). The initially growing Ge domains are small and show a low long-range order that leads to the blurriness of the (2x2) spots. During the growth these (2x2) spots become sharp and more intense (see figure 3.1c and 3.1d).

The LEED spot intensities are shown in figure 3.1g and h. The intensity of the 00 beam for 15 min and afterwards the intensity increases to a maximum after 30 min. The intensity of the associated (2x2) spots increase to the maximal intensity at 30 min and afterwards the intensity decreases. The intensity of the (3x3) spots increases after 30 min while the other spots decrease in intensity.

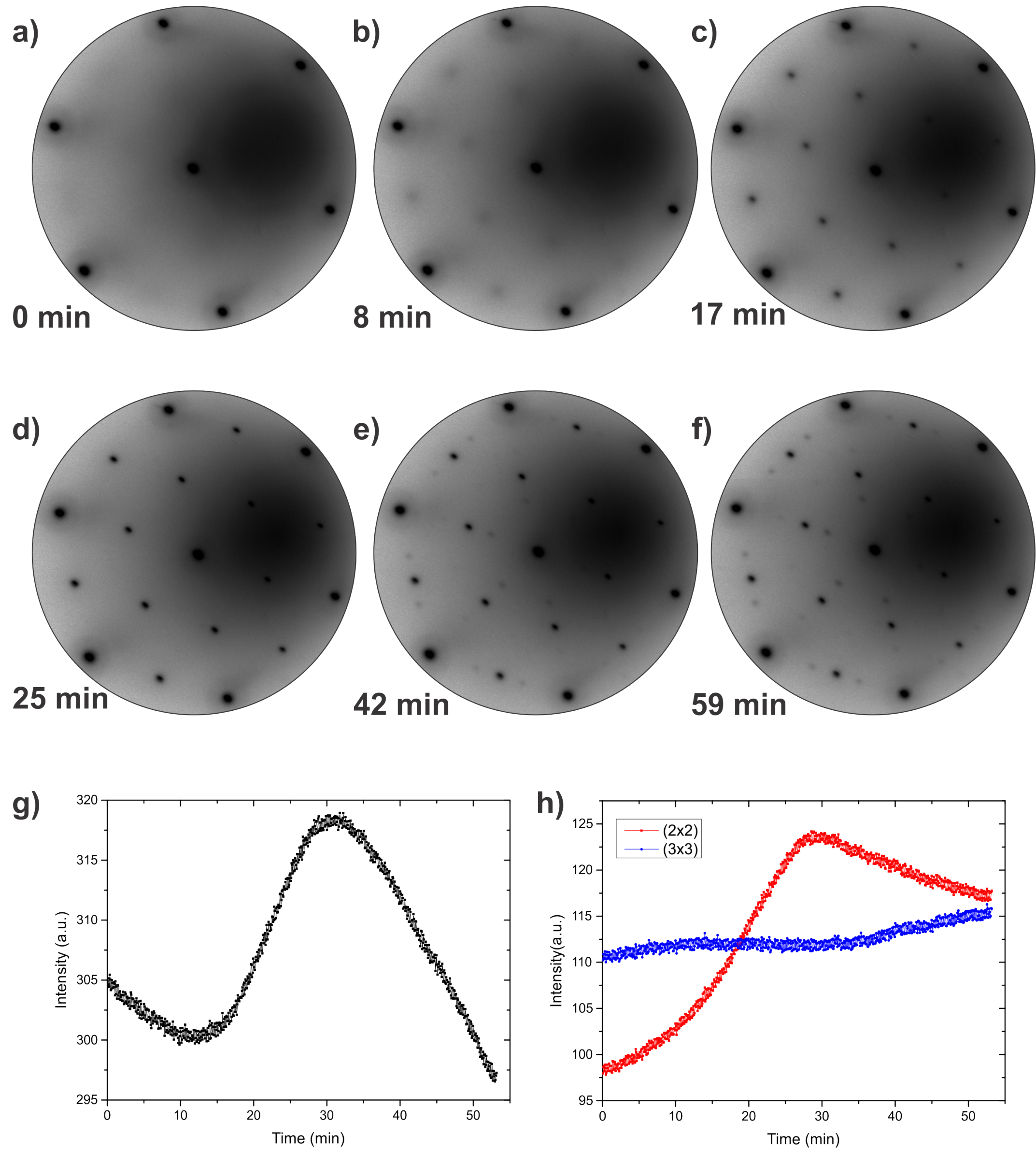

Figure 3.1: Structure formation of germanium during the growth on bare Ru(0001) at 540K in UHV (LEED at 42eV). a) initial (1x1) LEED pattern of Ru(0001), b-d) formation of a (2x2)-Ge/Ru(0001) phase, e-f) formation of coexisting (3x3)-Ge/Ru(0001) and (2x2)-Ge/Ru(0001) phases, g) 00 beam intensity over time, h) LEED intensity (2x2) (red) and (3x3) spots (blue)

Complementary to the reciprocal space, the growth of germanium on Ru(0001) in real space is presented in figure 3.2. In LEEM the growth of germanium on bare Ru(0001) was studied under conditions fully comparable to the previous LEED experiments. The LEEM images were taken at 6 eV kinetic energy. The (2x2) phase is only visible by intensity decrease of the LEEM images. The image 3.2a shows the start of the Ge growth and the early decoration of the atomic steps of the ruthenium substrate with germanium.

The decoration of the atomic steps becomes stronger and small dark areas are visible in figure 3.2b. The dark areas are covered with germanium. The decoration occurs only at one side of the terrace. In figure 3.2d some dark germanium areas appear on the terrace and at the same time the germanium areas at the atomic steps continue to grow in size. The nucleation starts in homogeneously at the atomic steps of the support which is thermodynamically preferred. After the saturation of the steps the nucleation continues on the terraces as homogeneous nucleation. The nucleation on the terrace is diffusion controlled. The formation of the nuclei on the terrace can be located at local defects.

The comparison of the blurry (2x2) LEED pattern (see figure 3.1h) with the LEEM image in figure 3.2b shows that the (2x2) structure is related to the decoration of the atomic steps of the ruthenium support. The intensity of the LEEM image decreases by the formation of the (2x2) structure. The LEEM images of 3.2b and 3.2c show only minor differences, but the related LEED pattern becomes sharper (see figure 3.1c and 3.1d). With further growth, additional weak LEED spots are formed (see figure 3.1e) that become more intense in figure 3.1f. The spots belong to a (3x3) structure that coexists to the (2x2) LEED pattern.

The associated LEEM images to the LEED pattern of figure 3.1e are shown in figure 3.2e and 3.2f. The comparison of the LEED pattern (see figure 3.1e) to the LEEM images (see figure 3.2e) shows that the (3x3) structure corresponds to dark growing areas in LEEM. From figure 3.2e to 3.2l, the formation of new dark areas on terraces during the growth cannot be observed, only an inhomogeneous growth of the dark areas. Some areas are growing in size whereas for other areas the growth is blocked. An Ostwald ripening is not observed, i.e. small islands are not incorporated into bigger islands. On the terraces the nuclei density is low at 540 K. In figure 3.2h and 3.2i the merging of two dark areas can be observed. The inhibited areas stay constantly during the film growth until those areas merge with other dark germanium areas.

In figure 3.2d the size of the dark germanium areas are 20 nm - 50 nm. By continuing the germanium deposition the size of the dark areas increases to maximal 150 nm (see figure 3.2j) or growing areas merge with other ones. The shape of the island is varied. A favored shape is hardly to detect. Some Ge areas show a triangular shape. The growth direction is starting at the atomic steps of the substrate across the terrace. The growth itself is not fractal and the nuclei density is low; some free surface areas are blocked for the growth.
In figure 3.2g an area with new contrast appears on the right side. This area is growing and clearly visible in figure 3.2h. This mid-gray phase can be identified as the second wetting layer of germanium. The growth of the second layer starts before the first layer is closed completely. In figure 3.2i to 3.2l the growth behavior continues with different growth speeds.

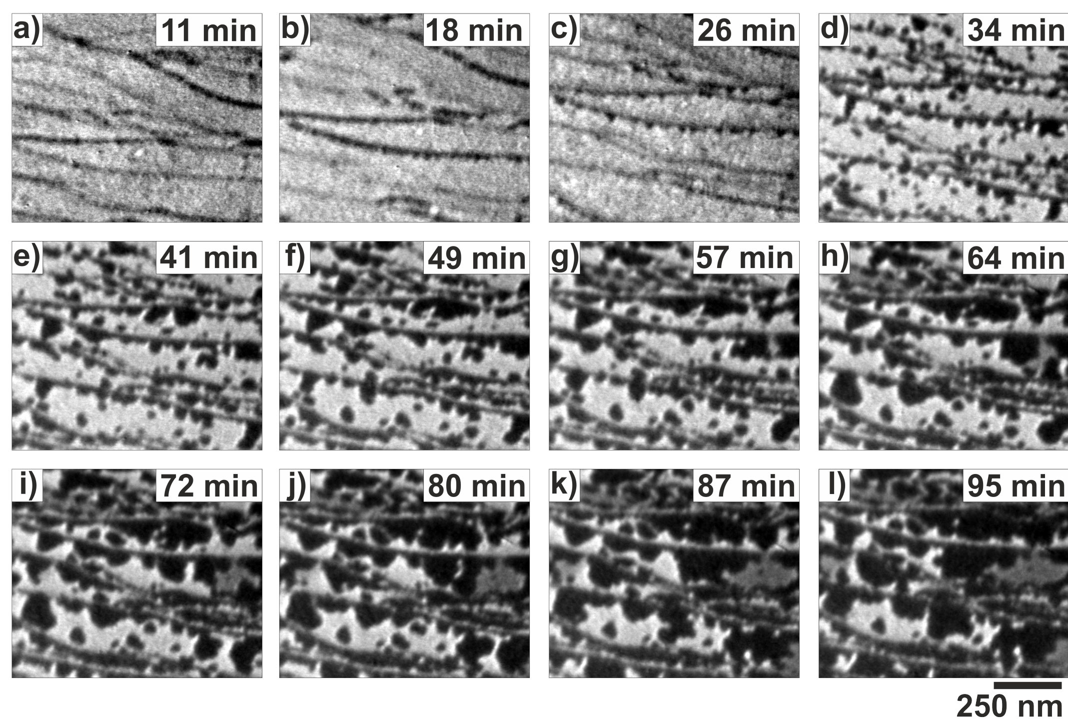

m)

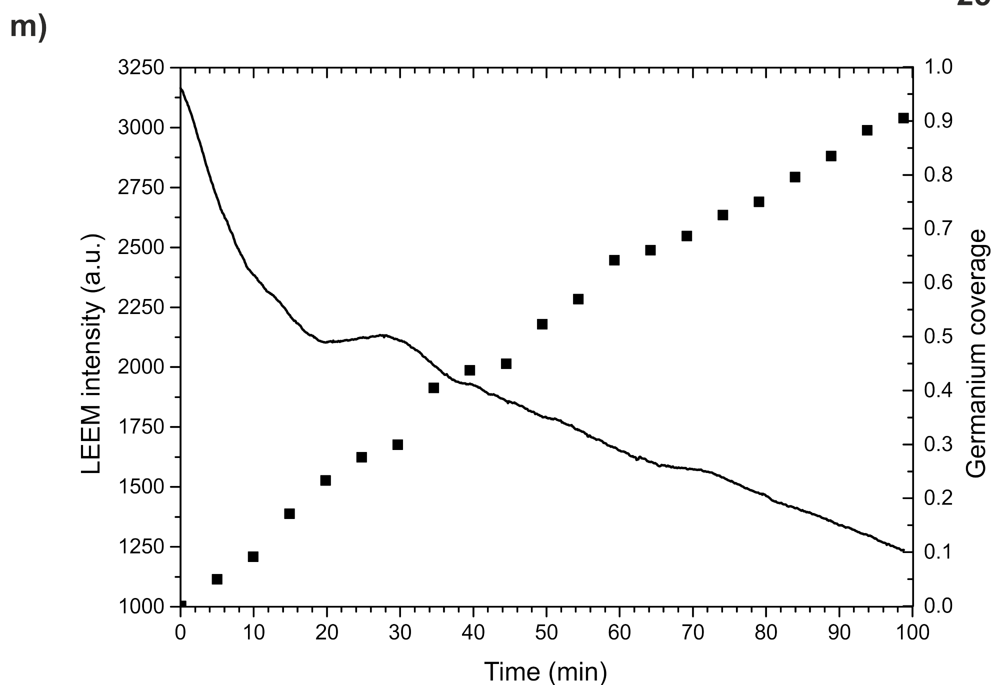

Figure 3.2: a - l) LEEM study of germanium growth on bare Ru(0001) in UHV at 540 K. The LEEM images were taken at 6 eV kinetic energy. m) LEEM intensity during germanium growth compared with the coverage. The LEEM intensity shows between 20 and 30 min and between 65 - 75 min deposition a plateau that correlates with a lower increase of the coverage. The first plateau is associated to the appearing dark (3x3) phase and the second plateau is associated to the mid gray phase.

The coverage evolution of the dark germanium and the LEEM intensity are shown in figure 3.2m. The LEEM intensity correlates with the intensity of the 00 beam in LEED. First, the LEEM intensity decreases and after around 20 min of Ge deposition the intensity increases. At around 30 min of Ge deposition, a plateau is reached. Afterwards the intensity decreases linearly. The during the first intensity decrease the (2x2) germanium phase growth. Also the atomic steps of the ruthenium support become decorated. The increasing LEEM and LEED intensity with simultaneous increase of the (2x2) intensity can be associated with the closing of the (2x2) phase. The coverage is around 25% after 30 min of germanium growth. After the appearance of the dark (3x3) phase, the (2x2) intensity decrease due to the coexistence of both phases. At around 70 min the LEEM intensity reaches a second plateau. In the LEEM images the mid-gray phase starts growing. The coverage is around 65%.

The comparison of LEED and LEEM shows that the Ru(0001) surface is covered by germanium before dark germanium areas are visible in LEEM. Initially only the LEEM intensity (at $E_{kin} = 6$ eV) is decreased. Therefore, the probing of the reflectivity of the surface can be used to identify the different phases. LEEM-IV curves contain information of the work function and information on the crystal structure and electronic structure. A quantitative analysis is complex due to the complex interaction of slow electrons with the sample [140]. LEEM-IV measurements can be used as fingerprints.
The LEEM-IV curves show clearly the formation of different Ge/Ru(0001) phases, as shown in figure 3.3. The LEEM shows one bright area and one area with a dark contrast, the mid-gray phase is missing. The mid-gray phase which is associated to the second wetting layer starts growing at higher coverages of the dark wetting layer as presented in figure 3.3. A LEEM-IV comparison of a highly covered Ru(0001) surface with germanium and 3D germanium islands is shown in figure 3.7. The LEEM-IV curves for both areas are compared with the LEEM-IV curve for the clean Ru(0001). The LEEM-IV curves show that the surface is different at all positions to the LEEM-IV curve for clean Ru(0001).

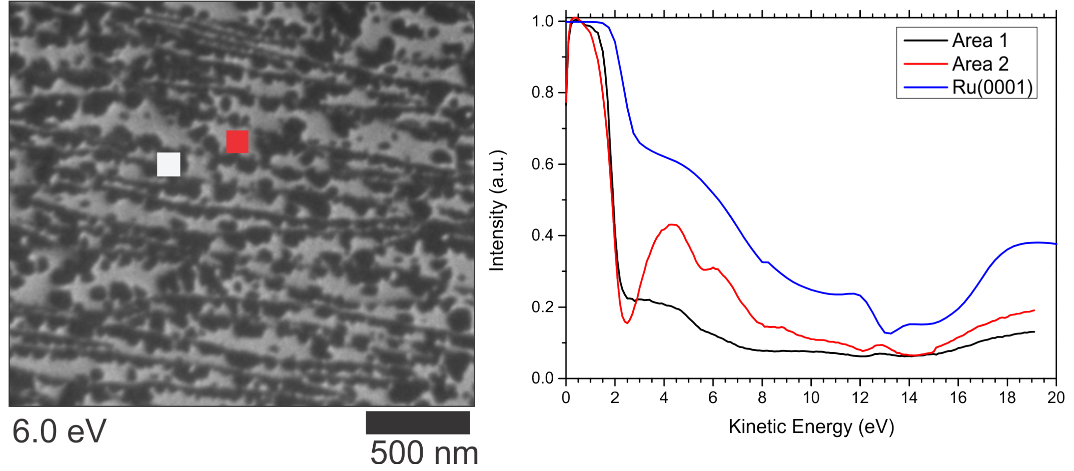

Figure 3.3: LEEM image of Ge on Ru(0001) combined with LEEM-IV measurements at the labeled areas of the image. The white area in the LEEM image has the black-labeled LEEM-IV curve (area 1). Both LEEM-IV curves are different to the LEEM-IV curve of clean Ru(0001) (blue). In both areas, germanium atoms are present. Germanium lowers the work function by around 0.9 eV compared to clean Ru(0001).

The MEM-LEEM transition energy, above which the electrons have enough energy to overcome the surface potential and to penetrate into the crystal, is for the germanium covered Ru(0001) surface lower than for the clean Ru(0001) surface. The MEM-LEEM transition is a relative measurement of the (local) surface work function referred to the fixed work function of the Schottky field emitter. The absolute work function of the Ru(0001) is 5.52 eV [141]. The MEM-LEEM transition of clean Ru(0001) is at 2.5 eV. That leads to an offset of 3.02 eV. So the measured MEM-LEEM transitions can be transferred into the local work functions of the two different germanium phases on the ruthenium surface. The dark germanium phase (area 1) shows a work function difference of 0.2 eV compared to the bright Ge phase (area 2). The bright germanium phase on Ru(0001) has a work function of 4.52 eV and the dark germanium phase of 4.72 eV. The LEEM-IV curves of area 1 and area 2 are very different at low kinetic energies between 2 and 10 eV.

Further deposition of germanium leads to the formation of three-dimensional germanium islands. Figure 3.4 shows a LEED pattern with 3D germanium islands on Ru(0001) combined with a color-coded scheme of the observed LEED spots. The LEED pattern shows the coexistence of a (2x2) and (3x3) structure. The (2x2) spots are shown in red and in blue the (3x3) spots. All observed spots are sharp which is related to highly ordered phase. The observed LEED pattern shows different spot intensities of the (3x3) spots. The highest intensity is observed for the inner spots. The (2x2) spots have a lower intensity compared to the additional spots. Spots that are similar to a (3x1) LEED pattern are more intense compared to additional spots for the (3x3). This indicates that the (2x2) germanium phase decreases by increasing germanium coverage. Also the (3x3) spots show higher intensities for

spots which are associated to a (3x1) phase. The formation of three-dimensional islands claims that locally the maximal density of the wetting layer is reached and thermodynamically the growth of three-dimensional islands is preferred while the surface area is enlarged.

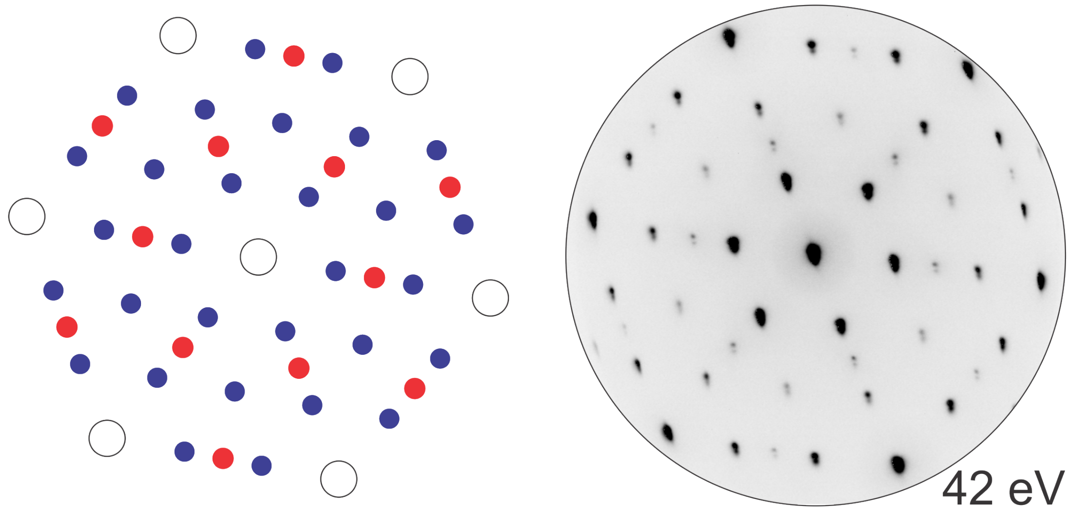

Figure 3.4: LEED pattern after the growth of three-dimensional germanium islands on Ru(0001) and color-coded scheme of the observed LEED spots (red (2x2) and blue (3x3)).

The chemical states of the different germanium phases can be measured spatially resolved by XPEEM. In figure 3.5, a XPEEM scan of a germanium film with 3D islands on Ru(0001) is presented. The XPEEM scan has an incremental step of 0.5 eV. A lower kinetic energy is related to a higher binding energy of the electron in the orbital. The photon energy is 100 eV; the kinetic energies of the electron around 70 eV are chosen to maximize the surface sensitivity due to a minimized mean free path of the electrons [80]. The kinetic energy increases from figure 3.5a to 3.5g. In figure 3.5a the bright areas show minimal differences in the intensity. For higher kinetic energies the differences increase. At 67.0 eV clearly bright areas appear in the image. In figure 3.5d, a homogenous intensity is visible except for some dark areas and the bright islands, which are already visible at 67.0 eV. The dark areas in figure 3.5d are also dark in figure 3.5a. In figure 3.5e the three different areas are marked and the intensities are plotted in figure 3.5h. In the figure 3.5e to 3.5g, the intensity distribution becomes more inhomogeneous and shows bright areas surrounded by dark areas. The images with a more homogeneous intensity distribution have a lower kinetic energy than for the more island-like intensity distribution. The area 2 has a maximum intensity at 69.5 eV and the area 3 at 67.5 eV. All areas show at 67.5 eV and 69.5 eV high intensity.

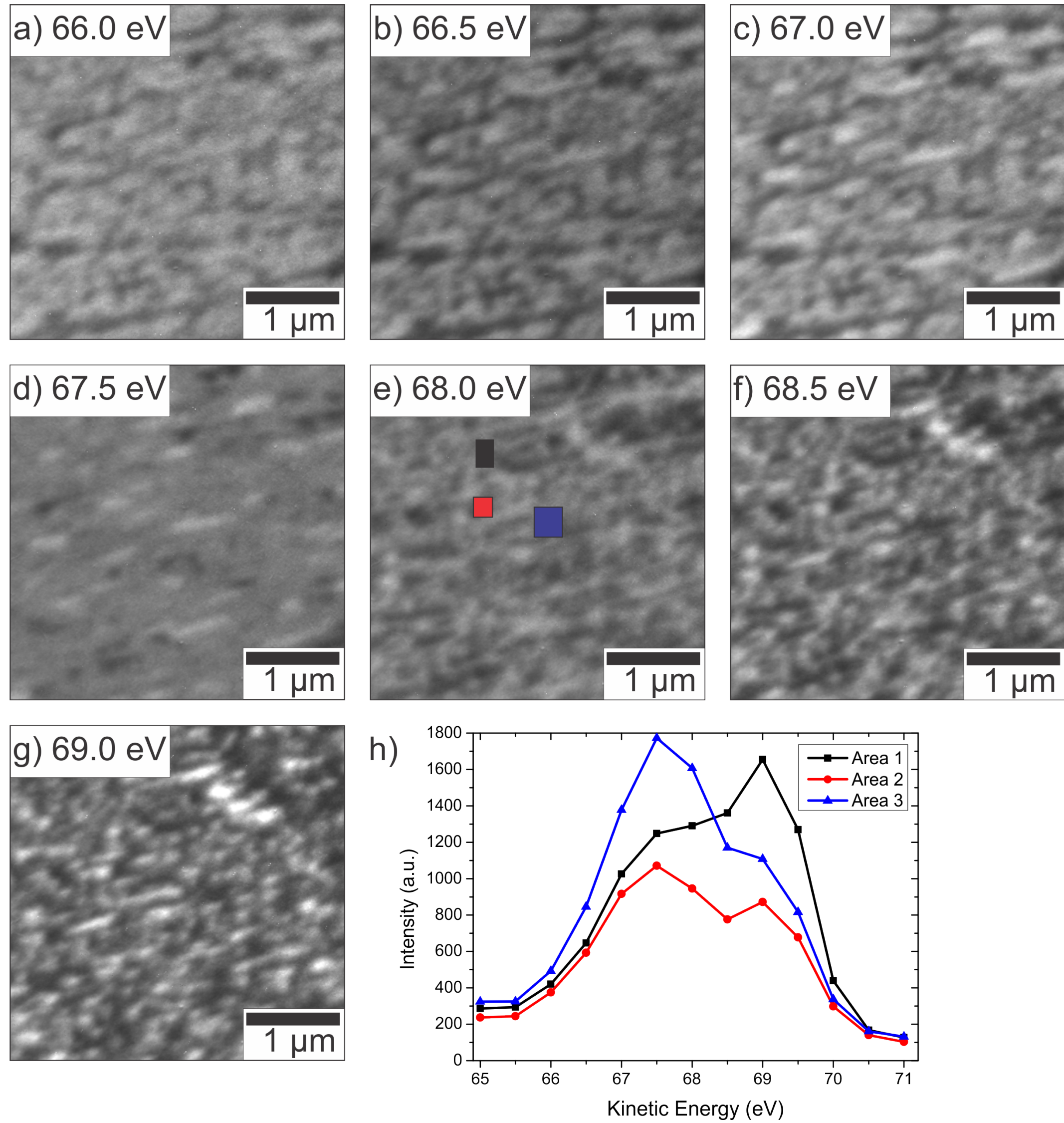

Figure 3.5: XPEEM (hν = 100 eV) scan of Ge3d core level (a-g) and intensity profile (h) of selected areas.

The area labeled as area 1 shows an overall lower intensity than the areas 2 and 3. The intensity scan for all areas has two peaks. The two peaks show an energy difference of 1.5 eV, which is much larger than the spin-orbit splitting of the Ge3d core level of 0.5 eV as observe in XPS (see figure 3.8). The energy difference of 1.5 eV is not related to an interaction of the film with oxygen, but can only be related to local variation of the germanium thickness. The LEEM-IV analysis in figure 3.7 shows a 2 eV higher work function of 3D germanium islands.

A direct comparison of XPEEM images of Ge3d and Ru3d with LEEM is presented in figure 3.6 to combine the high resolution and morphology contrast of the LEEM with the chemical sensitivity of XPEEM.

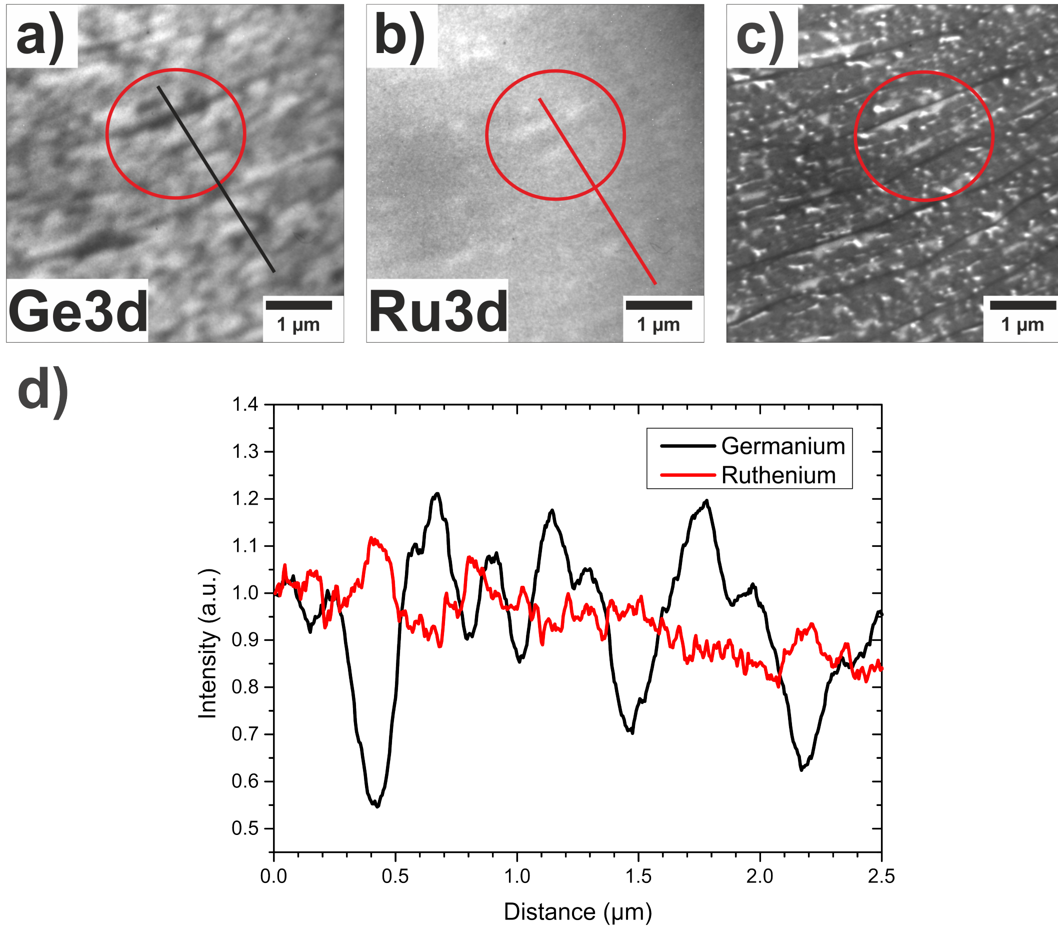

Figure 3.6: Comparison of germanium and ruthenium XPEEM images with LEEM. a) Ge3d (E_{kin} = 67.0 eV, $h\nu$ = 100 eV); b) XPEEM of $Ru3d_{5/2}$ (E_{kin} = 67.5 eV, $h\nu$ = 350 eV); c) LEEM (E_{kin} = 6 eV), d) intensity profile for germanium and ruthenium along the lines as indicated in a) and b)

Figure 3.6a and 3.6b show XPEEM images of the Ge3d and Ru3d core levels at the same position combined with a LEEM image (see figure 3.6c) and an intensity profile of the labeled lines (see figure 3.6d). The XPEEM image of the Ge3d core level shows different intensities. The different intensities are also clearly illustrated in the intensity profile (see figure 3.6d). A low intensity at certain energy can correlate to a locally low amount of germanium or to a different component of the Ge3d peak. At a kinetic energy of 67 eV the dark areas can be correlated to high intensity in the XPEEM image of the $Ru3d_{5/2}$ at 67.5 eV. The intensity profile confirms that the intensities of the Ru3d increase at low Ge3d intensities. That indicates a lower amount of germanium because the intensity of the Ru3d core level is not infected by splitting of the Ge3d core level. The contrast of the XPEEM images correlates with the structures of the LEEM image. The dark area (see figure 3.6a) which is selected in the red circle can be found in the Ru3d XPEEM (see figure 3.6b) and in the LEEM (see figure 3.6c). The mid-gray contrast in LEEM is related to a lower germanium concentration. The very bright small dots in the LEEM image are

not visible in the XPEEM images. The slight variation and intensity decrease are related to inhomogeneities of the illuminating x-ray beam. The areas of the high germanium intensity are correlated to the bright dots in the LEEM image. The bright dots are small three-dimensional germanium islands on a germanium-wetting layer. The germanium wetting layer is not completely closed. A detailed LEEM-IV analysis of germanium with three-dimensional islands on ruthenium is presented in figure 3.7.

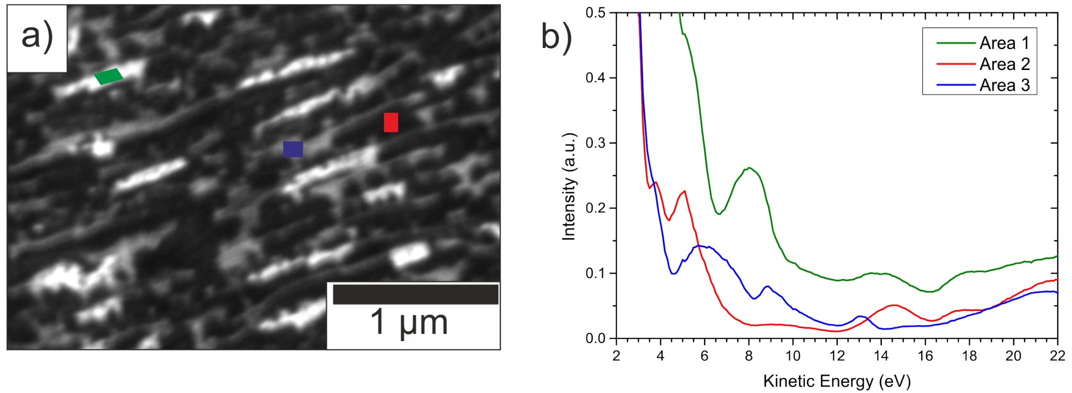

Figure 3.7: a) LEEM (E_{kin} = 6eV) image of a germanium film on Ru(0001) with 3D germanium islands (green label) and first wetting layer (red label) and second wetting layer (blue label), b) LEEM-IV curves of selected areas.

Figure 3.7a shows a LEEM image of germanium on Ru(0001) with three-dimensional germanium islands. The bright areas with the green label are germanium 3D islands on top of a partially closed second germanium wetting layer and a completely closed first wetting layer. The associated LEEM-IV curves are shown in figure 3.7b. The LEED pattern of the films is similar to the LEED pattern presented in figure 3.4. The first and second wetting layer shows a similar work function. The 3D germanium islands have a significantly higher work function. The MEM-LEEM transition for the wetting layers is at 3.1 eV and for the germanium island at 5.1 eV. The LEEM-IV curve of the islands shows a local maximum at 8 eV whereas the second wetting layer shows a local minimum and the reflectivity of the first wetting layer is minimal. The overall reflectivity of the islands is higher than for the other phases. The LEEM-IV curves of the wetting layers show a similar behavior at kinetic energies above 12 eV.

The germanium grows in the Stranski–Krastanov growth mode at room temperature [133] and at 540 K on Ru(0001). At room temperature one wetting layer was reported, however at 540 K two wetting layers are formed before the growth of 3D germanium islands. The 3D germanium islands have an elongated shape which is related to the atomically flat terraces of the support. The growth of the 3D germanium across a terrace step could not be observed.

3.2 Adsorption of molecular oxygen on Ge/Ru(0001) at room temperature

The previous part was focused on the growth of germanium on bare Ru(0001). In the this part, the interaction of germanium on Ru(0001) with oxygen will be discussed. In figure 3.8, the XP spectra of the Ge3d core level of Ge/Ru(0001) (in black) are compared to the Ge3d core level with oxygen adsorbed on O-Ge/Ru(0001) (in red). Due to the used photon energy of 100 eV, the XPS of the Ge3d core level is very surface sensitive. The measured doublet separation of the Ge3$d_{3/2}$ and Ge3$d_{5/2}$ is 0.5 eV. The measured binding energies are 28.5 eV and 29.0 eV for the Ge3$d_{5/2}$ and Ge3$d_{3/2}$, respectively. For the ultra-thin films there is no separation of surface and bulk state in the XP spectra due to the missing bulk component. The Ge3d XP spectrum shows two components: the Ge3$d_{3/2}$ and Ge3$d_{5/2}$. There are no components at high binding energy which are related to oxidized germanium.

The red XP spectrum shows the Ge3d core level after the adsorption of oxygen at room temperature ($p = 1 \cdot 10^{-6}$ mbar O_2). The XPS measurement was done after 220 s oxygen dosing; this would lead to a dose of approximately 300 L with an assumed sticking coefficient of 1. The dose is high enough for fully saturated oxygen coverage. The direct comparison of the XPS of Ge/Ru(0001) and adsorbed oxygen on Ge/Ru(0001) show that the adsorbed oxygen leads to a partial oxidation of the germanium. The observed Ge3d core level shift is around 0.5 eV, due to the formation of Ge-O bonds. In the XPS of Ge3d core levels a shoulder at higher binding energies develops due the adsorption of oxygen. The Ge3$d_{5/2}$ component of the oxygen adsorbed film shows a binding energy of the Ge3$d_{3/2}$ component of the oxygen free film. By dosing oxygen on germanium, the observed intensity of the Ge3$d_{3/2}$ is increasing compared to the Ge/Ru(0001). This is related to a broad component of Ge^{2+} at around 30.5 eV binding energy, which leads to the apparent ratio change of the spin-orbit splitting. A binding energy for Ge^{2+} of round 30 eV was also observed in [142].

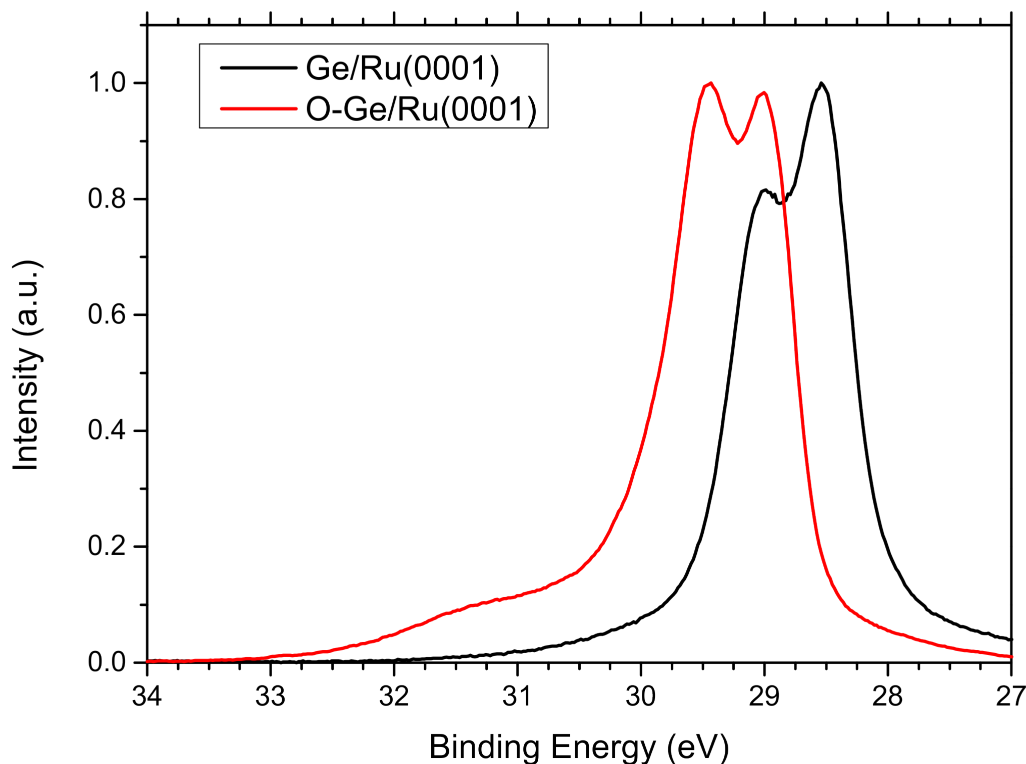

Figure 3.8: Comparison of Ge3d core levels (hν = 100 eV) of Ge/Ru(0001) (black) and O-Ge/Ru(0001) (red).

3.3 Germanium deposition on 3O-(2x2)-Ru(0001)

The deposition of silicon on 3O-(2x2)-Ru(0001) is the most common recipe for the preparation of ultra-thin silica films on Ru(0001) [26]. A detailed study of the deposition of silicon on 3O-(2x2)-Ru(0001) can be found in [32]. Also germanium can be deposited on the 3O-(2x2)-Ru(0001) in oxygen atmosphere to prepare ultra-thin germania films [9]. The deposition of germanium on 3O-(2x2)-Ru(0001) at room temperature in $8 \cdot 10^{-8}$ mbar O_2 is shown in figure 3.9.

The LEEM image (see figure 3.9a) shows the step bunches of the ruthenium support clearly and the terraces appear homogeneous. The LEED pattern in figure 3.9b shows weak and burry (2x2) spots and sharp (1x1) spots of the Ru(0001)support. The sharp (2x2) LEED spots of the oxygen covered 3O-(2x2)-Ru(0001) surface vanished. The blurry (2x2) LEED spots show that the germanium on 3O-(2x2)-Ru(0001) has a low long-range order after the deposition at room temperature.

The XP spectrum of the Ge3d core level is shown in figure 3.9c. The XP spectrum shows the main peak at 31.5 eV binding energy and a shoulder at lower binding energies. The two peaks can be related to Ge^{4+} and Ge^{2+}. The germanium is not completely oxidized to the Ge^{4+} oxidation state after the deposition on 3O-(2x2)-Ru(0001) in oxygen atmosphere.

The associated O1s core level is presented in figure 3.9d. The O1s core level shows the highest intensity at 529.5 eV and a shoulder at higher binding energies. The oxygen contains two components of the incomplete oxidized germanium. The binding energy of the O1s core level of RuO_2 is around 529.3 eV [143]. For the different oxygen termination of the ruthenium surface, a binding energy of 529.2 eV was measured [32]. The O1s core level binding energy of GeO_2 vary from 529.2 eV [144] to around 531.9 eV [145].

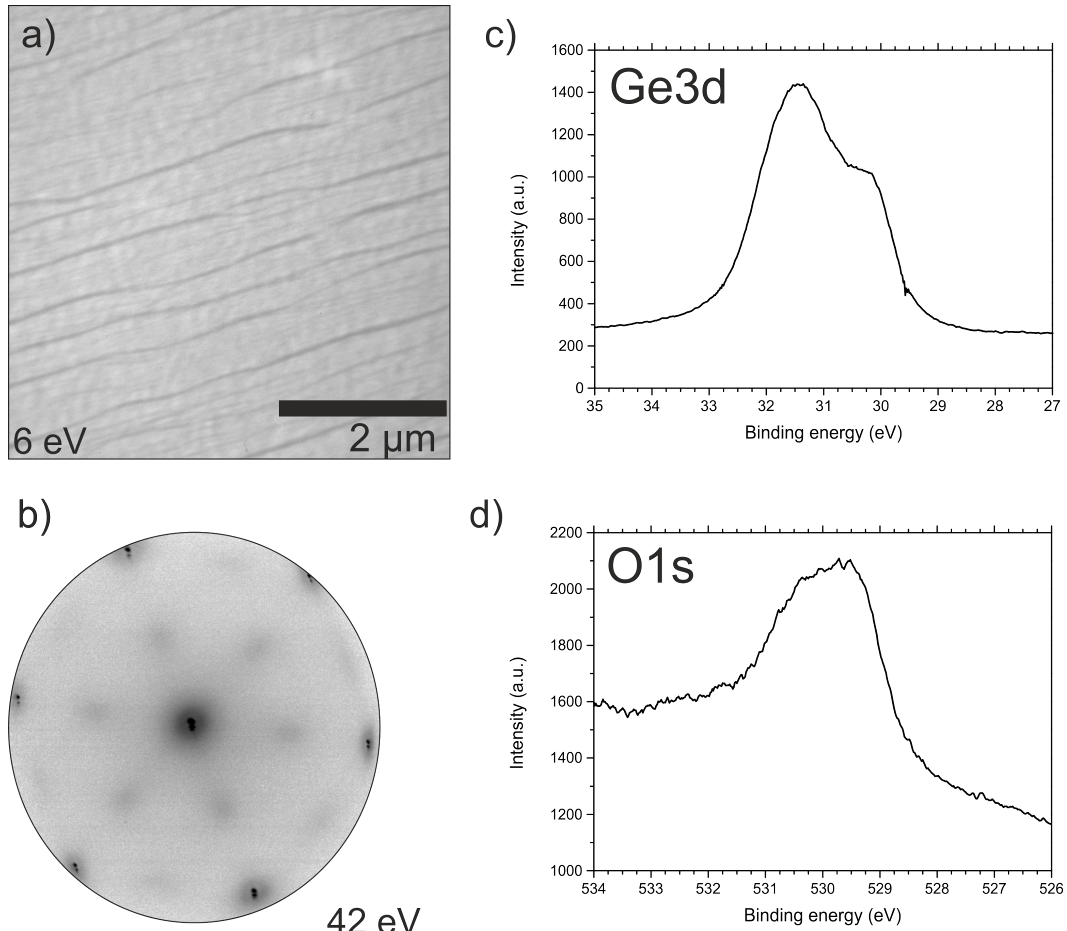

Figure 3.9: a) LEEM after Ge deposition on 3O-(2x2)-Ru(0001) in $8 \cdot 10^{-8}$ mbar O_2, b) LEED pattern, c) XPS of Ge3d core level of GeO_X (hν = 100 eV), d) XPS of O1s core (hν = 600 eV).

By depositing germanium on ruthenium, the ruthenium is influenced by the deposited germanium. Figure 3.10 presents the evolution of the Ru3d core level during the deposition of germanium on 3O-(2x2)-Ru(0001). The black labeled curve shows the XPS Ru3d core level of the initial 3O-(2x2)-Ru(0001) surface. The red labeled curve shows the Ru3d XPS after the deposition of 0.22 ML Ge and the blue curve after the deposition of 0.5 ML Ge. One monolayer is defined as a closed layer of the dark (3x3) germanium phase, as described in the previous part. The measurements were taken under similar conditions without changing the beamline and the microscope. The Ru3d core level shows two peaks due to spin-orbit splitting of the 3d orbital. The more intense peak is the $Ru3d_{5/2}$. A detailed analysis of the Ru3d core levels of different ruthenium oxygen species can be found in [146]. The $Ru3d_{5/2}$ core level consists of two peaks; one component is related to the surface state. The second component is related to the second ruthenium layer or bulk component. The bulk contribution is small due to the mean free path of the of the photo electrons at 360 eV photon energy; mainly the second atomic layer of the support contributes in addition to the surface to the photo emission spectrum.

The Ru3d core level peak shifts during the deposition to lower binding energy. The shift between the initial 3O-(2x2)-Ru(0001) and the 0.22 ML GeO_X/Ru(0001) is 0.12 eV. The Ru3d peak intensity is damped by a factor 1.5 due to the adsorbed germanium. The damping becomes stronger for more adsorbed germanium. The shift from the initial 3O-(2x2)-Ru(0001) surface to 0.5 ML GeO_x/Ru(0001) is 0.15 eV.

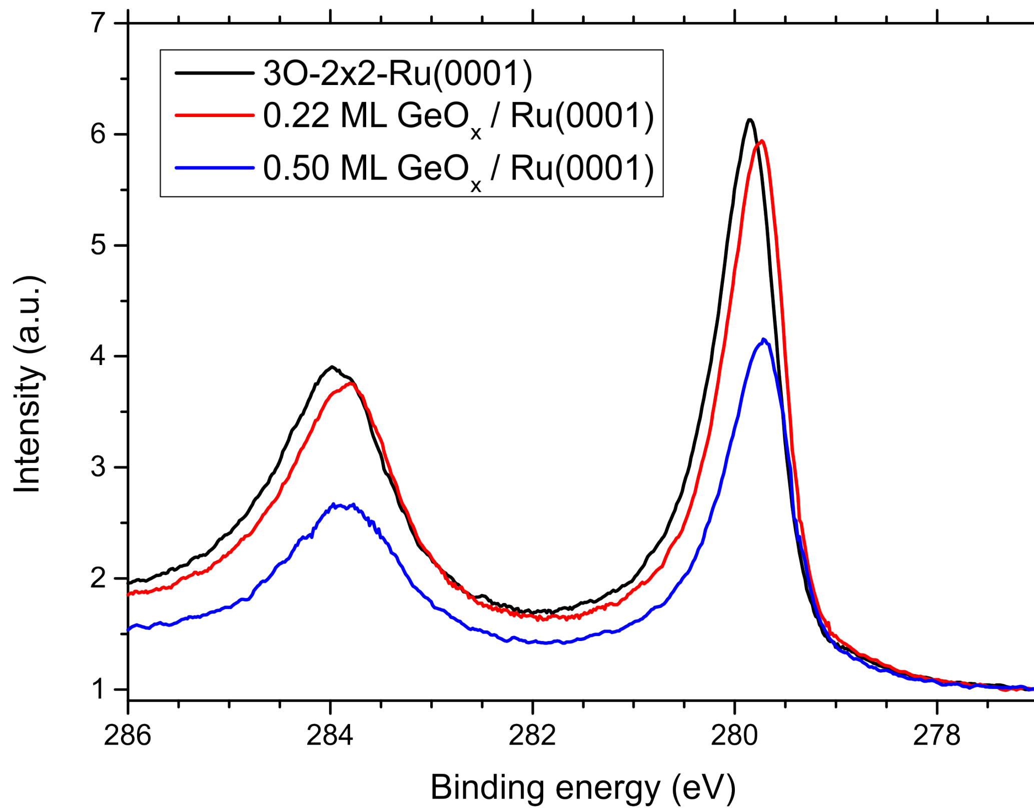

Figure 3.10: XPS of Ru3d during germanium deposition in $8 \cdot 10^{-8}$ mbar O_2 at room temperature on 3O-(2x2)-Ru(0001). The initial Ru3d spectrum of the 3O-(2x2)-Ru(0001) is shown in black. The spectrum after the deposition of 0.22 ML GeO_X is shown in red and after the deposition of 0.5 ML GeO_X in blue.

3.4 Interpretation

The information of the different experimental methods can be used to propose a model of the Ge growth on Ru(0001) at 540 K. The observed LEED patterns during the growth of germanium on ruthenium are different to the published structures for the growth of germanium on Ru(0001) at room temperature. The growth of germanium on Ru(0001) at room temperature was observed by atomically resolved STM for low coverages [133]. A $\sqrt{21} \times \sqrt{21}$ R10.9° structure is reported by STM for the sub-monolayer regime, a LEED pattern is not shown in [133]. For higher coverages the formation of three-dimensional islands on the germanium wetting layer is observed [133], the STM images are not atomically resolved.

Figure 3.1 shows that germanium forms initially a (2x2) structure on Ru(0001) at 540 K in UHV. By continuing the growth a coexisting (3x3) structure is formed. Figure 3.1g and h show that initially the intensity of the 00 is decreasing and increasing with the formation of the (2x2) phase. The intensities of the 00 beam and of the (2x2) spots show a similar behavior. The 00 beam and the (2x2) spots reach a maximal intensity by the highest coverage of the (2x2) phase. Here the long-range order is maximal. The intensity of (2x2) and 00 spots are decreasing by the formation of the (3x3) phase. Both phases are coexisting. The appearing (3x3) phase lowers the long-range order of the surface which leads to the decreasing intensity. A contrast change is not observed for the (2x2) structure (see figure 3.1) in LEEM (see figure 3.2), only a decrease of the intensity (see figure 3.1g and h). The comparison of the LEED (see figure 3.1) and LEEM images (see figure 3.2) shows that the (3x3) structure changes the LEEM image and dark areas appear. A second wetting layer is formed before the first (dark phase) is closed completely. The LEEM-IV analysis (see figure 3.3) shows that the complete surface is covered by the different germanium phases. The direct comparison of the Ge3d and Ru3d XPEEM with LEEM image in figure 3.6 leads to the explanation of the different contrasts of the LEEM image. The grown germanium film has holes and coexisting germanium islands (bright in LEEM). The XPEEM intensity profile shows the different germanium thicknesses and the Ge3d and Ru3d core levels are correlated, a high germanium intensity leads to a low ruthenium signal (see figure 3.6).

The formation of three dimensional islands can be observed. The work function of the islands are 2 eV higher compared to the dark and mid-gray germanium phase (see figure 3.7). Also the XPEEM scan shows the shift of the Ge3d core level by 2 eV of the islands (see figure 3.5). The difference of the work function and the core level shift is very huge. The germanium islands might disturb the electron beam that cause the huge difference of the work function. The germanium films with three-dimensional islands show also the (2x2) and (3x3) LEED spots, but spots belonging to a (3x1) structure are more intense compared to the (3x3) structure. The LEEM and XPEEM studies show that germanium grows in the Stranski–Krastanov growth mode on Ru(0001).

The XP spectrum of the Ge3d for Ge on bare Ru(0001) is shown in figure 3.8. The Ge3d core level is splitted due to spin orbit splitting of the 3d orbital. The non-oxidized germanium has a binding energy of the Ge3d core level of 28.5 eV and 29.0 eV for the $Ge3d_{5/2}$ and $Ge3d_{3/2}$, respectively. The measured doublet separation of the $Ge3d_{3/2}$ and $Ge3d_{5/2}$ is 0.5 eV. The measured binding energies are 28.5 eV and 29.0 eV for the $Ge3d_{5/2}$ and $Ge3d_{3/2}$, respectively. This is in good agreement to doublet separation found in literature of around 0.58 eV [147].
The adsorption of oxygen leads to a shift of the Ge3d core level. The observed core level shift of around 0.5 eV is smaller compared to the 0.85 eV per Ge-O bond published in [148]. In figure 3.8, the observed chemical shift of the $Ge3d_{3/2}$ and $Ge3d_{5/2}$ core level is around 0.5 eV. Due to the adsorption of oxygen the XP spectrum shows a shoulder at higher binding energies. The shoulder contains two components, one at around 30.5 eV and one at around 31.5 eV. The observed shifts fit to GeO at 30.5 eV and GeO_2 at 31.5 eV. The adsorption of oxygen leads to an apparent ratio change of the spin-orbit splitting, due to the GeO component close to the $Ge3d_{3/2}$ component.
Germanium deposition on 3O-(2x2)-Ru(0001) in oxygen atmosphere leads to a partial oxidation of the germanium (see figure 3.9). The Ge3d core level shows two components one at 31.5 eV and the second at around 30.5 eV. Here the Ge3d core level consists partially of Ge^{4+} and Ge^{2+}. The O1s core level shows the highest intensity at round 529 eV binding energy and a second component at 530.5 eV. The germanium becomes more oxidized by the deposition on 3O-(2x2)-Ru(0001) in oxygen atmosphere compared to the adsorption of oxygen. The partial oxidation is also known for silicon deposition in oxygen atmosphere on 3O-(2x2)-Ru(0001) [32]. The LEEM of GeO_X shows a homogeneous image. The LEED pattern shows a blurry (2x2) pattern. For SiO_X on Ru(0001) the intensity of the LEED spots depends of the deposited silicon amount. The effect on the ruthenium support by the deposition of germanium is shown in figure 3.10. The Ru3d core level peak shifts by around 0.15 eV during the germanium deposition to lower binding energy. The shift of the Ru3d core level might be related to the reduction of the surface by the germanium.

A model for the observed germanium growth at 540 K in UHV can be proposed. In figure 3.11a the $\sqrt{21} \times \sqrt{21}$ R10.9° structure is shown that is observed by STM [133] and calculated by DFT at room temperature [134] [136]. The DFT calculations suggest that germanium energetically prefers to maximize the distance between the adsorbed germanium atom on the Ru(0001) [136]. At low coverages, germanium adsorbs at the hcp sites which are the most preferred adsorption sides on the ruthenium [136] [134]. However, DFT calculations show that the adsorption energies of the (2x2) structure with 0.25 ML, 0.50 ML and the (3x3) structure with 1/9 ML are thermodynamically more unfavorable [134]. The differences in the adsorption energies of the (2x2) and (3x3) structures are around 0.1 eV higher compared to the $\sqrt{21} \times \sqrt{21}$ R10.9° structure [134].

The small energy difference could overcome by annealing. The unit cell of the $\sqrt{21} \times \sqrt{21}$ R10.9° structure includes two additional germanium atoms, which form a triangle (see figure 3.11a) [136]. The density of the $\sqrt{21} \times \sqrt{21}$ R10.9° structure is 1/7 ML referred to the Ru(0001) unit cell [134].

In figure 3.11b a proposed (2x2) structure is shown that is constructed by the germanium triangles from figure 3.11a. This (2x2) structure has a germanium coverage of 1/4 referred to the (1x1) unit cell of the Ru(0001). This (2x2) structure (see figure 3.11b) is a probable structure for the observed initial germanium phase on Ru(0001) at 540 K. In figure 3.11c, a proposed (2x2) structure with a higher coverage of 1/2 is assumed. The structure in figure 3.11c is a honeycomb structure and half of the Ge atoms adsorb on the top site. This positions of Ge atoms were found for GeO_2 on Ru(0001) [9]. This leads to a maximized distance between the Ge atoms.

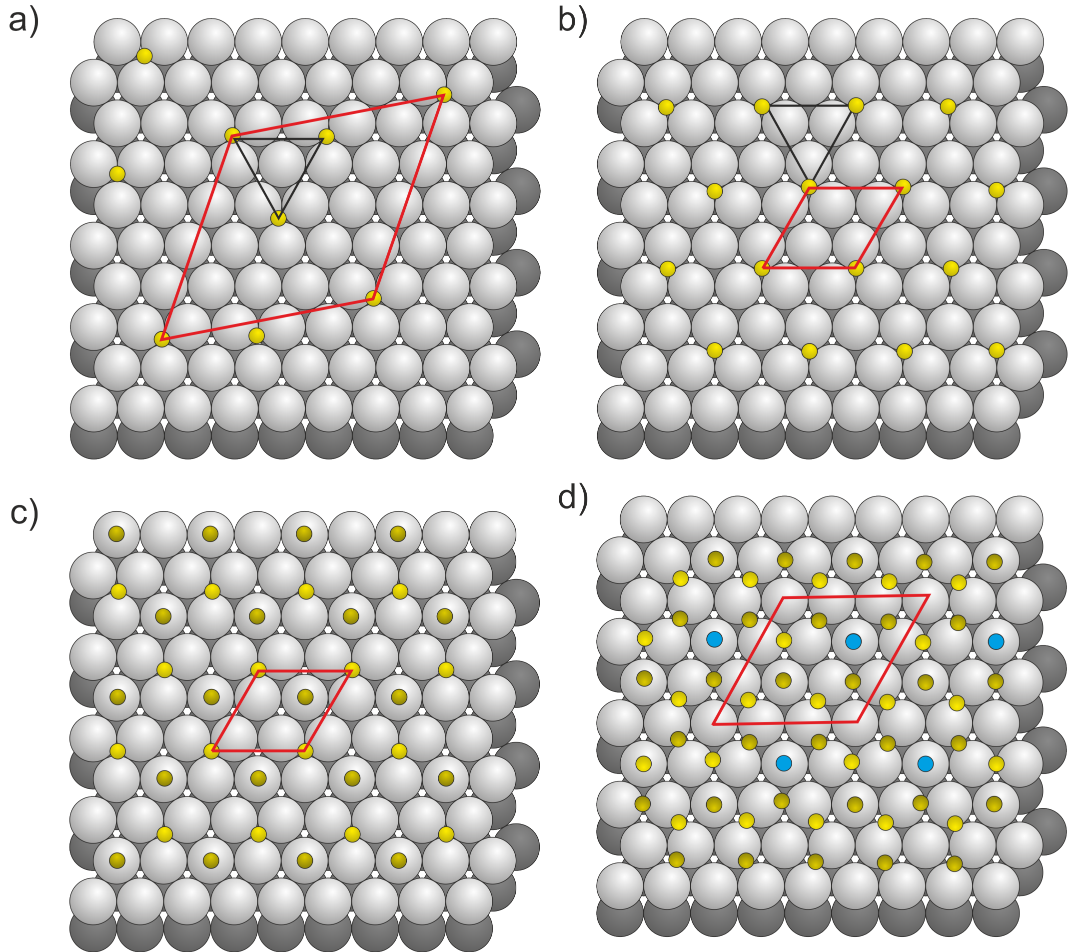

Figure 3.11: Germanium structures on Ru(0001): a) $\sqrt{21} \times \sqrt{21}$ R10.9° structure reproduced from [136], b) proposed (2x2) structure with triangles from a), c) honeycomb (2x2) structure, the Ge atoms are on the adsorption sides of GeO_2 [9], d) proposed (3x3) germanene structure on Ru(0001). The blue labeled atoms on the top sites might have a larger distance to the ruthenium surface.

If the preferred adsorption sites are occupied by germanium and more germanium is deposited, there are three possibilities for the further germanium growth: a) direct desorption of Ge; b) Ge diffusion into the ruthenium bulk and c) filling of the structure. The LEEM and LEED experiments show that the growth continues after the formation of the initial (2x2) structure. Hence, the desorption rate of Ge is lower than the adsorption rate at 540 K on Ru(0001). The diffusion into the ruthenium bulk was never observed within the used experimental conditions. The presence of germanium close to the surface can be excluded by XPS of the Ru3d. There is no indication of a ruthenium-germanium surface alloy which is well-known for germanium and platinum [149].

The observed germanium structure shows a (2x2) LEED pattern with a coexisting (3x3) structure. The formation of a (3x3) germanene structure was found on Al(111) [126]. Germanene has a buckled structure on Al(111) [137]. The calculated nearest neighbor distance of free standing germanene is $d_{Ge-Ge} = 0.238$ nm [150]. The Al(111) surface has an nearest neighbor distance of $d_{Al-Al} = 0.286$ nm [126]. For the (3x3) germanene structure on Al(111) a periodicity of 0.85 nm was found [126], the mismatch of germanene on Al(111) is around 5.4 %. On $\sqrt{7} \times \sqrt{7}$ Au(111) the mismatch of (2x2) germanene is around 4.2 % [151]. The mismatch of (3x3) germanene on Ru(0001) would be around 4.9 %. The reported preparation temperature of germanene is at around 360 K [152]. However deposition temperatures of around 470 K are reported in [4]. This is in the temperature range of the present study. It is reported that coexisting phases would probably reduce the surface energy [129]. Also on Ru(0001) two coexisting germanium phases are found. A (buckled) (3x3) germanene-like structure is a feasible Ge/Ru(0001) structure. The mid-gray phase in figure 3.2 could be a second germanene layer. The existence of multilayer germanene is published in [153]. However a detailed structural analysis is necessary to clarify the observed germanium structures on Ru(0001).

3.5 Conclusion

The results show that germanium grows in the Stranski–Krastanov growth mode on bare Ru(0001) at 540 K. However the present results show different structures compared to the published structures. During the germanium growth a (2x2) structure is formed. This structure decreases the LEEM intensity. Further germanium deposition leads to a coexisting (2x2) and (3x3) structure. The (3x3) shows a strong contrast in LEEM at 6 eV kinetic energy. The growths continues with the formation of a mid-gray germanium phase on top of dark gray (3x3) structure. This mid-gray structure grows before the dark-gray structure is completely closed. Finally three dimensional germanium islands are formed which appear bright in LEEM (at 6 eV). For a detailed structural analysis further research is necessary. However a germanene-like structure would be a feasible structure. Germanium reacts at room temperature with the oxygen of the 3O-(2x2)-Ru(0001) surface and forms a blurry (2x2) structure.

4 Ultra-thin GeO_2 films on Ru(0001)

In this chapter the formation and properties of ultra-thin germanium dioxide (GeO_2) films on Ru(0001) films are presented. This chapter consists of three parts. First the real-time oxidation of the germanium films on Ru(0001) is reported. The oxidation of a 0.6 nm thick germanium film on Ru(0001) is shown in the second part and the properties of GeO_2 films on Ru(0001) on a mesoscopic scale combined with an analysis of the chemical properties are described in the third part.

4.1 Formation of GeO_2 on Ru(0001) - in real-time

The initial germanium film was prepared as described in the previous chapter in particular by deposition of germanium at 540 K in UHV on bare Ru(0001). For the study of the real-time oxidation of germanium, the germanium film was annealed in UHV to 600 K and afterwards the oxygen was dosed up to a pressure of $1 \cdot 10^{-6}$ mbar. During the annealing in UHV, the germanium films are stable and checked by LEEM and LEED.

Figure 4.1 shows a real-time LEEM sequence of the germanium oxidation on ruthenium. Figure 4.1a shows the germanium film at 600 K in UHV with bright lines which can be related to GeO_X, due to residual oxygen on the Ru(0001) surface. The images 4.1b to 4.1k show the oxidation of the germanium film on Ru(0001). The oxygen pressure was increased from 10^{-10} mbar (see figure 4.1a) to $1 \cdot 10^{-6}$ mbar (see figure 4.1b - d). The oxidation starts at an oxygen pressure of around 10^{-8} mbar (see figure 4.1b). During increasing the oxygen pressure bright dots appear (see figure 4.1b) which are obviously the growing oxide areas. In figure 4.1g - 4.1j the oxide grows on the entire terraces. The real-time measurement shows that the growth velocity is different for the terraces that can be seen in figure 4.1e; one terrace is still dark meanwhile the appearing bright oxide is formed on other terraces. Already visible bright areas (see figure 4.1h) become more pronounced in figure 4.1k. The bright areas can be determined as excess material.

The oxidation time is around 77 s (see figure 4.1 d-k) after reaching the final oxygen pressure of $1 \cdot 10^{-6}$ mbar. In figure 4.1l, the associated LEED pattern of the germania film is presented. The LEED pattern shows sharp (2x2) spots which indicates a good long-range order of the germania film on Ru(0001).

The evolution of the coverage was done by threshold images of the different intensities of the LEEM image at 6 eV. The threshold images are shown in figure 4.1m for the initial and the oxidized film. The scheme in figure 4.1m visualizes the oxidation of germanium. The bright areas (GeO_X or GeO_2) are located at the atomic steps of the Ru(0001) crystal (blue) and the germanium is painted in green. The initial films shows 16 % bright GeO_X areas (in the scheme blue). After the oxidation the complete surface is covered with the GeO_2 (blue) and addiationally bright excess material is visible (red). After the oxidation, the germania film shows 14 % bright areas (red in the scheme).

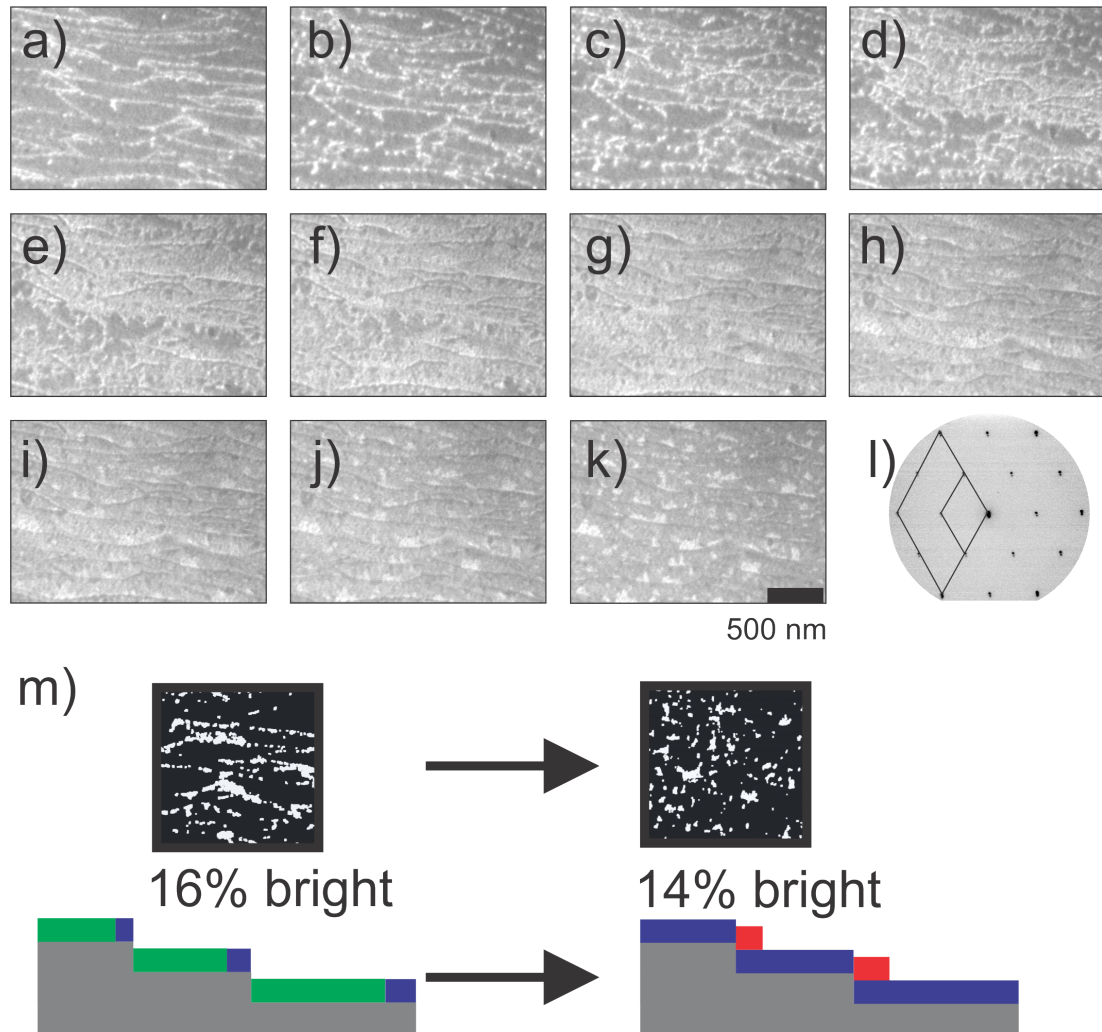

Figure 4.1: Real-time oxidation of germanium on Ru(0001) in LEEM (E_{kin} = 6 eV) series (a - k) at 600 K. Oxygen pressure in a) is p = $1 \cdot 10^{-10}$ mbar, b) p = $1 \cdot 10^{-8}$ mbar c) p= $1 \cdot 10^{-7}$ mbar and in d) - k) p = $1 \cdot 10^{-6}$ mbar. The oxidation time for (a-k) is 0 s, 18 s, 33 s, 44 s, 55 s, 60 s, 64 s, 69 s, 73 s, 79 s and 121 s respectively. The dark area in (a) is the germanium and the bright lines are the atomic steps. The oxidation starts at the atomic steps (b-c) and the oxidation front moves from the top to bottom in the image (d-g). In h) the oxygen reaches the complete film. In i)-k) the film is oxidized and excess material (bright areas) appear at the bottom side of the terrace. The associated LEED pattern (l) shows (2x2) spots (42 eV). m) Coverage determination before the oxidation (16 % bright areas) and after the oxidation (14 % bright areas). For visualization a scheme shows the expansion of the film. The initial germanium film is shown in green on the support. The excess material (bright in k) is shown in blue and the germania monolayer in red.

In contrast to the high germania coverage with excess material, a germania film without excess material and germania free areas is shown in figure 4.2. The initial germanium film (see figure 4.2a) has a coverage of 45 % (dark in LEEM). The oxidation conditions are fully comparable to the previously shown experiment in 4.1. The dark germanium areas are similar to the film shown in figure 4.1, and the bright areas are Ru(0001) with the low dense germanium phase, as shown in chapter 3. During the oxygen dosing a slight change of the intensity is observed and presented in the intensity over time plot (see figure 4.2g 0 - 60s). The oxygen pressure increased $p = 5 \cdot 10^{-7}$ mbar in figure 4.2a to the final pressure of $1 \cdot 10^{-6}$ mbar in figure 4.2b. The differences between both images 4.2a and b are negligible. Directly afterwards (see figure 4.2c) the final oxygen pressure of $1 \cdot 10^{-6}$ mbar is reached and the film oxidizes. The dark germanium areas transform within 11 s (see figure 4.2c to f) into germania.

In figure 4.2a, two areas are labeled and the intensity vs. time plots of these areas are shown in figure 4.2g. Only the LEEM images with a visible change of the morphology are shown in figure 4.2a-f. Afterwards the morphology is constant and the intensity of the dark germania decreases (see figure 4.2g 80- 140s). The intensity vs. time plot shows that the initially bright area with a lower germanium density becomes moderately brighter during the oxidation (black curve). The moderate intensity increase is caused by the adsorption of oxygen and the oxidation of germanium and ruthenium. The dark Ge phase (red curve) shows a strong intensity increase in within 10 s (between 70 and 80 s). This rapid increase indicates a fast oxidation of the high Ge density phase.

The final film (see figure 4.2f) shows a strong contrast and clearly separated phases of the dark germania and bright (germania-) ruthenium. The bright areas are mainly bright after the oxidation and small dark areas agglomerate to the new large dark germania areas. The evolution of the coverage is presented in figure 4.2h as a scheme. The germanium is colored in green on the gray stepped ruthenium support. The coverage of the dark germanium is around 45 %. After the oxidation the dark germania areas cover around 50 % of the ruthenium. The formation of bright excess material on top of a germania layer cannot be observed.

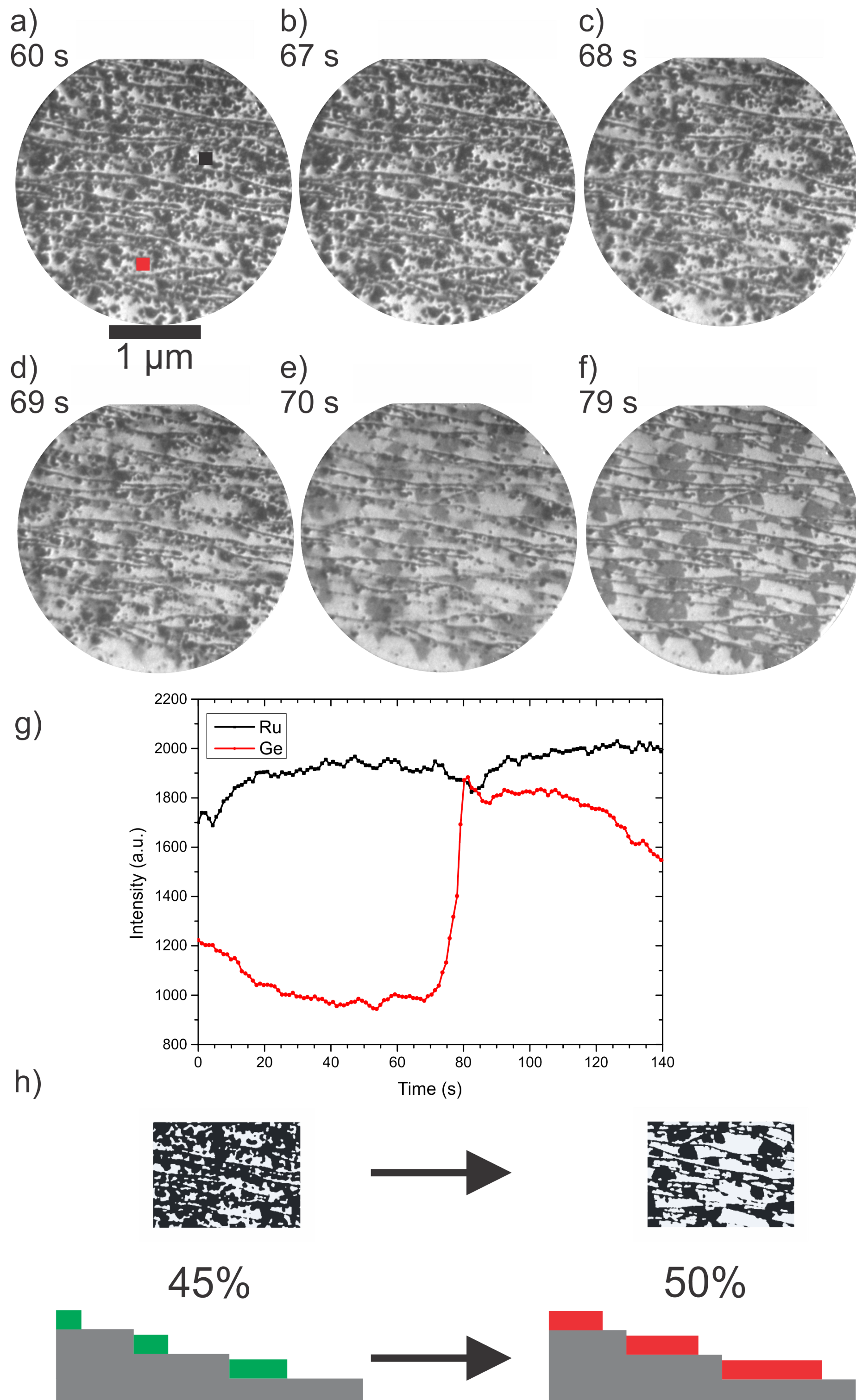

Figure 4.2: Real-time oxidation at 600 K of a 45 % covered germanium film on Ru(0001) (E_{kin} = 6 eV). Oxygen pressure is in a) is $p = 5 \cdot 10^{-7}$ mbar, b)-f) $1 \cdot 10^{-6}$ mbar. a) - f) Oxidation of dark germanium (a) into dark germania (f). g) Intensity vs. time plot of the labeld areas in (a). The dark germanium area shows a fast and huge intensity increase whereby the changes of bright ruthenium area are less. h) determination of the coverage evolution from 45 % to 50 % without the formation of excess material.

In figure 4.3 the structural transformation during the oxidation of germanium on Ru(0001) is presented. The initial germanium film on Ru(0001) shows the (3x3) plus (2x2) superstructure (see figure 4.3a). The adsorption of oxygen ($1 \cdot 10^{-7}$ mbar) leads to the transformation of the sharp (2x2)-Ge/Ru(0001) spots into blurry and weak (2x2) spots. The (3x3) spots are unaffected due to the adsorption of oxygen. The (2x2) spots become more blurry with increasing the oxygen pressure to $1 \cdot 10^{-6}$ mbar at 600 K and the intensity of the (00) spots increases due to the adsorption of oxygen. The (3x3) spots become weaker in figure 4.3c compared to figure 4.3b. During the oxidation, the (3x3) spots disappear (see figure 4.3e) and in figure 4.3f the (3x3) structure has vanished completely. The (2x2) spots of the oxide are blurry and become sharper over time from figure 4.3f to 4.3h. The transformation of the (2x2) plus (3x3) structure into the germania (2x2) structure takes around 120 s. The (2x2) structure orders after the complete transformation. The background of the LEED pattern decreases from figure 4.3d to 4.3h due to the ordering of the oxide. The spots are more blurry at 600 K compared to room temperature due to temperature dependence of scattering, the so-called Debye-Waller factor [154].

The evolution of the LEED spot profiles (SPA-LEED) during the oxidation is shown in figure 4.3i. The SPA-LEED shows the decrease of the (3x3) structure during the oxidation and the broadening of the spots. The SPA-LEED contains information on the domain size distribution [155]. The FWHM of the LEED spot is inverse proportional to the domain size distribution. Therefore, the analysis of the spot profile shows the evolution of the domain sizes distribution. The initial Ge/Ru(0001) films have a FWHM of the (2x2) spot of 3.5 % BZ, the final GeO_2/Ru(0001) films have a FWHM of the (2x2) spot of 9.0 % BZ. The domain size of the Ge/Ru(0001) is around 2.6 times larger than the domain size of the GeO_2/Ru(0001). The huge intensity change of the (00) beam, which is used in LEEM, is clearly visible in the LEED patterns in figure 4.3b to 4.3c.

The LEED spot intensities are shown in figure 4.3j. The intensity of the (00) beam increases by a factor of 1.1 during the oxidation and the intensity of the (2x2) spots stays nearly constant. The intensity of the (3x3) spots decreases to the background intensity.

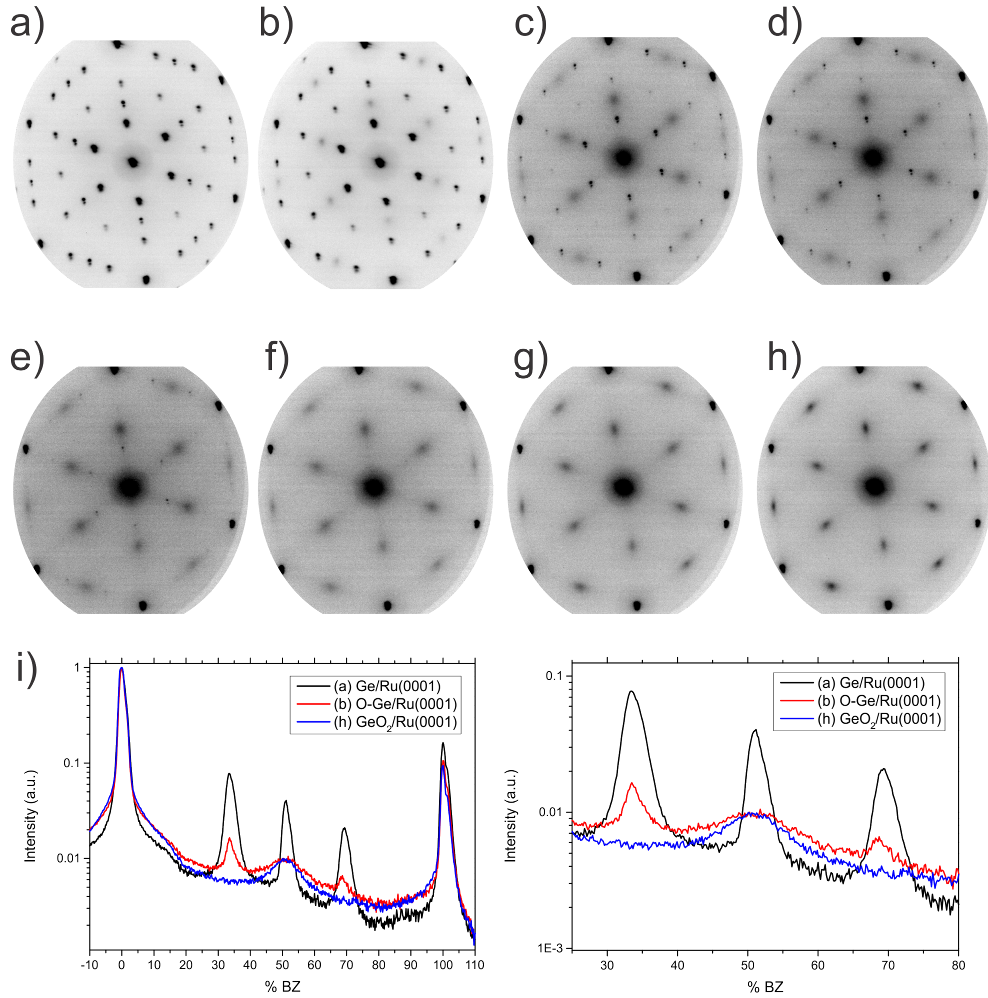

Figure 4.3: Evolution of LEED pattern (E_{kin} = 42 eV) during the oxidation, from the coexisting (2x2) and (3x3) germanium structure to a (2x2) germania structure (T = 600 K) a) UHV, b) p = $1 \cdot 10^{-7}$ mbar O_2, c) p = $1 \cdot 10^{-6}$ mbar O_2, d) 28 s after c), e) 60 s after c), f) 120 s after c), g) 200 s after c, h) 370 s after c). i) SPA-LEED analysis of the LEED pattern a, b and h shows an initial broadening of the LEED spots with the presence of oxygen and the decrease of the (3x3) spots. j) LEED spot intensity over time of the 00 beam, (2x2) spots in red and (3x3) spots in black.

4.1.1 Interpretation

The oxidation of germanium on Ru(0001) can be resolved and observed in real-time by LEEM and LEED. The LEED measurements show the structural transformation from the (3x3) plus (2x2) Ge/Ru(0001) into sharp (2x2) structure of GeO_2/Ru(0001) (see figure 4.3).

The figures 4.1 and 4.2 show the oxidation of germanium in real-time LEEM. The germanium film in figure 4.1 is completely closed. At the ruthenium steps GeO_X is located due to residual oxygen on the ruthenium surface. The LEEM sequence (see figure 4.1) shows that the oxidation starts from the bright areas at the step edges of the ruthenium support (see figure 4.1b-c). The oxide grows from one side of the terrace to the other and the growth has the same direction. After the oxide growth bright areas appear that is accumulated only on one side of the terrace, in particular on the higher level of the substrate.

The partially closed germanium film (see figure 4.2) oxidizes without the formation of excess material on top of a germania monolayer. The film in figure 4.2 expands slightly from 45 % coverage to 50 % coverage. In Figure 4.2, the small dark germania areas agglomerate in ripening process to large germania areas.

The bright areas in figure 4.1k are excess material due to an expansion of the film during the oxidation. The analysis of the coverage shows that the germanium expands during the oxidation. The completely closed germanium film shows 14 % excess material after the oxidation (114 % coverage). Before the oxidation, 16 % of the closed germanium film were already partially oxidized due to residual oxygen on the Ru(0001) surface. Therefore the expansion has to be corrected by the expansion of the GeO_X. The expansion analysis of figure 4.2 leads to an expansion of around 11 % (from 45 % coverage to 50 %). With this factor the initial germanium coverage is around 98 %. This leads to an expansion of the film during the oxidation of around 16 %.

In the work of A. Lewandowski the coexistence of the germania monolayer and bilayer is shown by STM [19]. The LEEM images indicate that the observed excess material is a germania bilayer on Ru(0001). At first, the germania forms a complete monolayer and afterwards, if excess material is present, a second layer is formed, as observed in figure 4.1. With the LEEM images the detailed structure of the germania bilayer cannot be determined. The LEED pattern shows sharp (2x2) spots. The bilayer has either the structure similar to the germania bilayer on Pt(111) in [156] or the bilayer consists of two stacked tetrahedral GeO_4 buiding units in a similar orientation. The germania bilayer on Pt(111) is physisorbed [156] and a bilayer with two in the same orientation stacked tetrahedral GeO_4 would be a chemisorbed structure.

The assumption can be proven by IRAS and by the thermal stability of the bilayer. The silica bilayer on Ru(0001) has a similar thermal stability like the silica monolayer on Ru(0001) [26]. The transformation of the crystalline bilayer into the vitreous one, is a clear indication for the bilayer of the silica-type. In the next chapter the oxidation of a 0.6 nm thick germanium is presented. This shows clearly the desorption of excess material and a complete covering germania monolayer stays on the Ru(0001). This would indicate that the observed excess material is different to a bilayer structure of the silica-type.

The LEEM measurement in figure 4.1 shows transformation of the Ge/Ru(0001) film into the GeO_2/Ru(0001) film within 77 s, whereas the structural transformation from the (3x3) plus (2x2) Ge/Ru(0001) into sharp (2x2)-GeO_2/Ru(0001) spots (see figure 4.3) takes around 120 s at similar temperature and oxygen pressure. The decrease of the (3x3) phase is on a similar time scale compared to the change of the 00 beam. The spot intensity of the initial (2x2) structure stays approximately constant during the oxidation (see figure 4.3j). However the oxidation of the partially closed Ge film (see figure 4.2) takes around 11 s. The ruthenium in figure 4.1 and 4.3 is nearly completely covered by germanium. This shows that the oxidation time depends on the initial germanium coverage and indicates the influence of the ruthenium support for the germanium oxidation.

From the real-time LEEM and LEED measurement of the germanium oxidation a mechanism for the germanium oxidation can be proposed. The ruthenium support has a huge influence on the germanium oxidation. Oxygen strongly chemisorbs on Ru(0001) and forms well-ordered adlayers [121]. The chemisorbed oxygen is dissociated. A 3O-(2x2)-Ru(0001) is formed underneath the silica bilayer [26]. Also for the germania monolayer the presence of the 3O-(2x2)-Ru(0001) is reported [9]. The real-time measurement in figure 4.1 shows that the oxidation starts at one side of the atomically flat terrace of the substrate. The growth starts at the atomic steps, this indicates that the oxidation takes place at the GeO_X / Ge interface. Therefore the oxygen might diffuse through defects and oxidizes the germanium. However the oxidation is related to the support.

The oxidation of the partially closed germanium film (see figure 4.2) shows that the germanium oxidizes within 11 s in contrast to slower oxidation of the completely closed germanium film. That indicates that the ruthenium is a catalyst for the oxidation. In figure 4.2 the ripening of small germania islands can be observed. That indicates that germania can diffuse on Ru(0001). Therefore, it can be concluded that the germanium oxidized at the interface between the ruthenium and the germanium island.
The deposition of germanium on 3O-(2x2)-Ru(0001) shows clearly the partial oxidation of germanium (see chapter 3). That shows that the germanium reacts with the chemisorbed oxygen of the Ru(0001). First the germanium oxidizes completely and afterwards the 3O-(2x2)-Ru(0001) adlayer is formed underneath the germania film. The tetrahedral GeO_4 units rearrange during the formation of the oxygen adlayer.

4.2 Oxidation of 0.6 nm thick germanium on Ru(0001) - a case study

In the following part the oxidation of a 0.6 nm thick germanium film on Ru(0001) is presented. The thickness of 0.6 nm is equivalent to around 3 - 4 monolayers germanium and the deposited thickness would lead to around 2-3 germania bilayers. The germanium was deposited in the preparation chamber, in contrast to the deposition directly in the measurement chamber. The thickness was calibrated with a quartz crystal microbalance (QCM). The calibration of the germanium evaporator was done at the deposition position with the QCM. The sample was annealed in UHV to around 540 K. The figure 4.4 shows the sample before the oxidation. In figure 4.4a and 4.4b two LEEM images of the germanium film are shown. The LEEM images show bright areas in the range of less than 100 nm size. The associated LEED pattern is shown in figure 4.4c. The LEED pattern shows diffuse LEED spots, which are located at the (3x3) positions.

For an enhanced ordering of the germanium film, the sample was annealed for a second time in the measurement chamber in UHV to 490 K. After the second annealing, the germanium film shows a strong contrast in Ge3d XPEEM (see figure 4.4d-e) and LEEM (see figure 4.4f). The XPEEM scan of the Ge3d core level is shown in figure 4.4g. The XPEEM scan shows two components, which are visible in the XPEEM images of figure 4.4d and 4.4e and in the LEEM image 4.4f. The dark area in the LEEM image corresponds to the bright area in the XPEEM image 4.4d, which is labeled in the XPEEM scan (see figure 4.4g) as area A. The area B is bright in the LEEM image 4.4f and also bright in the XPEEM image 4.4e. The area A has the maximal intensity at lower kinetic energies compared to the area B. The area B can be related to additional germanium on top of a closed germanium film on Ru(0001). The associated LEED pattern in figure 4.4h shows split LEED spots.

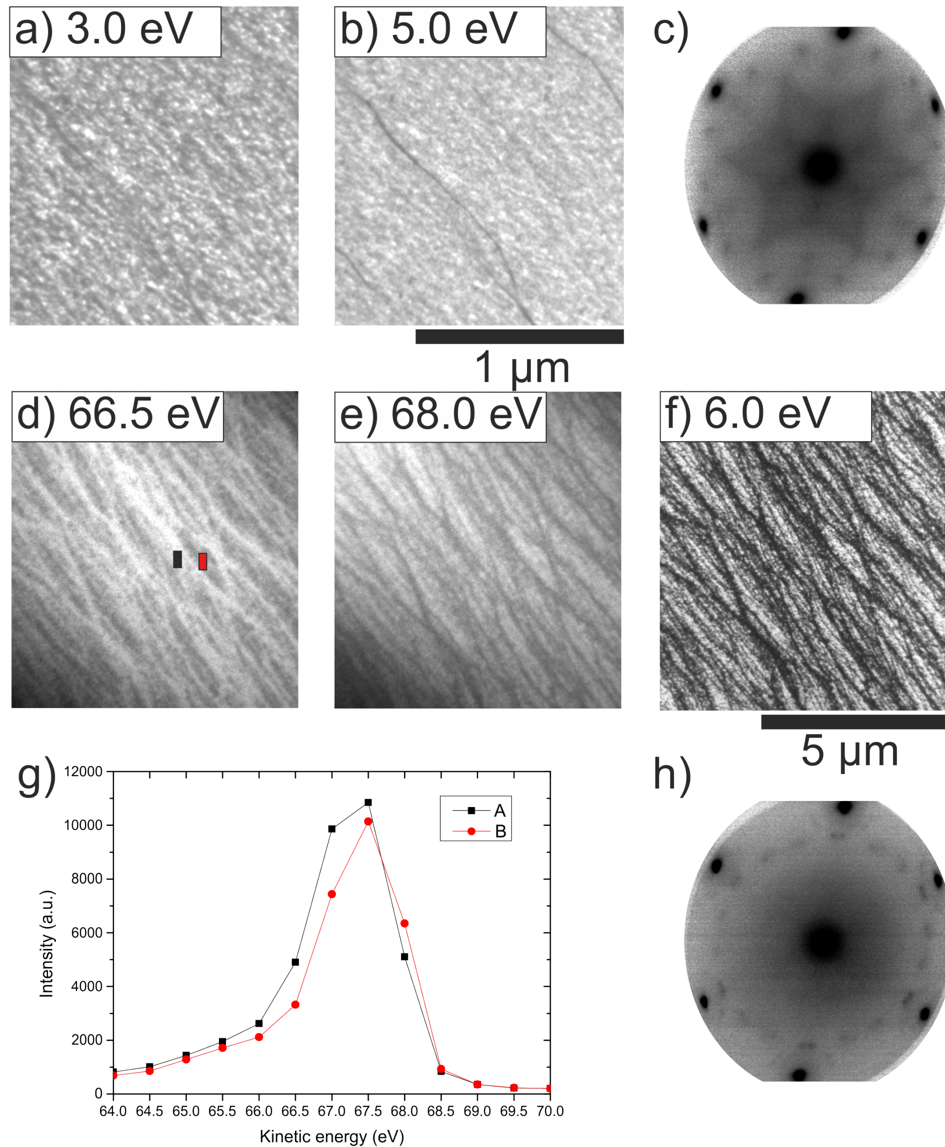

Figure 4.4: 0.6 nm thick germanium film on Ru(0001). a) and b) LEEM images after transfer into the measurement chamber, c) associated LEED pattern (42 eV), d) and e) Ge3d XPEEM images (hν = 100 eV) after the second annealing in UHV to 490 K, f) LEEM image associated to the Ge3d XPEEM, g) XPEEM scan with two shifted components (hν = 100 eV), h) LEED pattern (42 eV) after the second annealing

The figure 4.5 shows the film after the first oxidation. The 0.6 nm thick germanium film was oxidized with comparable conditions to the real-time oxidations of the previous part. The germanium film was oxidized at 610 K in $1 \cdot 10^{-6}$ mbar O_2 for 10 min. The Ge3d XPEEM images (see figure 4.5a-b) show two different components of the Ge3d core level. The contrast of the XPEEM images switches from figure 4.5a to figure 4.5b that shows the incomplete oxidation of the film. The figure 4.5c shows a zoomed in LEEM image of the GeO_X film. The LEEM image shows bright

areas A (labeled black) and dark areas B (labeled red). The bright areas in the LEEM image are also bright in the XPEEM image of figure 4.5b. The bright area A and dark area B have a different MEM-LEEM transition (see figure 4.5d). The difference of the work function is around 0.1 eV. The Ge3d XPEEM scan shows two components which are slightly shifted (see figure 4.5e). The labeled area A shows higher intensity compared to area B at higher kinetic energies, hence at lower binding energies. The LEED pattern of the film is presented in figure 4.5f and shows blurry (2x2) spots with a ring around the (1x1) spots.

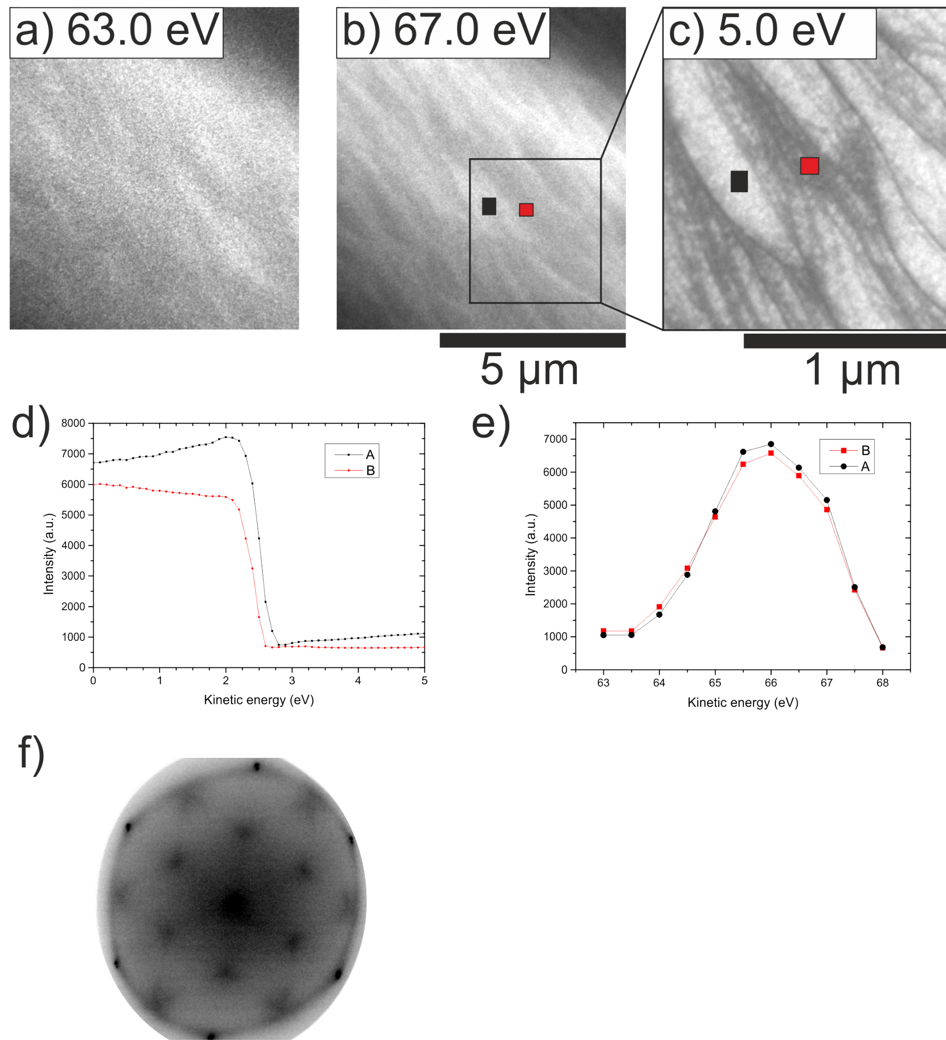

Figure 4.5: Oxidation of 0.6 nm thick germanium film on Ru(0001) (T = 610 K, p = 1 $\cdot$ 10^{-6} mbar O_2, 10 min). a) and b) Ge3d XPEEM images (hν = 100 eV) c) associated LEEM image (zoomed in), d) MEM-LEEM transition of the labeled (in c) areas A (black) and B (red). Both areas show a MEM-LEEM difference of 0.1 eV. e) Ge3d XPEEM scan with the labeled areas A and B. f) LEED pattern (42 eV) with blurry (2x2) spots and a ring structure.

The figure 4.6 shows the evolution of LEED pattern during the second annealing in oxygen to 770 K in $1 \cdot 10^{-6}$ mbar O_2. The blurry (2x2) LEED pattern with the ring in figure 4.6a becomes a sharp (2x2) LEED pattern with a low background (see figure 4.6f). The intensity over temperature plot shows the increase of the spot intensities at temperatures above 740 K for the 00 beam and 760 K for the (2x2) spots.

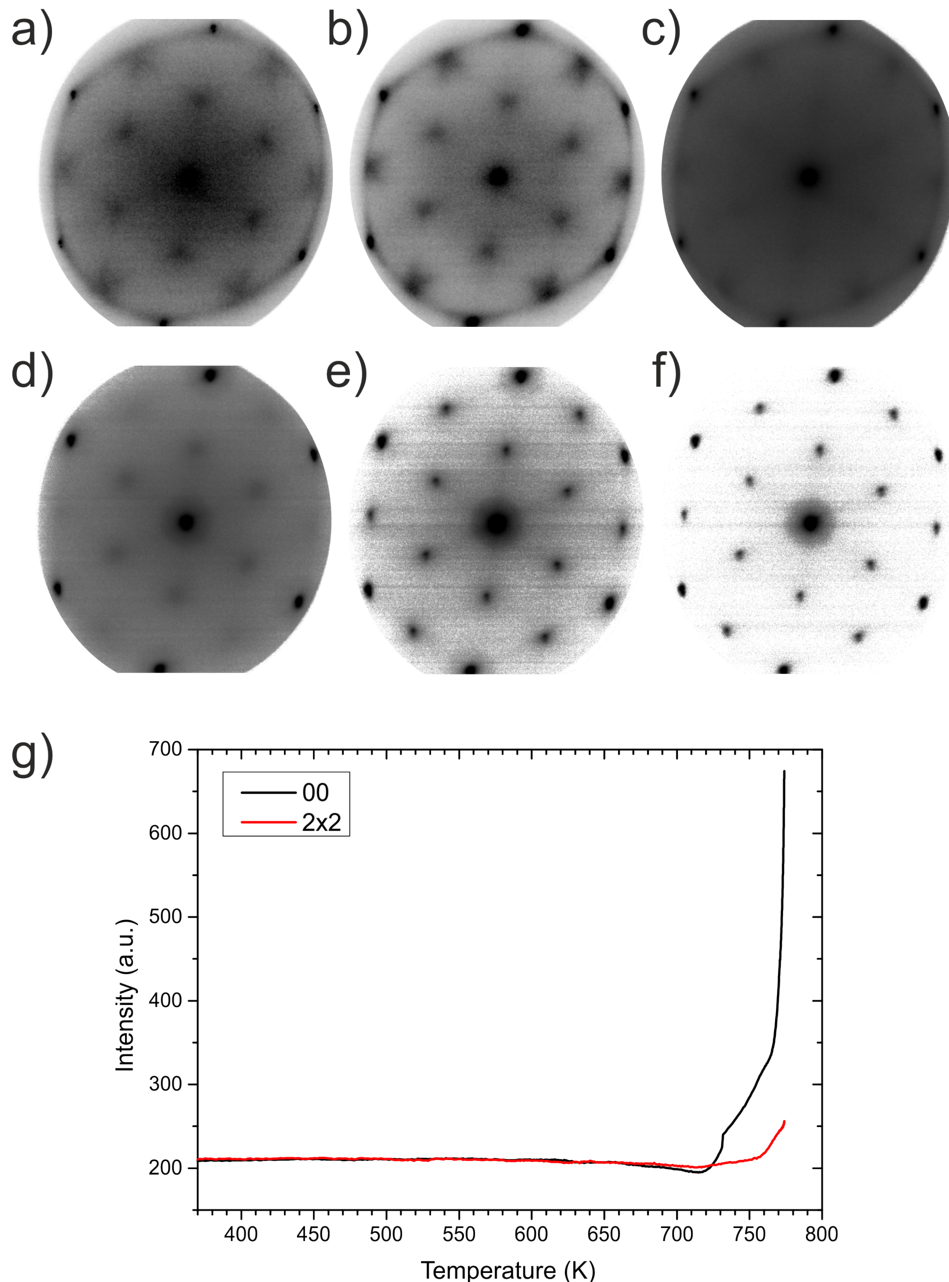

Figure 4.6: Evolution of LEED pattern (42 eV) of GeO_X during the second oxidation ($1 \cdot 10^{-6}$ mbar O_2) to 770 K. a) at room temperature, b) 720 K, c) 740 K, d) 750 K, e) 760 K, f) 770 K and g) spot intensities over temperature of the 00 spot and the (2x2) spots.

In figure 4.7 the LEEM-IV, Ge3d XPEEM and LEED measurements of the final GeO_2 film are presented. In figure 4.7a the LEEM image shows a homogeneous germania film. The associated Ge3d XPEEM in figure 4.7b and c shows also a homogeneous image, in contrast to the GeO_X film (see figure 4.5). The comparison of the LEEM-IV curves of the final GeO_2 film after the second annealing (blue) and the GeO_X film after the first annealing (black and red) shows for the GeO_2 film more prominent features and a higher work function. The area A (bright) of the GeO_X film shows a broad peak around 6 eV and the dark area B show an intensity decay. The germania film shows a (2x2) LEED pattern with sharp LEED spots and a low background after the second annealing to 770 K in oxygen atmosphere (see figure 4.7e).

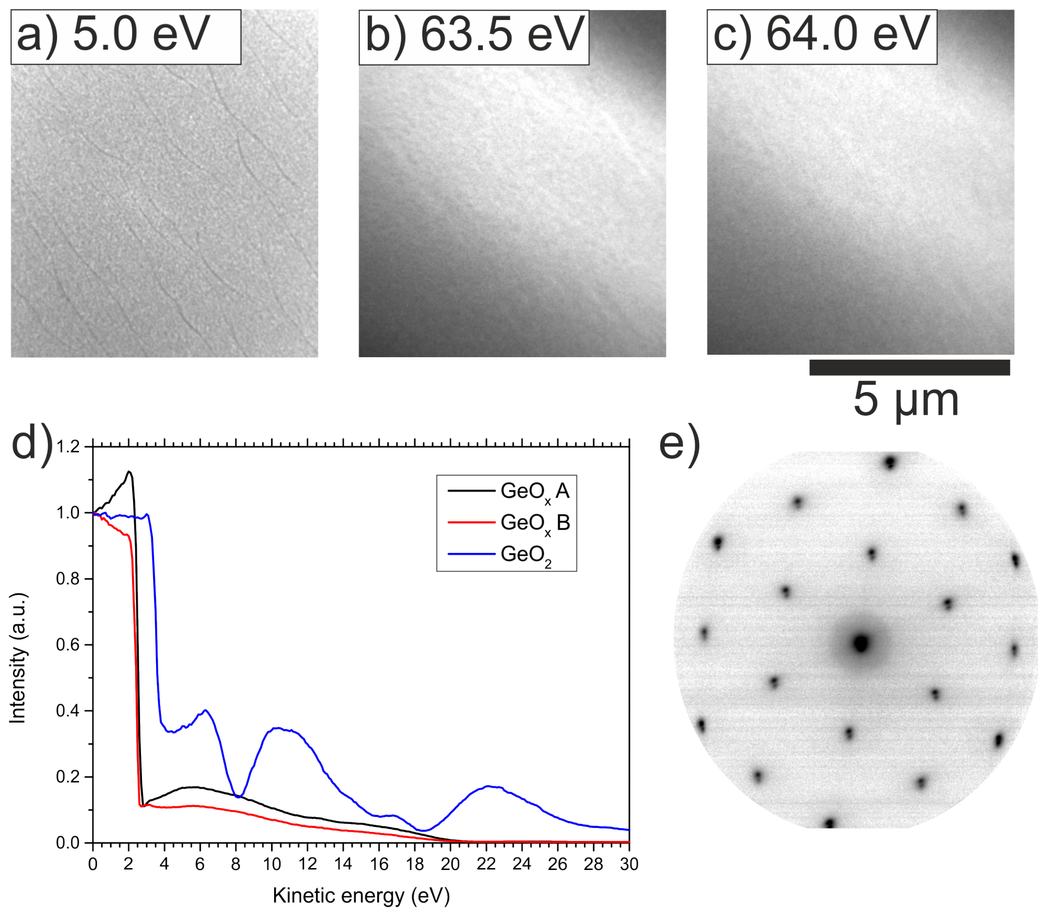

Figure 4.7: Germania film after the second annealing to 770 K in $1 \cdot 10^{-6}$ mbar O_2. a) LEEM image, b) and c) Ge3d XPEEM (hν = 100 eV), d) LEEM-IV comparison of the film after the first annealing to 600 K (black and red) and the second annealing to 770 K (blue), e) (2x2) LEED pattern (42 eV) of the final GeO_2 film.

The XPS measurements are collected in figure 4.8. In figure 4.8a, the Ge3d core levels for the 0.6 nm thick germanium film after the first oxidation to 610 K in $1 \cdot 10^{-6}$ mbar with the Ge3d core level after the second oxidation to 770 K are compared.

The XPS of Ge3d after the annealing to 610 K shows that the germanium is incompletely oxidized. The Ge3d has a binding energy of 30.5 eV with a shoulder at lower binding energies. The oxidation at 770 K leads to a shifting of the Ge3d core level by 0.8 eV and only a single peak is observed.

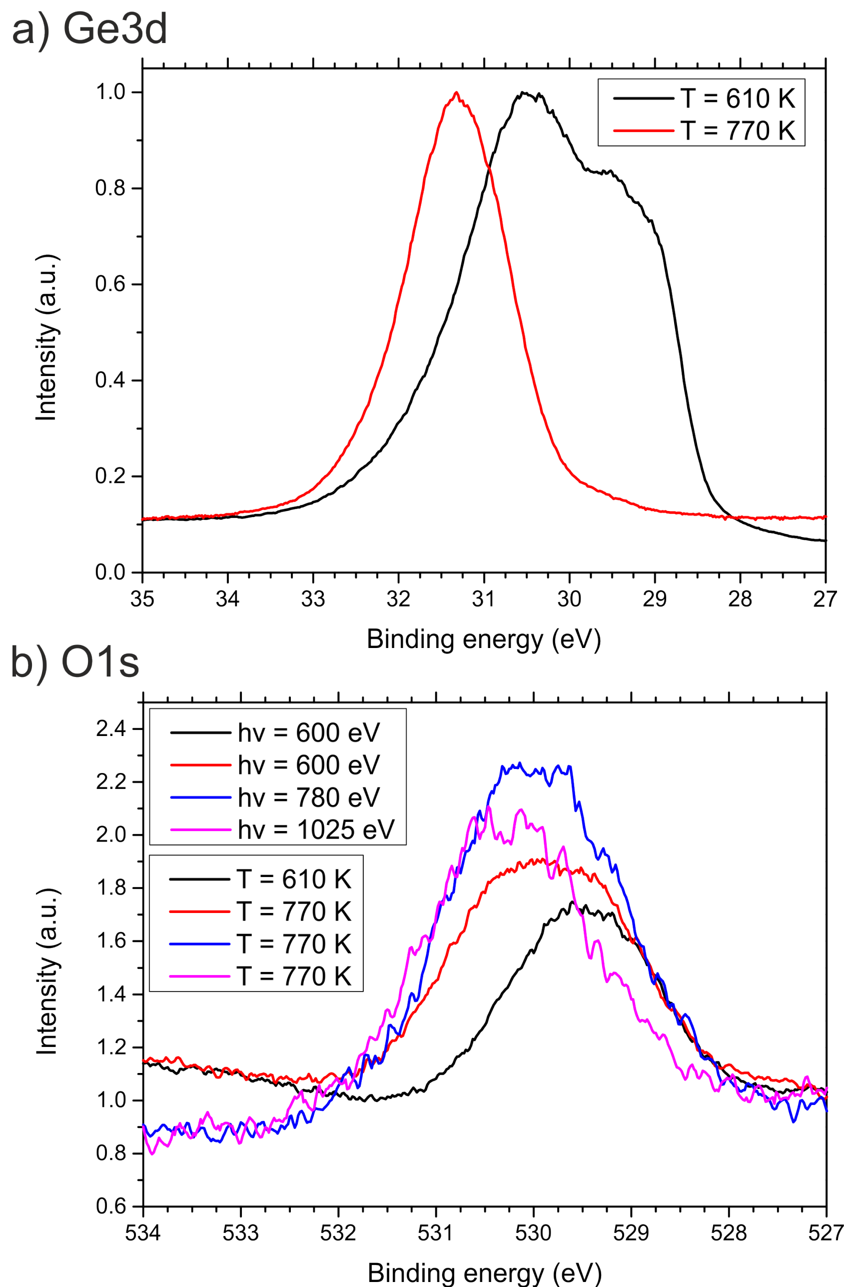

Figure 4.8: Comparison of the XP spectra of the Ge3d and O1s core levels after the first annealing to 600 K and second annealing to 770 K in oxygen. a) Ge3d core level (hν = 100 eV) after the first (black) and second annealing (red). The germanium becomes completely oxidized after the second annealing. b) O1s core level spectra of the different annealing temperature with different photon energies.

In figure 4.8b the XP spectra of the O1s core level are shown. The XP spectrum in black shows the O1s core level after the first oxidation to 610 K. The peak maximum is at around 529.5 eV. The O1s core level after the annealing to 770 K shows the formation of a new component at around one eV higher binding energy. For more detailed information, the XPS was measured with different photon energies for probing different the mean free path of the photo electrons. The XP spectrum with 780 eV photon energy (in blue) shows the main intensity at around 530 eV binding energy and a shoulder at around 529 eV. The XP spectrum with 1025 eV photon energy (in pink) has a maximal intensity at around 530.5 eV and the component at lower binding energies vanished.

4.2.1 Interpretation

The oxidation of a 0.6 nm thick germanium film on Ru(0001) is different from that of the thin germanium films shown in the previous part. After the deposition, the germanium film shows inhomogeneous LEEM and XPEEM images. The LEEM images in figure 4.5a and b show bright areas. The bright areas might be three-dimensional germanium islands on top of a germanium wetting layer due to the Stranski-Krastanov growth mode. The LEED pattern of the 0.6 nm thick germanium film shows a diffuse pattern with (3x3) spots after the deposition in the preparation chamber (see figure 4.4c). The diffuse LEED pattern indicates a poor long-range order of the film.

A second annealing in UHV leads to sharp LEED spots (see figure 4.4h) and the contrast in LEEM (see figure 4.4f) becomes stronger compared to the LEEM images after the deposition. After the second annealing the Ge3d XPEEM scan shows clearly two components of the Ge3d core level (see figure 4.4g). The two components are correlated to the LEEM image (see figure 4.4d-f). The component which has a maximal intensity at 68 eV kinetic energy correlates with the bright areas in the LEEM image at 6 eV. This component might be related to three-dimensional islands on the wetting layer which appear dark in the LEEM image (see figure 4.4f). The XPEEM shows that the wetting layer is bright at lower kinetic energies, which is related to a higher binding energy of the germanium. The spin-orbit splitting of the Ge3d core level is not resolved in the XPEEM scan at a step width of 0.5 eV.

The oxidation treatment which oxidizes a “thin” germanium film completely (previous part) leads to an incompletely oxidized “thick” germanium film. The observed chemical shift of the Ge3d core level in figure 4.8a is around 0.8 eV and around 1.6 eV for the shoulder from the incompletely oxidized germanium to the GeO_2. The chemical shift of 0.8 eV is related to the formation of one germanium oxidation state [157]. In addition, the O1s core level changes during the complete oxidation and shifts towards higher binding energies, which is related also to the formation of the Ge^{4+} species. At larger mean free path of the photoelectrons the O1s components are more prominent at higher binding energies.

The XPS of the oxygen core level shows that the oxygen components with the lower binding energy are located at the surface and the components with the higher binding energies are located at the interface to the ruthenium support.

With the chemical information of the XPS, the LEEM and LEED images of the 0.6 nm thick germanium film during the oxidation can be interpreted. The bright areas in figure 4.5c show a higher kinetic energy or lower binding energy in XPEEM and a higher work function in the MEM-LEEM transition. The LEED pattern in figure 4.5f indicates a poor long-range order of the surface. The bright areas could be related to a three-dimensional GeO_X network on top of an also incompletely oxidized GeO_X film. This could lead to the ring structure in the LEED pattern of figure 4.5f.
The evolution of the LEED pattern in figure 4.6 during the second annealing to 770 K shows that the final LEED pattern has sharp spots with a low background, compared to the initial LEED pattern. This indicates the ordering and formation of a good long-range order of the surface during the annealing. The strongly increasing LEED spot intensities at above 740 K for the 00 beam and 760 K for the (2x2) spots could be related to the desorption of the incomplete oxidized three-dimensional GeO_X network and the simultaneous formation of a GeO_2 monolayer on the ruthenium. Due to the Debye-Waller factor, the LEED intensity at high temperatures decreases [154]. The LEEM image and Ge3d XPEEM images in figure 4.7 show a homogeneous GeO_2 film without the bright areas of figure 4.5. This observation is in line with the theoretical calculation that the germania monolayer is the preferred germania structure on Ru(0001) [19][9].

4.3 Germania on Ru(0001)

In this part, the germania film on Ru(0001) is discussed on a mesoscopic scale. The detailed knowledge of the thickness of ultra-thin films is fundamental. On Ru(0001) ultra-thin silica films can be prepared as the chemisorbed monolayer and the physisorbed bilayer [26]. The monolayer and bilayer can form a (2x2) LEED pattern, but the IV curves are different. A detailed study of the thickness calibration of silica by LEEM and LEED measurements can be found in [32]. At room temperature the silicon grows as a disordered film that leads to a decay of the LEED intensity during the deposition [32]. This intensity decay can be used to calibrate the finial thickness of the silica film [32]. This method is very reliable. The silica system is self-aligning regarding the final thickness. If more than the equivalent of a bilayer silicon is deposited, the excess SiO_2 desorbs and the final film is a silica bilayer.

Therefore, the thickness calibration of the germania and germania-silica films plays an important role. The distinction between the monolayer and bilayer germania is hard by LEEM. However, LEED-IV analysis gives detailed information on the structure of the film [82]. This was done by A. Lewandowski and co-workers for the germania monolayer on Ru(0001) [9]. The SMART microcope can be also used for LEED-IV measurements. Therefore, the LEED-IV curves of the germania films can be compared to identify the germania film thickness of the present work.

Figure 4.9 shows the comparison of the (01) spot form [9] (black IV curve), with a germania film, prepared for this thesis (red IV curve). The comparison shows a very good agreement with the reference LEED-IV curve. All peaks are at same positions, but the reference LEED-IV curve shows more prominent peak intensities for energies higher than 325 eV compared to the (01) beam of the present work. This might be related to beam induced effects because the flux density of the electron beam in the microscope is much higher than in the LEED apparatus (20 μm spot size compared to around 1 mm at comparable flux). Therefore, it can be concluded that the germania films are similar to the described germania monolayer in [9].

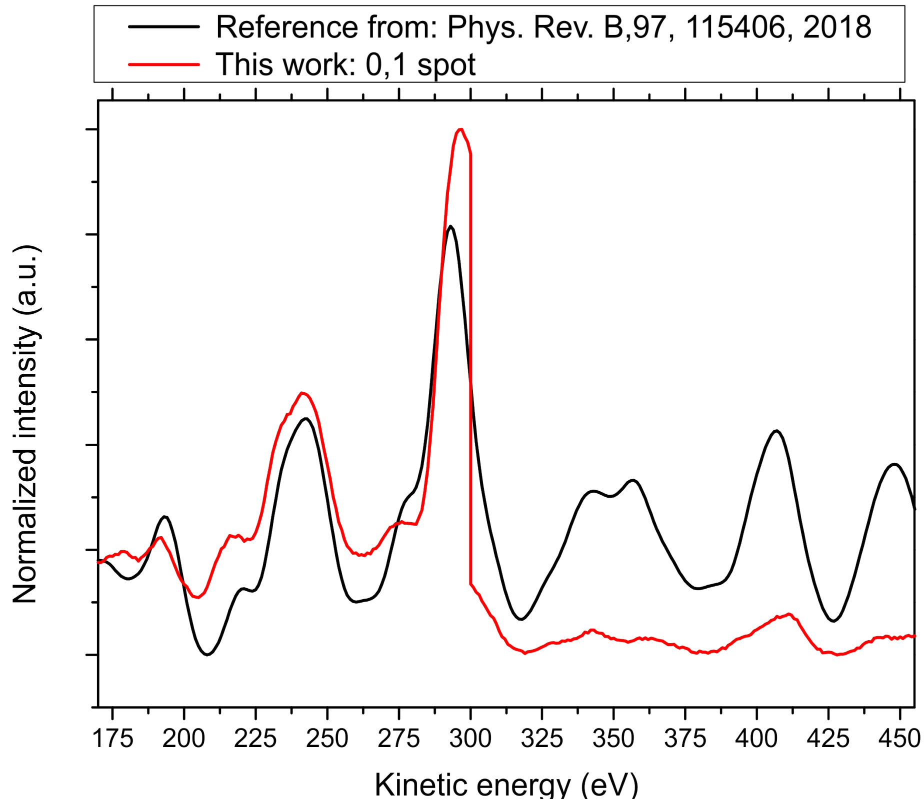

Figure 4.9: LEED-IV comparison of the (01) beam of a monolayer germania on Ru(0001). The reference intensity (black) is taken from [9] and the red curve is measured by the SMART microscope. Both curves show the peaks at similar energies, which is a good accordance.

Two different preparation recipes for the preparation of ultra-thin germania films were used. In addition to the previously described growth of germanium on bare ruthenium at 540 K and the oxidation, one further approach was used: germanium deposition on an oxygen covered 3O-(2x2)-Ru(0001) surface at room temperature and additionally the annealing in oxygen atmosphere to 600 K. Germanium partially oxidizes at room temperature by consuming the oxygen from the ruthenium surface, as shown in the previous chapter 3.

Figure 4.10 compares the LEEM measurements of the two differently prepared germania films on ruthenium support in comparison to the LEEM-IV curve of bare Ru(0001) and 3O-(2x2)-Ru(0001). In figure 4.10a, a LEEM image of germania prepared on 3O-(2x2)-Ru(0001) is shown. The film shows a homogeneous bright image at 5 eV. The atomic steps of the ruthenium support are visible. The germania film prepared on bare Ru(0001) at 540 K in UHV is shown in figure 4.10b and 4.10c. Here the germania film shows a strong contrast which is inverted between the image at 4 eV and 5 eV. Three different contrasts are visible and labeled in the image.

The MEM-LEEM transition of all different contrasts of the images 4.10b and c are shown in figure 4.10e. The high intensity of area 1 is related to a focus effect of the needle domains. All selected areas have different work functions. The MEM-LEEM transition of germania prepared on 3O-(2x2)-Ru(0001) is at 2.93 eV kinetic energy. The MEM-LEEM transitions of the different germania areas are 3.37 eV for area 1, 3.14 eV for area 2 and 3.06 eV for area 3. The work function of bare Ru(0001) is 5.52 eV [141] and the measured MEM-LEEM transition of clean Ru(0001) is 2.5 eV. The offset of 3.02 eV has to be added to the measured MEM-LEEM transition. The 3O-(2x2)-Ru(0001) surface has a work function of 6.71 eV. The work function of germania prepared on 3O-(2x2)-Ru(0001) is 5.95 eV. The work functions of germania of the different germania areas are 6.39 eV for area 1, 6.16 eV for area 2 and 6.08 eV for area 3.

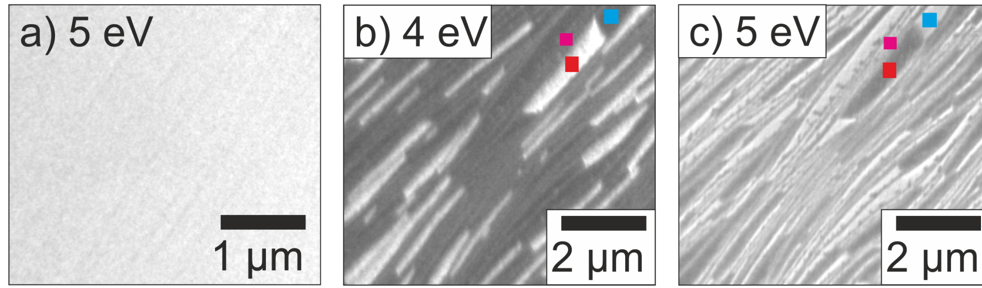

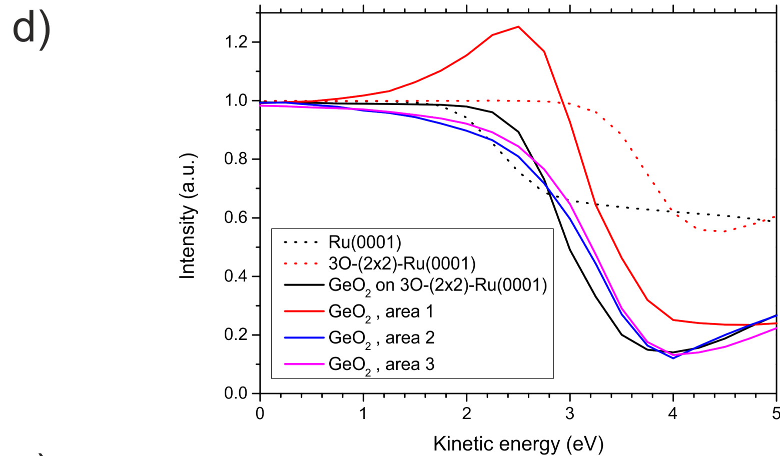

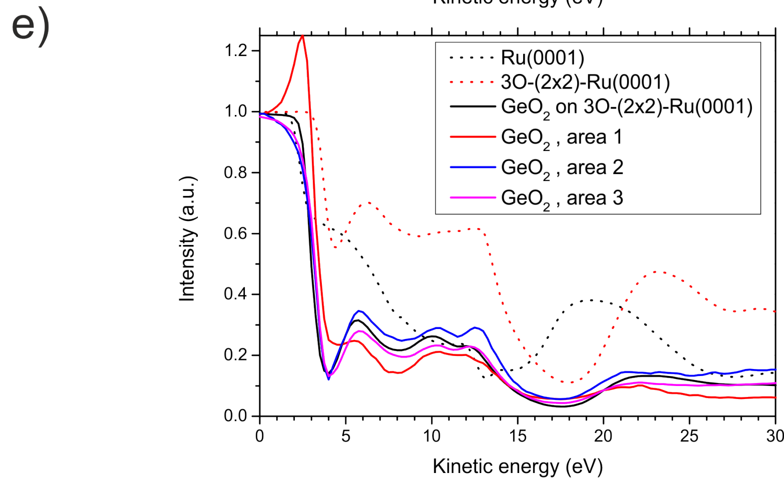

Figure 4.10: a) LEEM image (E_{kin} = 5eV) of germania grown on 3O-(2x2)-Ru(0001) at RT; LEEM (E_{kin} = 4 eV) germania grown on bare Ru(0001) at 540 K b) LEEM (E_{kin} = 4 eV) and c) LEEM image (E_{kin} = 5 eV), d) MEM-LEEM transition measurements of the different areas labeled in b) combined with the LEEM-IV curves of 3O-(2x2)-Ru(0001) and bare Ru(0001) and e) LEEM-IV of the different areas labeled in b) combined with bare Ru(0001) and 3O-(2x2)-Ru(0001).

The core level spectroscopy of GeO_2 on Ru(0001) is presented in figure 4.11. In figure 4.11a, the XPS of Ge3d is shown and in figure 4.11b, the XPS of the O1s. The maximum of the Ge3d is at 31.7 eV BE and the FWHM of the Ge3d core level is 1.55 eV.

The Ge3d core level of GeO_2 shows one peak in contrast to Ge on Ru(0001). The spin-orbit splitting is clearly observed for Ge on Ru(0001) (see chapter 3, figure 3.8). The peak width of the $Ge3d_{3/2}$ and $Ge3d_{5/2}$ is broadened inhomogeneously due to the oxidation.
The O1s core level of the germania monolayer is shown in figure 4.11b. The O1s core level contains two components; one component is related to Ge-O and the other one to O-Ru. The component related to O-Ru has a lower binding energy (529 eV) [146] compared of the Ge-O component (530 eV).

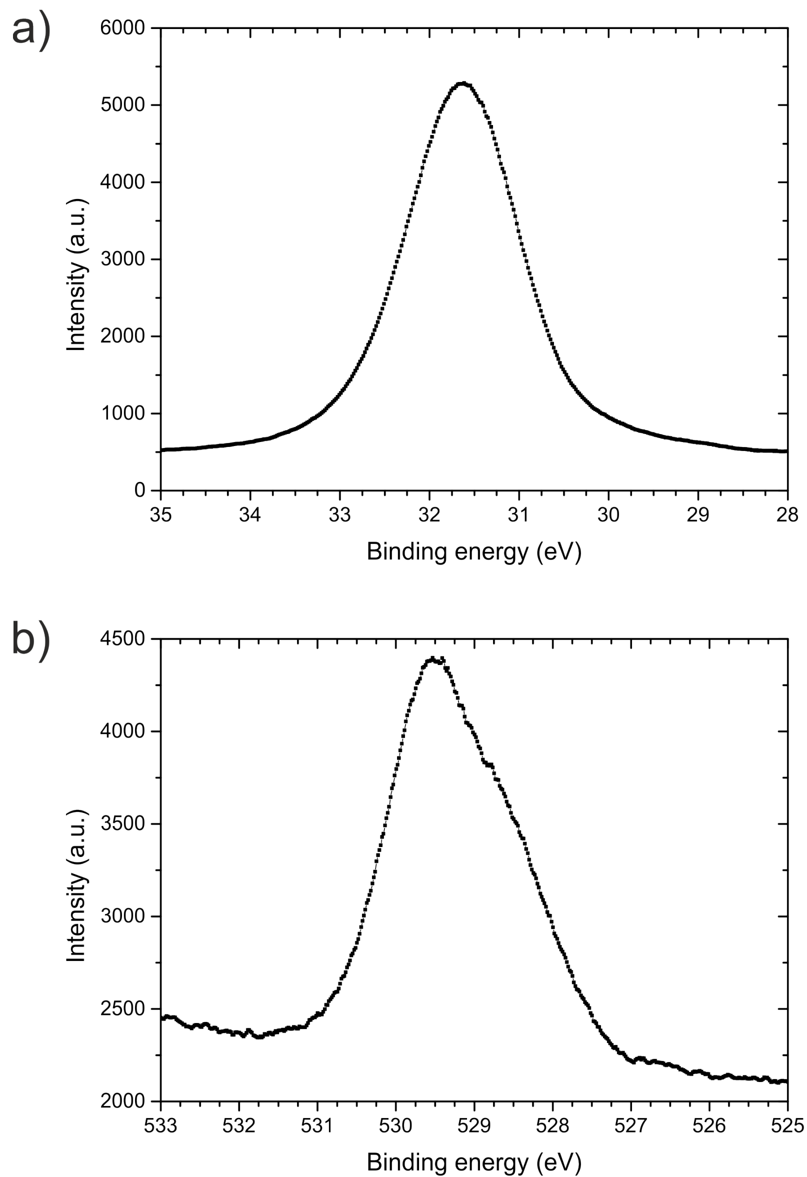

Figure 4.11: XPS of a germania monolayer on Ru(0001): a) Ge3d core level (hν = 100 eV) and b) of O1s core level (hν = 600 eV).

4.3.1 Interpretation

The LEED-IV measurements (see figure 4.9) of the germania film on Ru(0001) are in line with the LEED-IV measurements of A. Lewandowski and co-workers [9]. The germania forms a monolayer structure on Ru(0001) that is determined in the work of A. Lewandowski and co-workers [9].

The germania films in figure 4.10 have a thickness of more than one monolayer and are prepared identically except of the oxygen coverage of the Ru(0001) support. The germania film in figure 4.10a that is prepared on 3O-(2x2)-Ru(0001) shows a homogeneous intensity distribution. Additional germania on top of a closed monolayer could be distributed homogeneously in small domains. As the film is prepared by growing at 540 K, the additional germania can accumulate and form micrometer size needle domains on top of the germania monolayer. The LEEM images (see figure 4.10 b and c) of the germania show three different areas which can be related to different germania thicknesses. However, a direct determination of local thicknesses is not possible by LEEM. Area 1 shows a higher work function and higher damping at higher kinetic energies (>6 eV), this could be related to additional germania on top of a closed germania layer.

The comparison of the LEEM-IV curve of 3O-(2x2)-Ru(0001) with the germania LEEM-IV curves show the main features of the 3O-(2x2)-Ru(0001) LEEM-IV curve with modulation of the germania. The LEEM-IV curve of bare Ru(0001) shows different features. A detailed analysis of the reflection of low-energy electrons from the Ru(0001) can be found elsewhere [32] [140] [158]. The germania films show in LEEM-IV three peaks, at 6 eV and a double peak at 10 eV and 13 eV. The comparison germania LEEM-IV curves of the two differently prepared germania films on ruthenium show that the films are very similar except for the labeled area 1, the bright areas at 4 eV. The labeled germania areas 2 and 3 show minor differences, mainly the shifted work function.

The XPS of the Ge3d core level (see figure 4.11a) shows that the germanium has an oxidation state of 4+ that is related to two bonding oxygen atoms and leads to stoichiometry of GeO_2. The O1s core level contains two components which can be related to Ge-O and O-Ru bonds. That is also in line with the presented germania monolayer structure in [9].

4.4 Conclusion

The real-time measurements of the germanium oxidation show a slight expansion of the coverage. The structure of the film changes from the coexisting (2x2) and (3x3) structure into a (2x2) germania monolayer structure. The oxidation time depends of the germanium coverage. Depending of the initial germanium coverage, the formation of excess material can be observed. The excess material on top of a germania monolayer desorbs at temperatures above 770 K which indicates that the germania excess material on Ru(0001) is not comparable to the silica bilayer. Only crystalline germania films could be prepared on Ru(0001). After annealing to 770 K only crystalline germania monolayer films could be observed.

5 Preparation and thermal stability of ultra-thin germania-silica films on Ru(0001)

The tailoring of ultra-thin oxides like the modification of silica offers many opportunities for catalysis and improves the fundamental understanding of those films. Modified silica is a common used catalyst, however silica is catalytically inactive, but the modification by catalytically active elements or compounds might activate the silica [41]. The ultra-thin silica system is a model system for the complex catalyst and accessible to surface science methods [54]. In addition, the ultra-thin silica system was modified by various catalytically active metals, for example with iron [47] [48], titanium [46], aluminum [45] and chromium [43].

In the present work ultra-thin germania-silica films on metal supports, in particular Ru(0001), have been studied for the first time. Due to the novel surface science approach for the preparation of ultra-thin germania-silica films on metal single crystals, the preparation conditions must be found. Atomic layers of GeO_2- SiO_2 films can be prepared by chemical vapor deposition [159]. Bulk germania-silica glasses can be prepared by chemical vapor deposition soot-remelting method [160] or by a sol-gel process [21]. In the present study, the ultra-thin films were prepared by electron beam physical vapor deposition in UHV or in oxygen atmosphere ($2 \cdot 10^{-7}$ mbar O_2) and annealing in $1 \cdot 10^{-6}$ mbar O_2. For finding preparation conditions synchrotron based spectro-microscopy offers the opportunities of studying chemical and structural properties in real time and in-situ of the different preparation steps. In particular, the determination of the chemical composition is important to identify a successful preparation of ultra-thin germania-silica films on Ru(0001).

In this chapter well-defined ultra-thin germania-silica films on Ru(0001) are prepared with two different recipes. In the first part, the deposition of silicon on a germania film will be presented. In the second part, the deposition of germanium on silica will be shown. For a well-ordered and fully oxidized structure, the films require an annealing in oxygen atmosphere. It turned out that the degree of order of the initial film has a huge influence on the final germania-silica film.

5.1 Germania with silica on top

5.1.1 SiO_X on (2x2)-GeO_2

The preparation of germania-silica on Ru(0001) was studied by adding 1.9 ML silica on top of a partially closed germania film. The germania films was prepared as presented in chapter 4 by germanium deposition in UHV at 540 K on bare Ru(0001) and the oxidation at 600 K in $1 \cdot 10^{-6}$ mbar O_2. LEEM and LEED comparisons during the preparation steps are presented in figure 5.1. In figure 5.1a the initial (2x2) LEED pattern of the GeO_2 is shown. The associated LEEM image (see figure 5.1b) shows an incomplete germania film with small dark areas at the atomic steps of the ruthenium support. The dark germania areas exhibit mainly a triangular shape and have a size of around 100 nm. The germania coverage is 0.1 ML. After the deposition of silicon, all spots except for (00) vanish (see figure 5.1c). This means, the surface is fully disordered, due to the silicon deposition. The LEEM image in figure 5.1d shows the germanium as diffuse dark areas at the areas of the former well-ordered germania areas.

The LEEM-IV curves of the partially closed germania film are shown in figure 5.1e. For the dark and bright areas in figure 5.1b they are different from the 3O-(2x2)-Ru(0001) reference LEEM-IV curve. The bright area contains germanium with a low density, as shown in chapter 3. The LEEM-IV analysis of the films shows a decrease of the work function by the deposition of silicon on germania by about 1.05 eV. The LEEM-IV curve of the amorphous silicon shows a decay of the intensity and the structural features vanished.

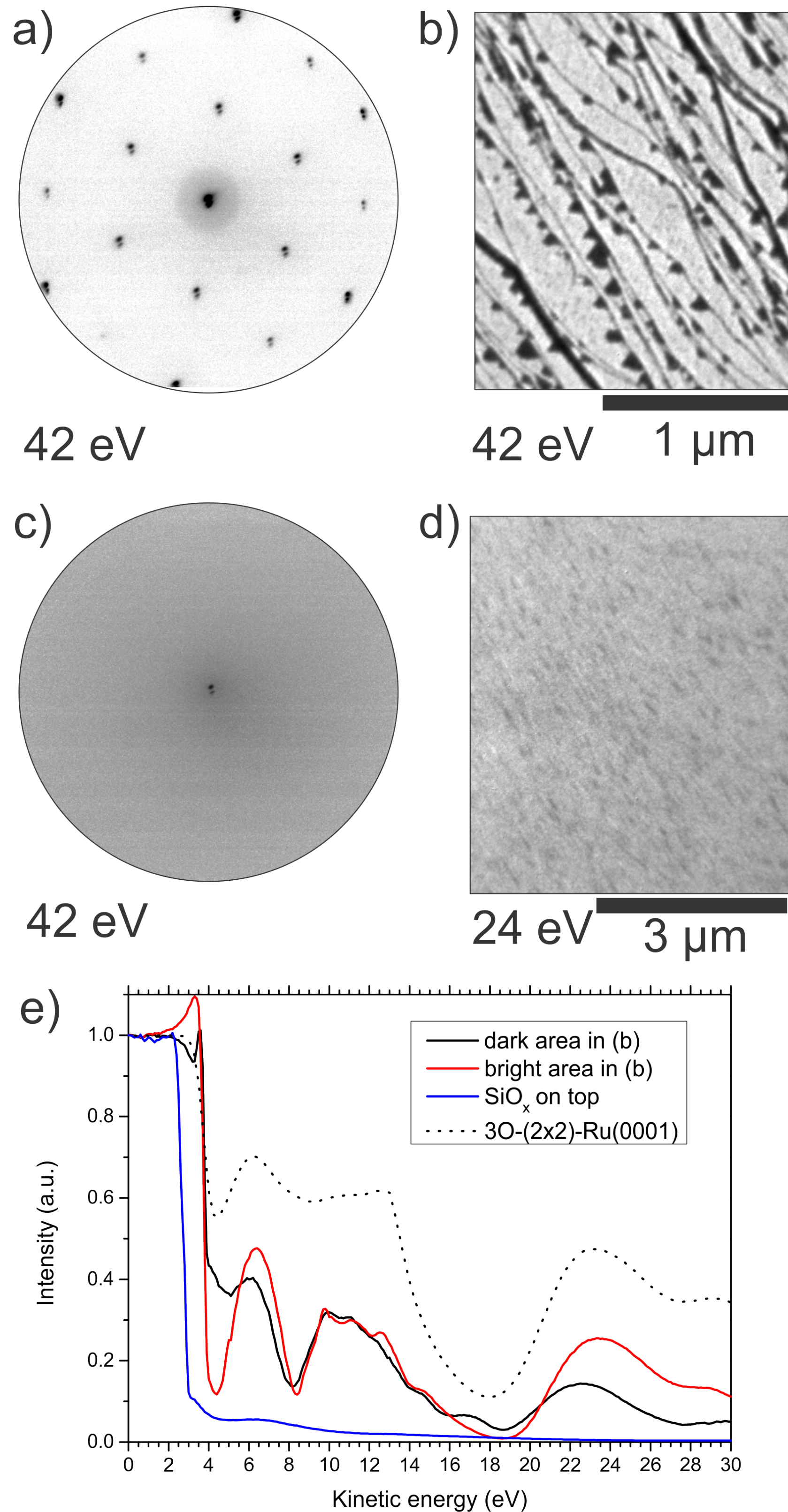

Figure 5.1: a) (2x2) LEED pattern of GeO_2 before silicon deposition b) LEEM image of a partially closed GeO_2 (dark), c) LEED with the 00 beam and d) LEEM after deposition ($p = 2 \cdot 10^{-7}$ mbar O_2 at RT) of the equivalent of 1.9 ML silica on top of 0.1 ML GeO_2. The dark GeO_X domains are visible (different sample position of b), e) LEEM-IV of the different phases of LEEM image b and after the deposition of SiO_X (blue).

In figure 5.2, the evolution of the structure during the annealing in oxygen with a heating rate of 0.8 K/s is presented. The LEED pattern in figure 5.2a shows only the diffuse (00) spot. By annealing to 1060 K a (2x2) LEED pattern is formed (see figure 5.2b). Further annealing leads to a (2x2) structure with an additional ring (see figure 5.2c). The spot intensities of the 00 beam and the (2x2) spots are presented in figure 5.2d. The structure formation starts above 1000 K. The structure formation above 1000 K is well-known for pure silica on Ru(0001) [32] [26], germania forms at 600 K well-ordered structures (see chapter 4). In the present case, the structure formation is dominated by silica.

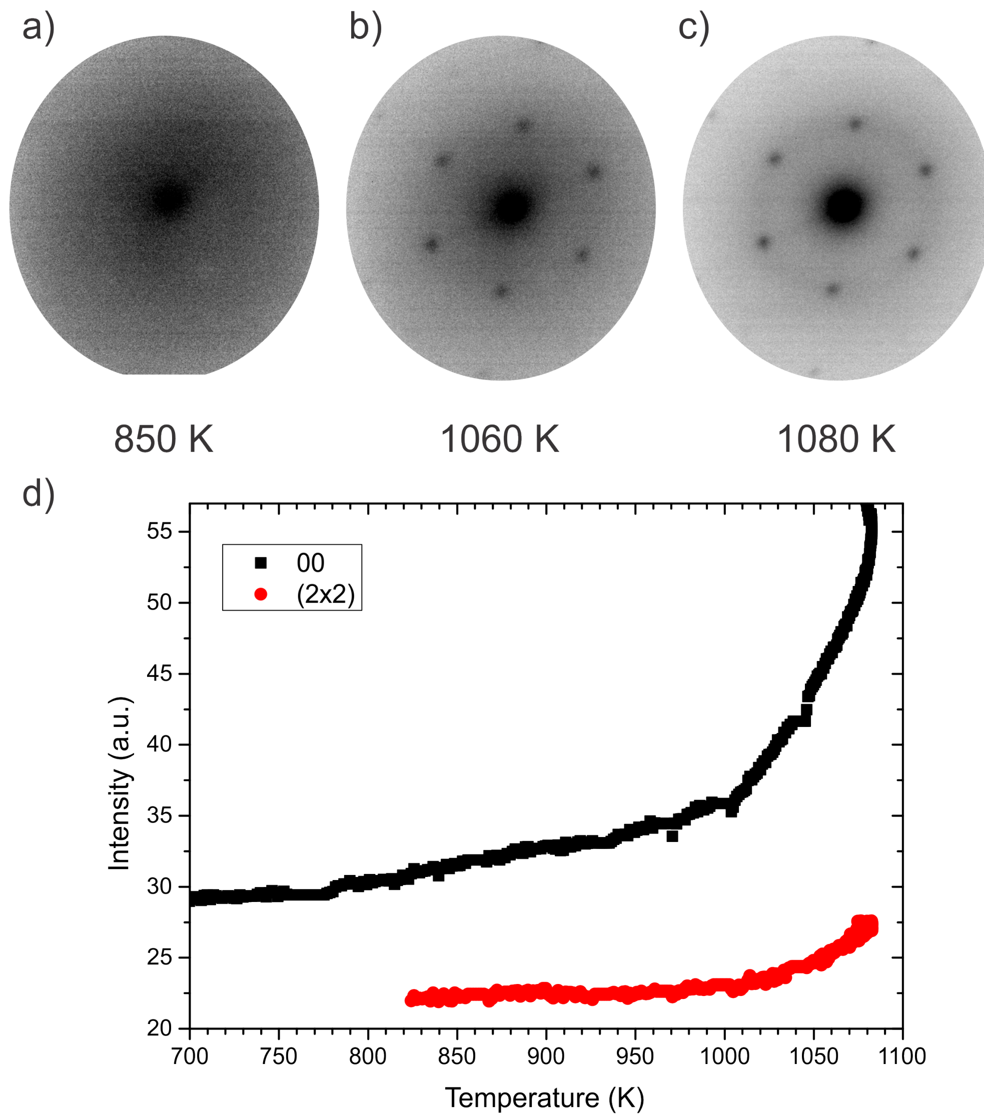

Figure 5.2: Evolution of LEED (42 eV) during annealing SiO_X - GeO_X film in $1 \cdot 10^{-6}$ mbar O_2. a) only the 00 beam, b) (2x2) LEED pattern, c) (2x2) LEED pattern with an additional ring of a vitreous phase, d) LEED spot intensity vs. temperature. The heating rate is 0.8 K/s.

In figure 5.3, the XPS during the preparation of the germania-silica film is presented. In figure 5.3a, the evolution of the Ge3d core level spectra are shown before, after the silicon deposition and after the annealing in oxygen to 1080 K. The Ge3d core level of germania (black) shows a single peak with a binding energy of 31.75 eV. After the deposition of silicon, the Ge3d core level shows that the germania is reduced by the silicon (red peak). The intensity is damped due to the SiO_X cover of the germania. The XPS after the annealing shows that the germanium desorbed and the Ge3d signal vanished completely. The Si2p core level after the deposition on germania shows an incomplete oxidation of the silicon, indicated by the shoulder at lower binding energies. After the annealing in oxygen, the silicon is completely oxidized. In figure 5.3c, the XP spectra of the O1s core level after the deposition of silicon on germania (black) and after the annealing (red) are presented. Due to the oxidation, the O1s core level shifts by 3 eV towards higher binding energies.

The presented photoemission spectra show desorption of germanium during the annealing in oxygen while the used temperature is required for structure formation. However the germanium and silicon do not form connecting bonds and the germanium vanishes. Due to the deposited silicon amount, the germanium desorbed either through the silica film or diffused into the bulk. However, the diffusion of germanium from the ruthenium bulk was never observed, unlike for iron oxide in platinum [7].

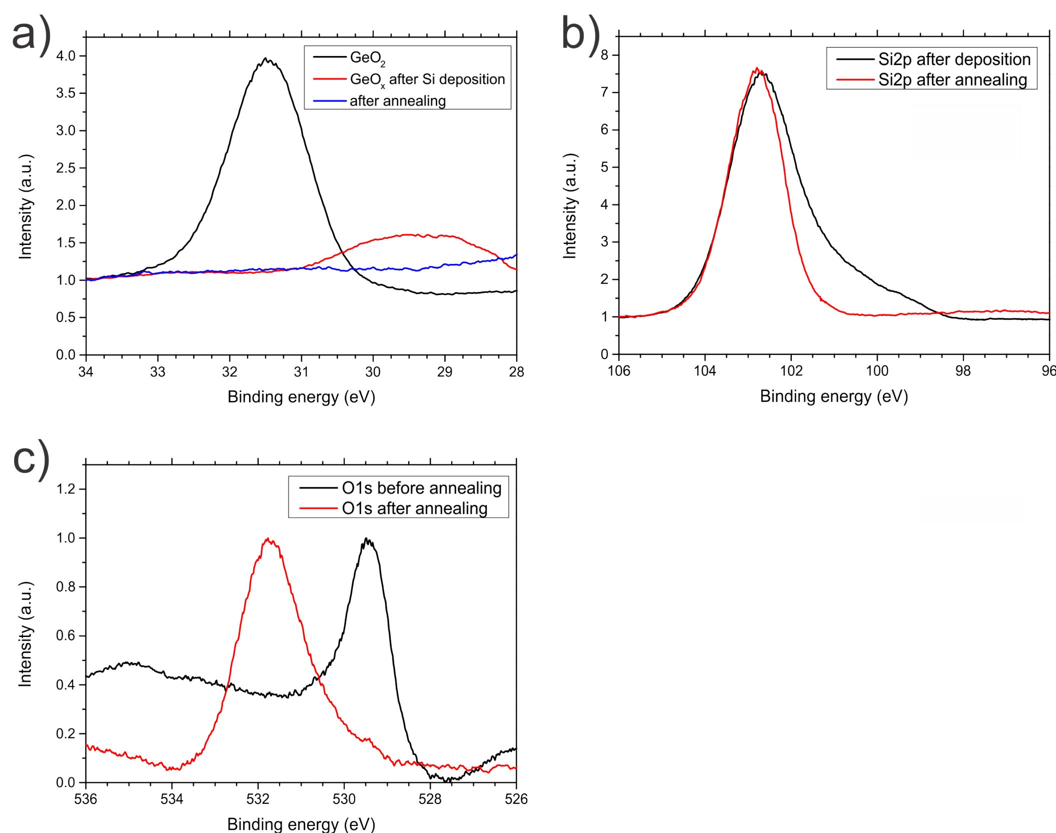

Figure 5.3: Comparison of XPS of germania - silica: a) Ge3d core level of GeO_2 before silicon deposition (black) and SiO_X - GeO_X (red) and Ge3d peak vanished after annealing to 1080 K in oxygen (blue) (hν = 130 eV) b) Si2p core level show partially oxidized silicon of SiO_X - GeO_X after the Si deposition (black) and completely oxidized silicon after annealing (red) (hν = 175 eV), c) O1s core level before the annealing (black) (hν = 600 eV) and after the annealing to 1080 K in oxygen (red).

5.1.2 SiO_X on GeO_X/3O-(2x2)-Ru(0001)

As shown in the previous part, the germanium desorbs during the required annealing at 1080 K for achieving a well-ordered structure. In contrast to the previously described case, in this part the germanium is deposited at RT on a 3O-(2x2)-Ru(0001) surface and directly afterwards the silicon is deposited without annealing before the deposition of silicon. The germania amount is equal to 1 ML and the silica amount is also 1 ML.
XPS were recorded during the preparation procedure and are presented in figure 5.4. Figure 5.4a shows the XPS of the Ge3d core level after the deposition on 3O-(2x2)-Ru(0001) at room temperature. The germanium is partially oxidized. For comparing the intensities of the Ge3d core level at different photon energies, the O2s core level is shown in the spectrum. After the deposition of germanium, the intensity of the Ge3d core level is around two times higher than the intensity of the O2s core level.

After the annealing in oxygen ($1 \cdot 10^{-6}$ mbar) to 1080 K, germanium is present and completely oxidized (see figure 5.4b with hν = 100 eV and 5.4c with hν = 175 eV). At 100 eV photon energy the intensity of the Ge3d is half of the intensity of the O2s core level. In figure 5.4c, the binding energy region is measured with 175 eV photon energy. The higher photon energy leads to a higher kinetic energy of the emitted electrons (around 70 eV for c and around 145 eV for hν = 175 eV) and a larger inelastic mean free path of the emitted electrons [80]. The inelastic mean free path is minimal around electron energies around 70 eV [80]. Therefore the probed depth is minimal at hν = 100 eV (for Ge3d and O2s)and for hν = 175 eV (for Si2p). The probed depth is close to the interface between the germania-silica film and the ruthenium support.

The photoionization cross sections of the probed core levels (Ge3d and O2s) depend on the used photon energies [89]. The photoionization cross section for the Ge3d core level at hν = 100 eV is 7.707 Mbarn and 5.28 Mbarn at hν = 175 eV [89]. The photoionization cross section for the O2s core level changes from 0.54 Mbarn at hν = 100 eV to 0.2338 Mbarn at hν = 175 eV [89]. The photoionization cross section of the Ge3d core level changes by a factor of round 1.5 and the cross section of the O2s core level by a factor of around 2.5. The intensity of the O2s core level decreases from around 9000 a.u. to around 4000 a.u. which correlates to to decrease of the photoionization cross section. The intensity of the Ge3d core level stays constant for both photon energies. The intensity of the Ge3d core level increased referred to intensity of the O2s core level. Due to the increased mean free path and the constant intensity, the germanium can be located underneath the silicon and stays in the bottom layer.

The O2s core level shows two separated peaks which are not detected in figure 5.4a after the deposition of Ge on 3O-(2x2)-Ru(0001). The O2s core level of RuO_2 has a binding energy around 21 eV [143]. The binding energy of the O2s core level in GeO_2 is around 24.1 eV [161] and of SiO_X the binding energy of the O2s core level is around 25.7 eV [162]. The O2s shows the formation of Ru-O bonds and of the Si-O and Ge-O bonds. The intensity ratios indicate that the Ru-O bonds are below the Si-O and Ge-O bonds.

Figure 5.4d shows the evolution of the Si2p core level. During the annealing in oxygen, the core level shifts by 0.4 eV from 101.8 eV to 101.4 eV. The FWHM of the Si2p core level decreased from 2.78 eV to 1.5 eV.

The O1s core levels after the final annealing are presented in figure 5.4e. The O1s was measured with two different photon energies (hν = 600 eV (black) and hν = 780 eV (red)) for increasing the mean free path of the emitted electrons. For the surface sensitive XP spectrum with 600 eV photon energy, the kinetic energy is around 70 eV, respectively 250 eV for 780 eV photon energy.

The more surface sensitive O1s spectrum (hν = 600 eV (black)) shows the main intensity at around 530 eV and a shoulder at around 529 eV. The higher photon energy probes the interface between the film and the ruthenium support. The shoulder is increasing with the higher photon energy, which shows that oxygen component with 529 eV is closer to the ruthenium support. The XPS results of the O1s and O2s are confirming each other and indicate that the germanium stays in the bottom layer of the mixed GeO_2-SiO_2 film on Ru(0001).

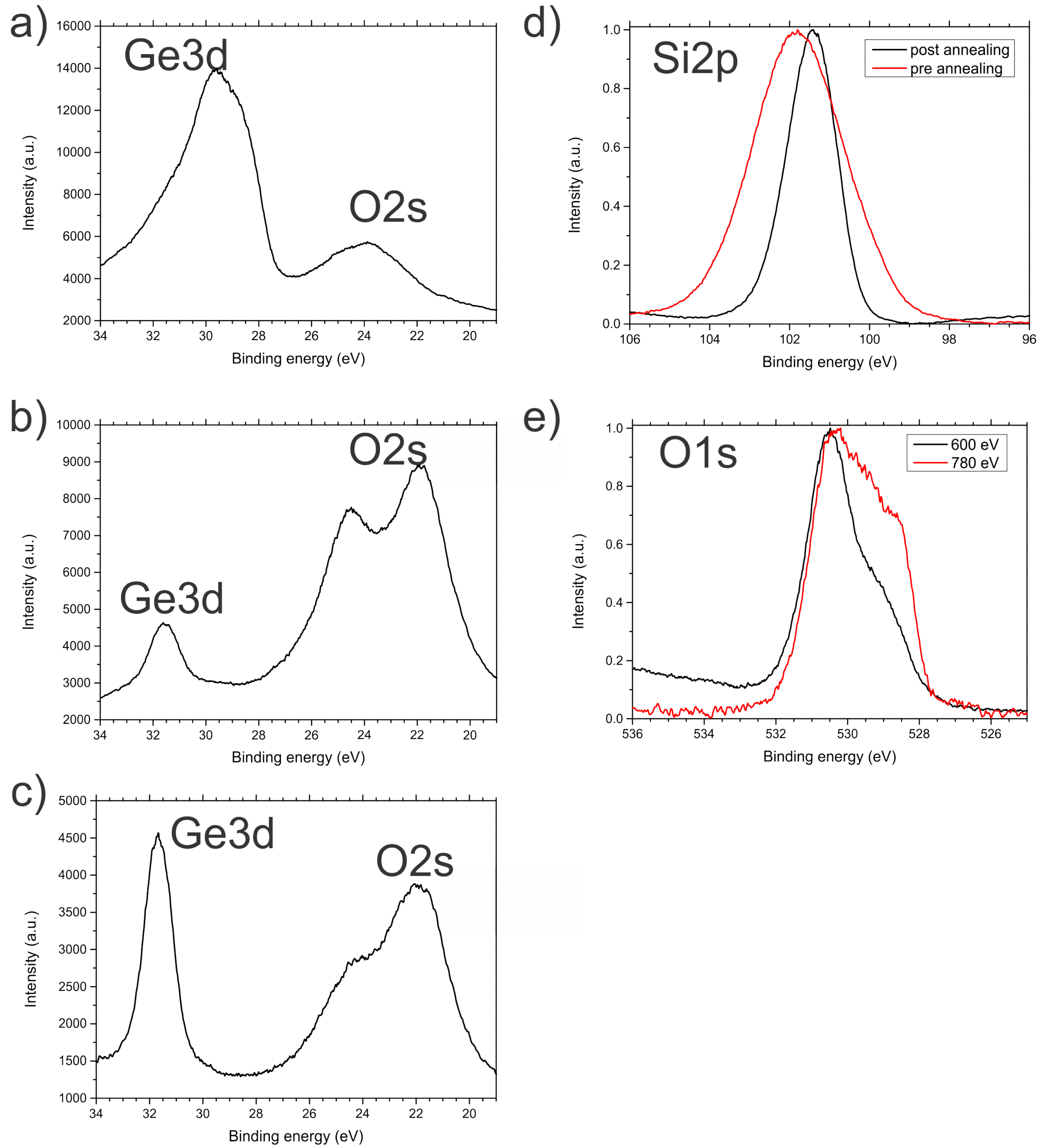

Figure 5.4: XPS study of germania-silica after annealing at 1080 K in $1 \cdot 10^{-6}$ mbar of oxygen a) Ge3d and O2s after deposition of silicon (hv = 100 eV) b) Ge3d and O2s (hν = 100 eV) after annealing, c) Ge3d and O2s (hν = 175 eV) after annealing, d) Si2p pre and post annealed (hν = 175 eV), e) O1s with different photon energies (hν = 600 eV (black line) and 780 eV (red line)) after annealing.

Figure 5.5 displays the structural evolution during the annealing in oxygen. The LEED pattern before the annealing shows only the LEED spots of the Ru(0001) support. At 860 K weak and diffuse LEED spots appear. The LEED spots become sharper at 1000 K and 1065 K. The LEED shows a (2x2) structure with a (2x2)R30° structure. The rotated structure vanished at 1085 K. The final structure shows a (2x2) LEED pattern with low background intensity.

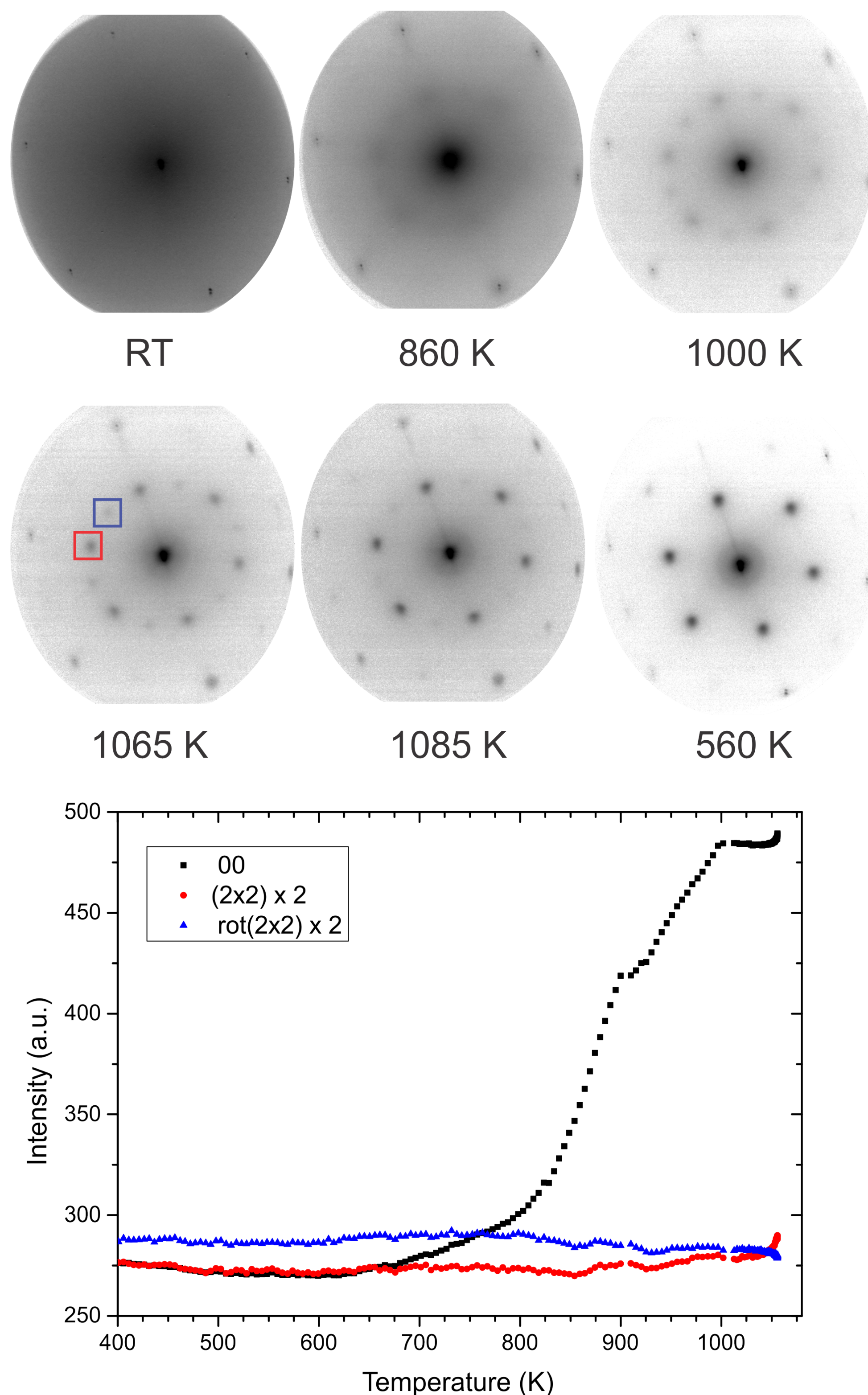

Figure 5.5: Structure formation (LEED at 42 eV) of germania-silica on Ru(0001) during annealing in oxygen ($1 \cdot 10^{-6}$ mbar O_2). At room temperature, only the LEED spots of the substrate are visible. At 860 K a (2x2) and rotated (2x2) phase develops. The spots become more intense at 1000 K and 1065 K. At 1085 K the rotated (2x2) vanishes. During cooling down the (2x2) spots become more intense.

The associated LEEM image (E_{kin}= 5 eV) and LEEM-IV curve of the final (2x2) germania-silica film are shown in figure 5.6. The LEEM-IV curve of the crystalline silica bilayer (red) is displayed additionally as a reference to the germania-silica film (black). The LEEM image shows that the film is homogeneous. Only atomic steps and step bunches of the ruthenium support are clearly visible. The LEEM-IV curve of germania-silica has the MEM-LEEM transition at 3.57 eV, which is 0.18 eV higher compared to the (2x2) silica bilayer. The features of the germania-silica LEEM-IV curve are more prominent compared to the silica LEEM-IV curve. However, the positions of the minima and maxima of the LEEM-IV curve of germania-silica follow mainly the LEEM-IV curve of the crystalline silica bilayer.

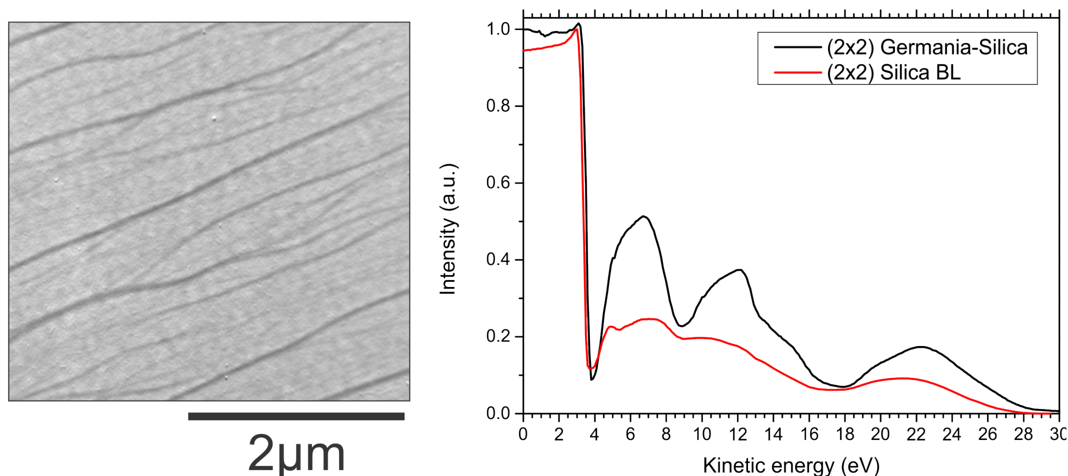

Figure 5.6: LEEM image (E_{kin} = 5 eV) and LEEM-IV comparison of the germania-silica (black) and as a reference the crystalline silica bilayer (red). The MEM-LEEM transition of the germania-silica film is 3.54 eV and silica bilayer has a MEM-LEEM transition of 3.36 eV.

5.1.3 Interpretation

The presented measurements show two different preparation approaches for ultra-thin germania-silica films on Ru(0001). The adding of 1.9 ML silica to a 0.1 ML crystalline (2x2) germania film is unsuccessful and leads to the complete loss of germanium (see figure 5.3). The film loses the (2x2) structure by the deposition of silicon. By annealing in oxygen atmosphere, the film forms also a (2x2) structure at 1060 K and a (2x2) with an additional ring at 1080 K. At these temperatures the structure formation of silica on Ru(0001) can be observed [26] [32]. The structure formation is dominated by the silica. The germanium can be lost by desorption after diffusion through the amorphous SiO_X. The formation of germanium nanocrystals into a silica matrix is reported in [163] [164]. However, the formation of germanium nanocrystals has never been observed for the ultra-thin germania-silica films on Ru(0001).

One successful approach is a combined approach: the deposition of germanium on 3O-(2x2)-Ru(0001), subsequent deposition of silicon and finally the annealing in oxygen atmosphere. The GeO_X forms a weak and blurry (2x2) LEED pattern on 3O-(2x2)-Ru(0001) (see chapter 3). After the deposition of germanium and silicon, the germanium is partially oxidized (see figure 5.4a). The oxidation at 1080 K leads to completely oxidized germanium. The comparison of the LEED spot intensities vs. temperature of both preparation approaches (see figures 5.2 and 5.5) show that the intensity of the 00 beam of the successful approach increases at around 700 K in contrast to around 1000 K for the unsuccessful approach.

The presence of germanium after annealing temperatures above 1000 K indicates the formation Ge-O-Si bonds, which lead to a thermal stabilization of the germanium. The O1s core level shows a shoulder at 529 eV binding energy that grows in intensity with the increase of the mean free path of the photoelectrons (see figure 5.4e). This binding energy can be related to O-Ru [146] [32]. That shows that the oxygen component is located at the bottom of the germania-silica film and at the interface to the ruthenium. With the increasing Ge3d core level intensity with increasing mean free path of the photoelectrons compared to the O2s core level, it can be concluded that the germanium is located at the bottom layer in the mixed germania-silica film (see figure 5.4b and 5.4c). From the XPS the presence of germanium at the surface cannot be excluded. However, the majority of the germanium is located at the bottom layer of the film. The evolution of the LEED pattern in figure 5.5 shows the presence of a (2x2) and a rotated (2x2) phase at 1060 K. The germania-silica film is homogeneous within the resolution limits of the SMART microscope (see figure 5.6).

The initial crystallinity of the first deposited film has a huge influence on the final film. Disordered partially oxidized GeO_X or SiO_X films have the ability to form new bonds with the other oxides during the complete oxidation. The structure formation temperature of germania-silica is decreased by around 300 K compared to pure silica. This indicates that germania acts as nuclei for the crystallization. The GeO_4 tetrahedral building units might be formed at lower temperatures compared to the SiO_4 tetrahedral building units. That would be a reasonable explanation. The formation of crystalline silicates at low temperatures is well-known for ion silicates [165] [48].

5.2 Silica with germania on top

In this part ultra-thin germania-silica films are prepared with the inverted deposition sequence as discussed in the previous part. The deposition and calibration of silica proceeds similar to the well-known and studied preparation conditions of silica on Ru(0001) [26]. The deposited silicon amount corresponds to 1.5 ML silica and the germania amount is equal to 0.5 ML. The ratio between silica and germania is chosen to 3:1 or $Si_{0.75}\,Ge_{0.25}\,O_2$. In this part, three different preparations will be presented with similar germania to silica ratio and comparable annealing temperatures:

- A: In a first step, the silicon is deposited in $2 \cdot 10^{-7}$ mbar oxygen atmosphere and the partially oxidized, disordered silicon is annealed in $1 \cdot 10^{-6}$ mbar O_2 to 1040 K. At 1040 K, the silica forms a crystalline six member honeycomb structure with a (2x2) LEED pattern [26] [37]. After cooling down the sample in oxygen, the germanium, corresponding to 0.5 ML germania, is deposited in $2 \cdot 10^{-7}$ mbar oxygen atmosphere at RT. For oxidizing and ordering the germanium the sample is annealed at 720 K for 10 min in $1 \cdot 10^{-6}$ mbar O_2. A proof of the thermal stability is done by further annealing to 970 K in oxygen atmosphere.

- B: A second variant is the silicon deposition in $2 \cdot 10^{-7}$ mbar oxygen atmosphere at room temperature on 3O-(2x2)-Ru(0001) (similar to the silica preparation [26]), the germanium was deposited at 570 K in $2 \cdot 10^{-7}$ mbar O_2 on top of the disordered SiO_X. Afterwards the sample was annealed at 720 K for 10 min and at 970 K in in $1 \cdot 10^{-6}$ mbar O_2. The second annealing step leads to a direct comparison to the preparation variant A.

- C: The third variant is the deposition of germanium on disordered SiO_X in $2 \cdot 10^{-7}$ mbar O_2 at room temperature, annealing afterwards to 820 K for 50 min in $1 \cdot 10^{-6}$ mbar O_2. The relatively long annealing time is required to form a (2x2) LEED pattern.

5.2.1 Preparation "A" and "B"

First, the chemical composition of the germania-silica films of the preparation methods "A" and "B" are compared in figure 5.7 and 5.8. In figure 5.7, the XP spectra for germania-silica are shown for the preparation "A", germania deposition on crystalline (2x2) silica.

After annealing to 720 K, the XPS of the Ge3d core level shows that the germanium is fully oxidized. The binding energy of the Ge3d core level is 31.8 eV. The silicon is also fully oxidized and a shoulder at lower binding energies of lower silicon oxidation states is missing. The O1s core level shows a broad peak which can be described by three components related to (a) the Si-O bond (531.3 eV), (b) Ge-O (530.2 eV) and to (b) the Ru-O bond (529.2 eV). A component related to Si-O-Ge is missing.

Further annealing to 970 K shows that the germanium signal completely disappears, meaning that the germanium desorbed. The solution of germanium into ruthenium bulk at room temperature is negligible [166], therefore the diffusion of germanium into the ruthenium bulk is very unlikely. The diffusion of germanium to the ruthenium surface was never observed during the experiments for this study. The Si2p line does not show any changes between the two annealing temperatures. The O1s line shows a decrease of the component with a binding energy at 530 eV. This decrease can be correlated to the loss of germanium. The XPS shows clearly that first adding and afterwards annealing in oxygen atmosphere of germanium on crystalline silica does not lead to a mixed germania-silica film. Instead, germanium and silicon form separated oxides. Once completely formed, the chemical stability of crystalline silica inhibits the subsequent formation of chemical bonds with germanium.

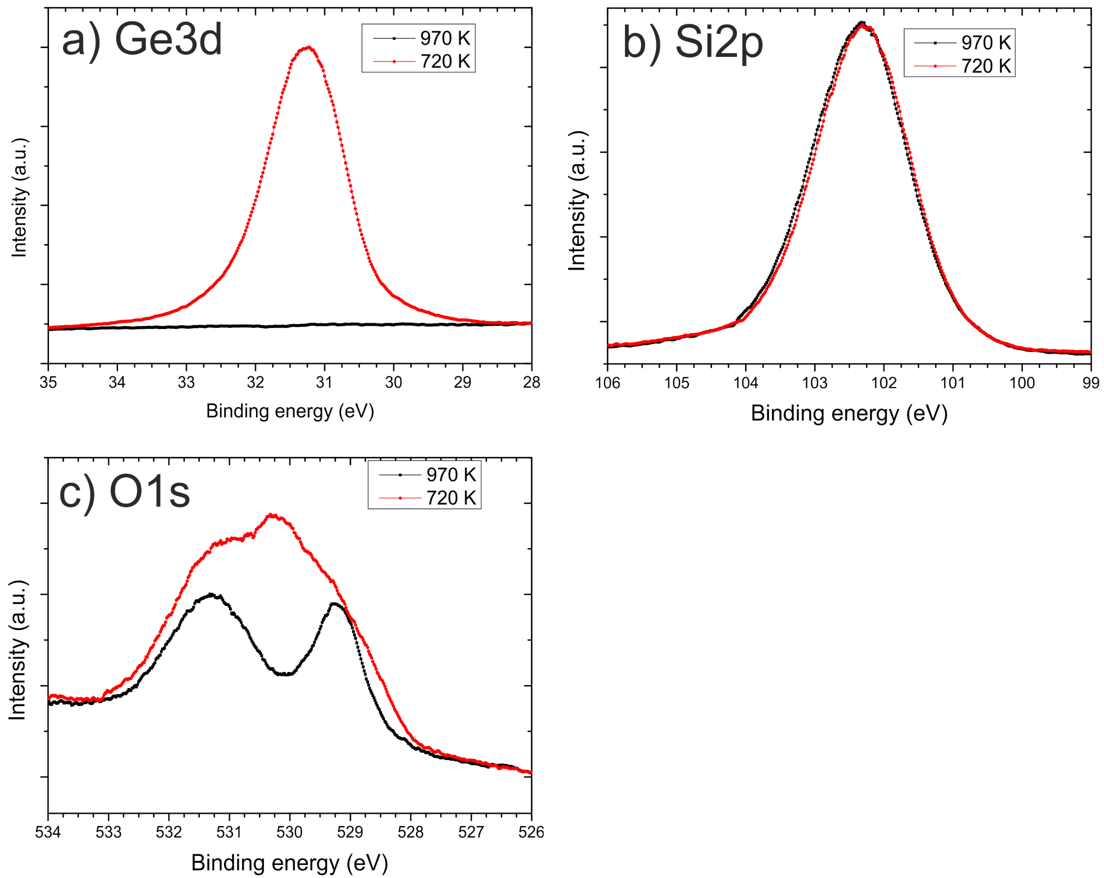

Figure 5.7: XPS results (preparation "A") of 1.5 ML crystalline silica with 0.5 ML germania after annealing in $1 \cdot 10^{-6}$ mbar O_2 to 720 K (red) and 970 K (black). a) Ge3d (hν = 100 eV) shows completely oxidized germanium at 720 K and germania desorption after annealing at 970 K; b) Si2p (hν = 175 eV) proofs completely oxidized silicon at 720 K, which does not change after the final annealing step; c) O1s (hν = 600 eV) oxygen component of Ge-O vanishes after annealing to 970 K

The preparation "B", germania-silica film with an initially disordered silica films, is presented in figure 5.8. To compare the influence of the crystallinity of the initial silica layer, the amounts and annealing temperatures are similar to the preparation "A". Figure 5.8a shows that germania is present after the annealing at 970 K, but the germanium Ge3d signal decreased by about a factor of two compared to the 720 K annealing. The germanium is completely oxidized. The comparison of the Ge3d core level spectrum of figure 5.8a with the one of figure 5.7a shows that both are similar after the first annealing at 720 K. The decrease of the signal intensity is either related to the desorption of non-connected germania to silica or to damping due to germania located at the interface to the support.

The Si2p core level shows minor differences between the two annealing steps (see figure 5.7b). After the annealing to 720 K, the Si2p core level is minimally broader than after the annealing to 970 K. The binding energy is constant and the silicon is completely oxidized. That indicates that the formation of Ge-O-Si bonds happens at 720 K. The silicon related chemical bonds are not affected to higher annealing temperatures. The comparison of the binding energies of the Si2p line for both preparation recipes "A" and "B" show that the binding energies for the crystalline silica (preparation "A") is 102.2 eV (see figure 5.7b) and for the preparation B with initially disordered silica is 101.2 eV (see figure 5.8b). That can be related to chemical shift due to presence of linking Si-O-Ge bonds. For the silica bilayer a Si2p binding energy of 102.5 eV is observed [32].

In figure 5.8c, the XPS of the O1s shows a similar line shape for both annealing temperatures. Increasing the annealing temperature by 250 K leads to a shift of the O1s core level to higher binding energy by 0.2 eV. The O1s peak intensity at the shoulder at 529 eV is increasing after the second annealing. This can be related to the formation of Ru-O bonds [146]. The comparison of the O1s line shows different line shapes for the preparation "A" (see figure 5.7c) and "B" (see figure 5.8c). This can be understood by different oxygen bonds for the different preparations.

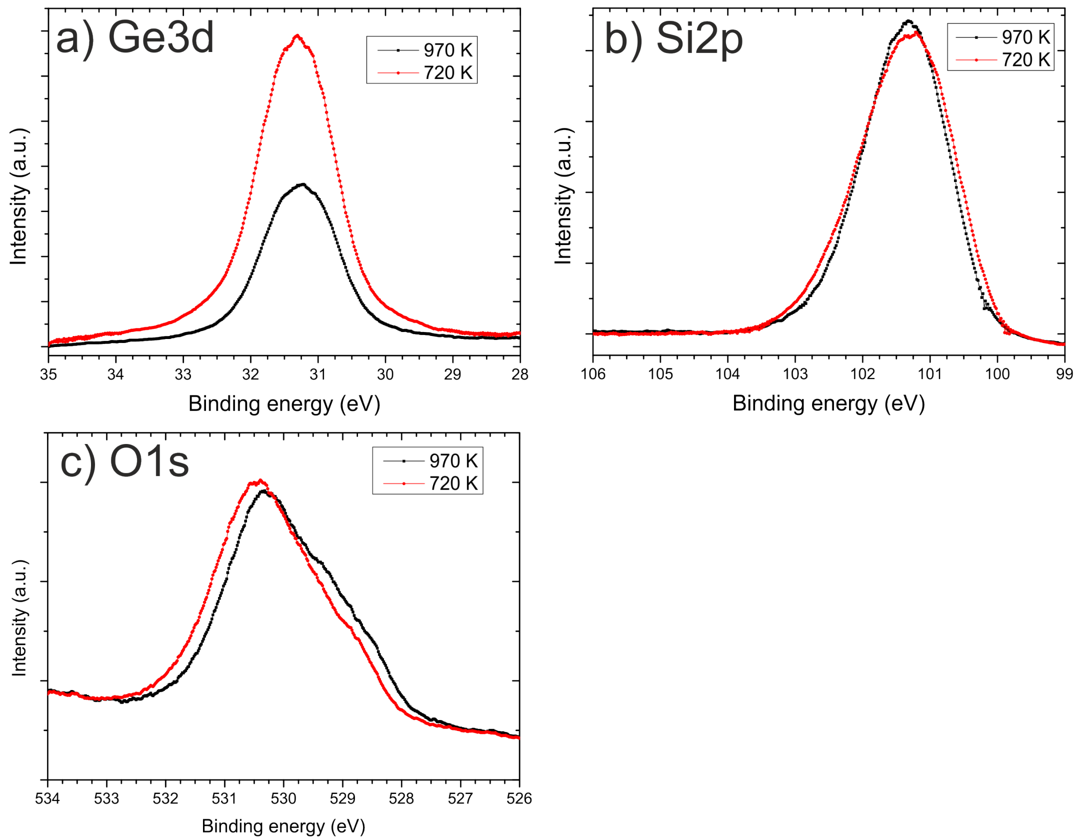

Figure 5.8: XPS (preparation "B") of 1.5 ML disordered silica with 0.5 ML germania after annealing in $1 \cdot 10^{-6}$ mbar O_2 to 720 K (red) and 970 K (black). a) Completely oxidized germanium at 720 K and at 970 K (hν = 100 eV); b) completely oxidized silicon (Si2p: hν = 175 eV); c) oxygen core level shifts by 0.2 eV after the annealing to 970 K (O1s: hν = 600 eV)

The evolution of the Ge3d, Si2p and O1s core levels during preparation "B" with different photon energies is presented in figure 5.9 for probing the core levels with different inelastic mean free path. The Ge3d is summarized in figure 5.9a at the different preparation steps. The used photon energies are 100 eV and 175 eV, which lead to kinetic energies of around 70 and 140 eV. At 100 eV the Ge3d core levels during the preparation show a binding energy of 31.4 eV. The binding energy is increased at 175 eV by around 0.3 eV, except for the annealing step at 720 K.

The evolution of the Si2p core level is presented in figure 5.9b, measured with 70 and 260 eV kinetic energy. The binding energies shift down with higher annealing temperatures. The binding energy is 102 eV after the deposition. The binding energy shifts to 101.5 eV after the annealing to 970 K. This can be seen for both photon energies, 175 eV and 360 eV. The germania and silica are completely oxidized after the deposition.

The XP spectrum of the O1s core level (see figure 5.9c) during the preparation shows that the component at around 529 eV increases with increasing annealing temperature and photon energy. The surface sensitive component has a binding energy of 530.5 eV. At around 240 eV kinetic energy (hν = 780 eV), the oxygen components show a lower binding energy compared to the surface sensitive measurements, also a component at 528 eV becomes more prominent. The second annealing leads to a shift of the binding energy towards lower binding energies.

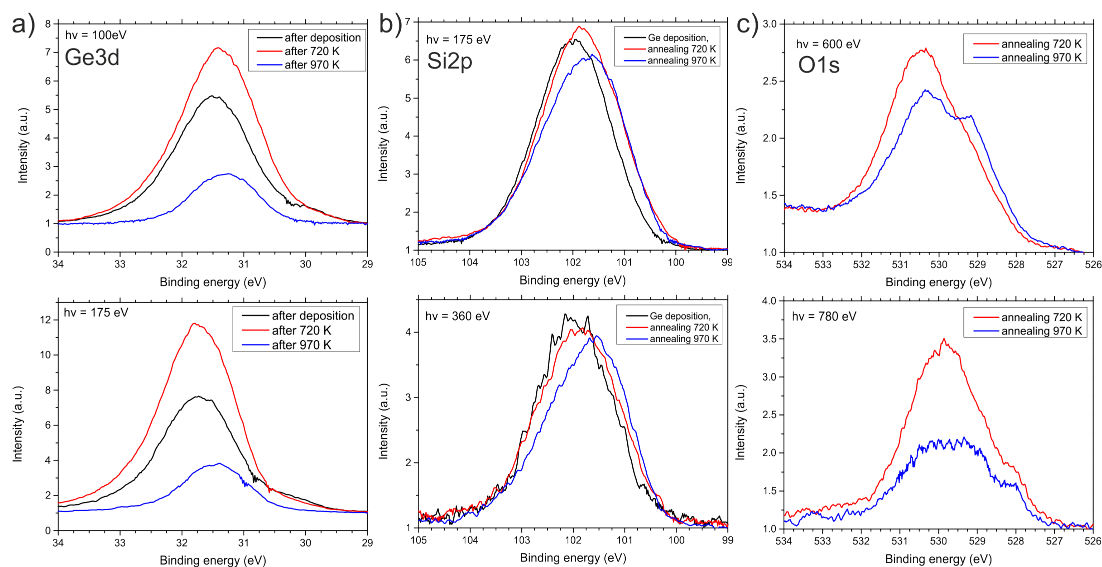

Figure 5.9: XPS depth profile during the preparation "B" of germania-silica: a) Ge3d b) Si2p and c) O1s. Annealing temperature and the used photon energies are given in the insets. The approximate kinetic energies are in (a) 70 and 140 eV, in (b) 70 and 260 eV and in (c) 70 and 240 eV for the more surface (top row) and more bulk (bottom row) sensitive spectra, respectively.

Figure 5.10 compares the LEED patterns for the two preparation variants “A” (top row) and “B” (bottom row) at different annealing steps. All preparations lead to a (2x2) LEED pattern. In figure 5.10a, the LEED pattern of a (2x2) silica plus the germania is shown. The LEED pattern of figure 5.10b shows the films after the annealing to 970 K, when the XPS showed the complete desorption of germanium.

The SPA-LEED shows that the desorption of germanium influences the silica (preparation “A”), the LEED spots become sharper compared to germania-silica films (preparation “B”) on Ru(0001). The comparison of the LEED pattern shows that the (2x2) LEED spots after germanium desorption are sharper (see figure 5.10b) compared to the LEED pattern in figure 5.10d.

The annealing to 970 K leads to a better order of the films than the annealing to 720 K (for preparation “B”). However the LEED pattern for preparation “B” shows less sharp LEED spots compared to the separated germania and silica. The required temperatures for well-ordered crystalline germania-silica films on Ru(0001) are 300 K lower than for pure silica films on Ru(0001) [32]. The ultra-thin germanium oxidizes and orders around 600 K on Ru(0001) (see chapter 4). The silica might arrange and crystallize at the ordered germania structure and the germania act as a nucleus for the crystallization of the silica.

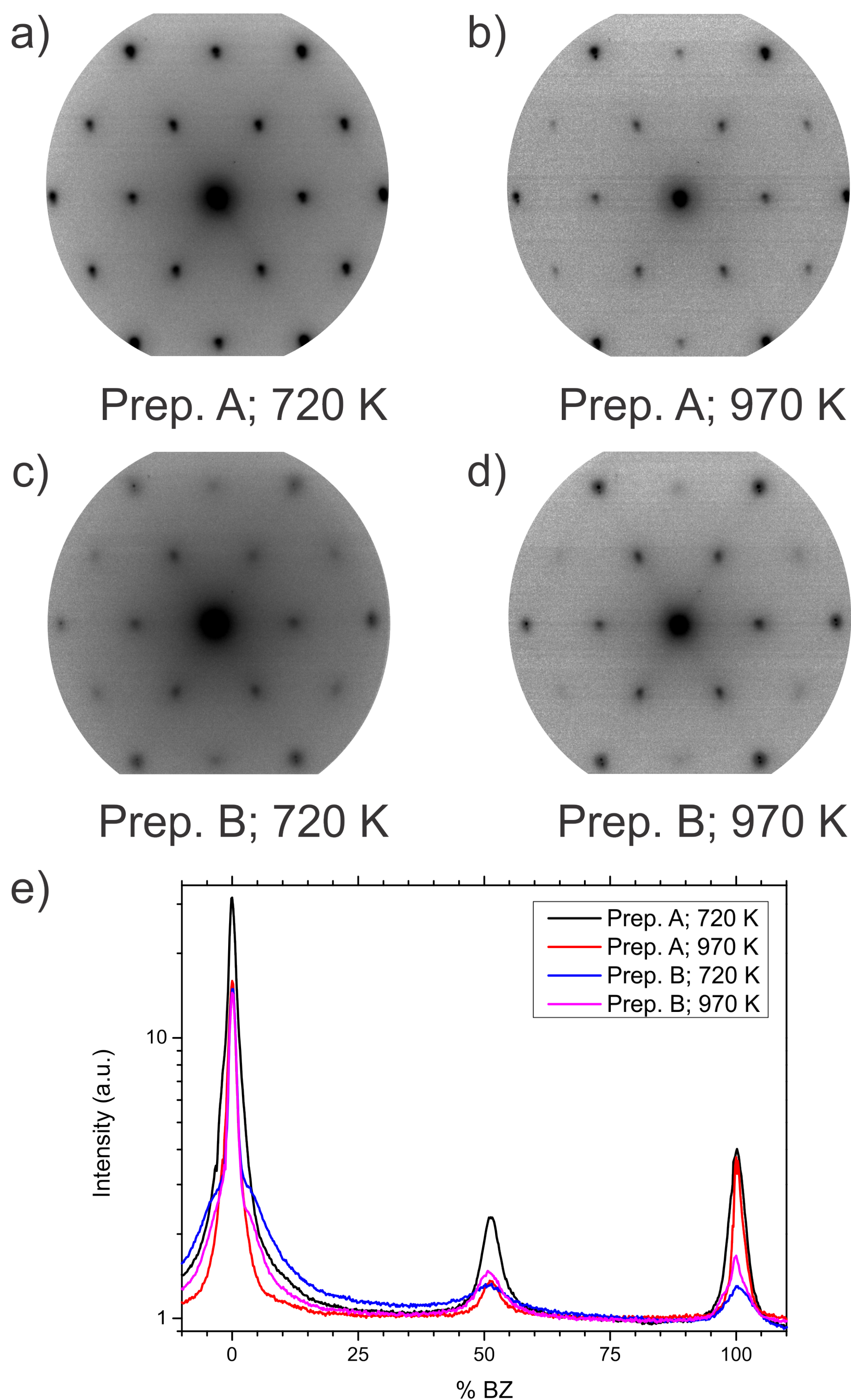

Figure 5.10: Comparison of (2x2) LEED pattern (E_{kin} = 42 eV) of different germania - silica preparations and annealing temperatures: a) preparation "A" with germanium deposition at RT on crystalline silica after annealing at 720 K, b) preparation A after annealing at 970 K, c) preparation "B" with germanium deposition at 570 K on non-crystalline silica after annealing to 720 K and d) preparation B after annealing to 970 K, e) SPA-LEED of the different LEED pattern

In figure 5.11, the LEEM-IV measurements of the different preparations steps are compared. All LEEM-IV curves show a very similar MEM-LEEM transition of 3.49 eV except for the LEEM-IV curve of the 720 K, non cryst. (preparation "B") with 3.45 eV and similarities at 8 eV, around 16 - 18 eV and an increasing reflectivity at 19 eV. The reflectivity at 19 eV and higher is dominated by the Ru(0001) support. The comparison of the LEEM-IV curves of the germania-silica shows that the annealing to 720 K lead to a „flat“ curve between 3.5 eV and 7 eV. After the annealing to 970 K the LEEM-IV curves show two maxima at 6 and around 12 eV. The LEEM-IV measurements show also similarities to the LEEM-IV measurements of pure silica [26], the influence of germanium on the curves is weak. Therefore the use of LEEM-IV fingerprints for the characterization of germania-silica films on Ru(0001) without chemical information is not feasible. The strong similarities of the LEEM-IV curves show that the structures of silica and germania - silica are very similar. That indicates that silicon can be substituted by germanium. However, germanium is not incorporated into an existing ultra-thin crystalline silica matrix. The incorporation of germania happens only in the initial formation of the silica network.

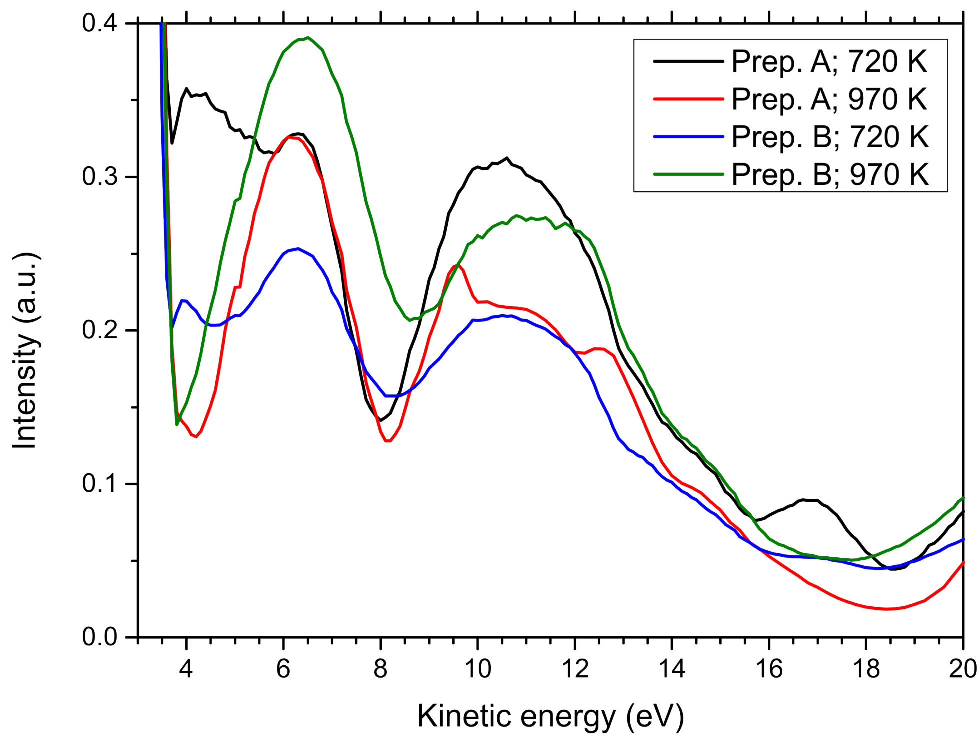

Figure 5.11: LEEM-IV comparison of different germania-silica preparations and annealing temperatures. Black curve: germania-silica on (2x2)-silica and annealed to 720 K; red curve: after desorption of germania after germania-silica annealing to 970 K; blue curve: germania-silica on disordered silica and annealed to 720 K; green curve: germania-silica on disordered silica and annealed to 970 K

5.2.2 Preparation "C"

The third variant is the preparation "C". The ratio between deposited germanium and silicon is similar to the previously presented germania-silica film with 1.5 ML silica and 0.5 ML germania. The germanium is deposited at room temperature on disordered SiO_X in $2 \cdot 10^{-7}$ mbar O_2. Afterwards, the germania-silica film is annealed to 820 K in $1 \cdot 10^{-6}$ mbar O_2 for 50 min. Figure 5.12 summarizes the XPS, LEED and LEEM-IV measurement of the resulting germania-silica film. The XPS of the Ge3d core level in figure 5.12a shows that the germanium is completely oxidized. The Ge3d core level has a slight shoulder at around 31.5 eV binding energy. The two components might be related to GeO_4 tetrahedral building units that are connected to SiO_4 tetrahedral building unit and one that are connected to GeO_4 tetraeders.

The O1s core level spectrum is shown in figure 5.12b. The O1s core level has a binding energy of around 531 eV and the core level shows an oxygen component with a binding energy of 529 eV. This core level can be related to O-Ru bonds, as observed, or pure silica, if interfacial oxygen is present. The XP spectrum of the Si2p core level is presented in figure 5.12c. The Si2p core level has a binding energy of 102.5 eV and has a FWHM of around 2.2 eV. The silicon is completely oxidized.

Figure 5.12d presents the LEEM-IV curve of the germania-silica film compared to the crystalline silica bilayer. The LEEM-IV curve of germania-silica is very similar to the crystalline silica bilayer and has a overall lower reflectivity. The LEEM-IV curve is dominated by the silica structure. This can also be observed for the crystalline-vitreous silica bilayer, here the LEEM-IV curve is similar to the vitreous one. The germania-silica film is crystalline and shows a (2x2) LEED pattern (see figure 5.12e). A representative LEEM image is presented in figure 5.12f. The LEEM image shows a homogeneous germania-silica film with 50 nm to 100 nm large brighter areas compared to the surrounding. The atomic steps and step bunches of the ruthenium support are visible.

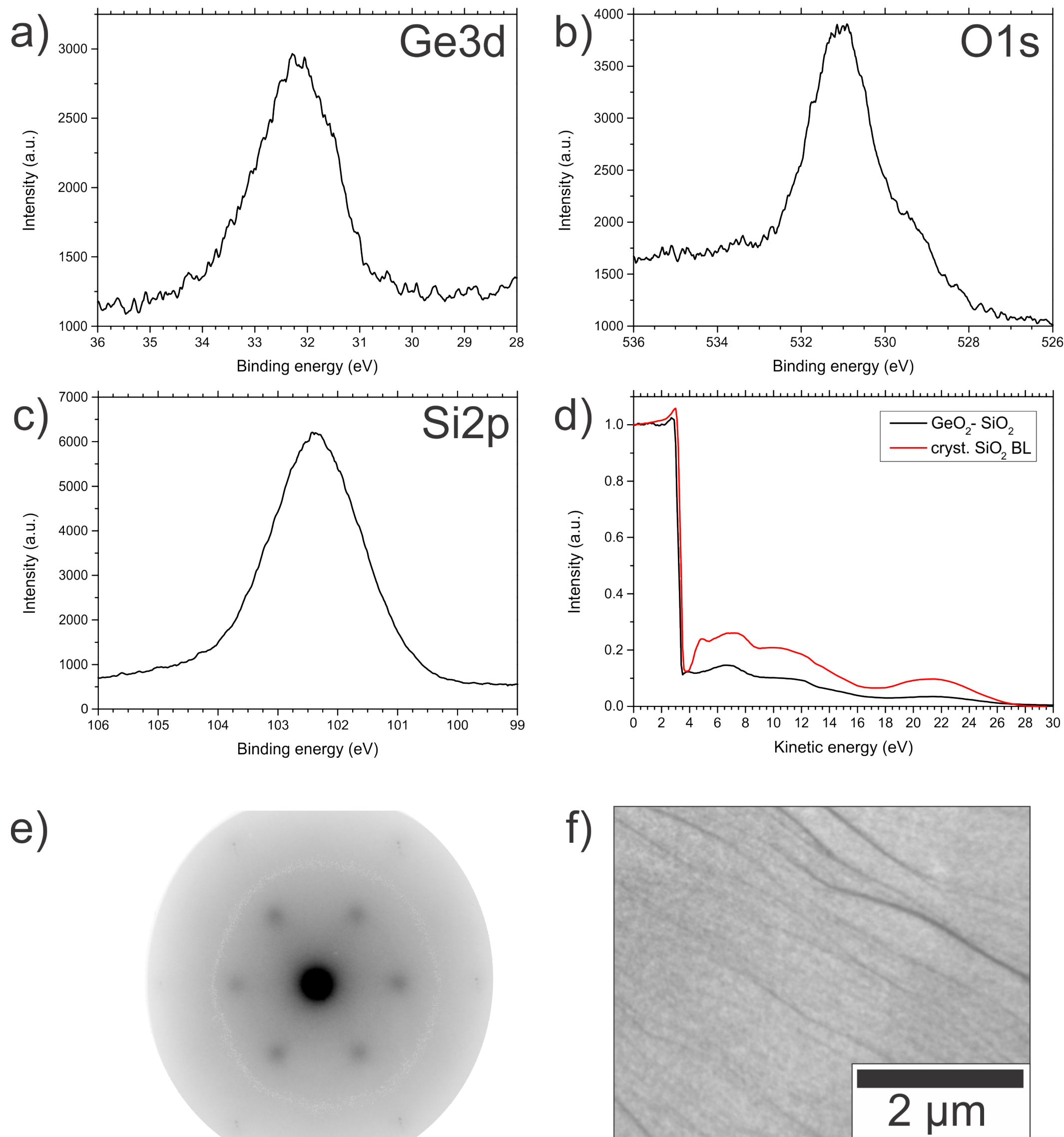

Figure 5.12: Preparation "C" of germania-silica on Ru(0001): XPS a) Ge3d core level (hν = 100 eV) with completely oxidized germanium b) Si2p core level (hν = 175 eV) and c) O1s core level (hν = 600 eV) shows oxygen with a binding energy of 529 eV. d) LEEM-IV measurements of GeO_2-SiO_2 and SiO_2 BL, e) (2x2) LEED pattern GeO_2-SiO_2 (42 eV), f) homogeneous LEEM with steps of the Ru(0001) support (42 eV)

5.2.3 Low temperature crystallization of germania-silica at 820 K

The different preparations of ultra-thin germania-silica films show that the films crystallize at temperatures around 720 K. This is around 330 K lower than the structure formation for the pure silica bilayer which crystallizes around 1050 K [26]. However the crystallization of silica was not studied at lower temperatures. Therefore, a comprehensive study of the crystallization of ultra-thin germania-silica and silica films on Ru(0001) is presented in figure 5.13. Figure 5.13 compares the LEED pattern of germania-silica (top row) and silica (bottom row) during the annealing in oxygen ($1 \cdot 10^{-6}$ mbar). The formation of a LEED pattern for preparation "C" is slower compared to preparation "B", 10 min at 720 K (preparation "B") compared to 50 min at 820 K (preparation "C"). The LEED pattern of a (2x2) germania-silica film is shown in figure 5.13a at 820 K after annealing for 50 min in $1 \cdot 10^{-6}$ mbar O_2. At room temperature the LEED pattern becomes more intense due to the Debye-Waller effect (see figure 5.13b). For comparison a similar annealing was performed for pure bilayer silica. The silica bilayer forms no structure after annealing at 820 K after 50 min annealing (not shown), but exhibit a diffuse LEED pattern after further annealing at 920 K for 50 min (see figure 5.13c). The silica bilayer forms immediately a (2x2) LEED pattern at 1090 K (see figure 5.13d).

The structure formation of germania-silica at 820 K is related to the presence of germanium. Germanium oxidizes at temperatures around 600 K and forms GeO_4 tetrahedral building units (see chapter 4). This initial GeO_4 structures are likely the nuclei for the formation of the germania-silica structure. In contrast to the described low temperature crystallization of germania-silica, the crystallization temperatures for germania-silica are around 1080 K for the case showed in the first part of this chapter. Obviously, the deposition order, germanium amount and initial order influence the crystallization. The low temperature crystallization of silica containing films is also known for iron-silicates [165] [48].

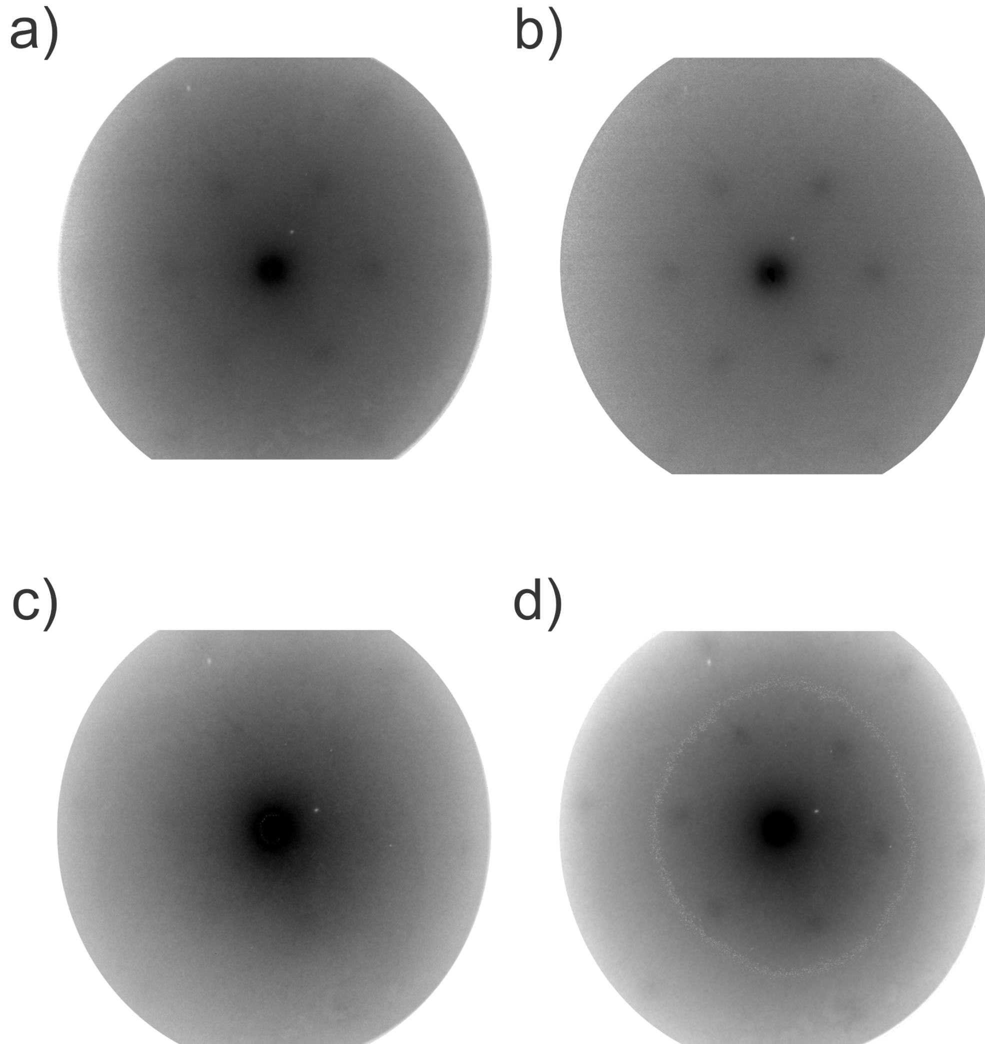

Figure 5.13: Comparison of LEED pattern (all at 42 eV) of germania-silica and silica a) (2x2) LEED germania-silica after 50 min annealing at 820 K (preparation "C"), b) Germania-silica LEED pattern at RT, c) silica bilayer after annealing at 920 K for 50 min, d) formation of a (2x2) LEED pattern of a silica bilayer after annealing at 1090 K for 1 min.

5.2.4 Interpretation

The the preparations "B" and "C" lead to the formation of well-ordered ultra-thin germania-silica films on Ru(0001) with the opposite deposition sequence as presented in the previous part. The used silica to germania ratio (1.5 ML silica and 0.5 ML germania) is similar for all three presented preparations. The XPS data in figure 5.8 (preparation "B") show that the germania-silica film can be successfully prepared by germanium deposition at 570 K in oxygen atmosphere on disordered SiO_X in contrast to the preparation "A" with germanium deposition on crystalline (2x2) SiO_2 (see figure 5.7).

The preparation "A" showed that the annealing to 970 K leads to the desorption of germanium. From this fact, one might conclude that for preparation "A", germania and silica are coexisting as two separated oxides; chemical bonds between SiO_4 and GeO_4 tetrahedral building units are not formed. This is shown by the constant Si2p core level by the desorption of the germania (see figure 5.7) and the mission Ge-O component of the O1s core level.

The initial crystallinity of the silica has the significant influence on formation of a mixed germania-silica oxide. The crystalline silica matrix is chemically inert and the integration of germanium is not possible within the used preparation parameters. On the contrary, for the preparations "B" and "C" with disordered SiO_X, it is possible to integrate germanium atoms into the silica matrix during the oxidation and structure formation which lead to the formation of mixed ultra-thin germania-silica films on Ru(0001).

However, figure 5.8 shows a less intense Ge3d signal. A possible explanation for the partial desorption of the germania is that the desorbed germania was on top of a bilayer domain which is chemically inert. The separated germania islands are not stable at 920 K and therefore germania desorbs. Another possibility is that the germania is partially located at the interface which leads to a damping of the surface sensitive signal.

Figure 5.9 summarizes the XPS during the preparation "B", measured with different photon energies. The Ge3d core level shows a shift towards lower binding energies with increasing mean free path of the photoelectrons. The Si2p core level during the preparation "B" shows an increasing Si2p component at lower binding energies in the surface sensitive measurements for the different annealing steps. The trend towards lower binding energies is smaller for the higher mean free path of the photoelectrons. The Si2p core level and the Ge3d core level show lower binding energies for large probing depth and for higher annealing temperatures.

The O1s core level shows that with increasing oxidation temperature and photon energy the oxygen components at lower binding energies increase. The increasing of the oxygen component at 529 eV can be observed after the first oxidation step to 720 K with 780 eV photon energy. The component becomes more prominent after the second annealing to 970 K and can be observed with 600 eV photon energy. This indicates the formation of Ru-O bonds during the first oxidation and the increasing of Ru-O with the further oxidation which indicates the formation and presence of interfacial oxygen. In addition, an oxygen component at 528 eV can be observed for high-probing depths. This oxygen component might be related to a slight contamination of the ruthenium bulk.

The preparation “C” leads to homogeneous crystalline germania-silica films (see figure 5.12). The germanium and silicon are completely oxidized. The O1s core level shows a narrow peak width compared to preparation “B”. The O1s core level spectrum of preparation “C” (see figure 5.12) is comparable to the O1s spectrum in figure 5.4e. In preparation “C”, the structure formation of the germania-silica film requires around 50 min annealing at 820 K in oxygen atmosphere in contrast to 10 min in preparation “B”. This shows that the germanium deposition at 570 K, leads to an enhanced chemical reaction of the SiO_X with germanium.
The comparable annealing of a pure silica bilayer and a germania-silica film is presented in figure 5.13 and shows that the pure silica requires around 230 K higher annealing temperatures for the formation of a crystalline silica bilayer. The structure formation is related to the presence of germanium that acts as a nucleus for the crystallization of the germania-silica film. For iron-silicates the iron oxide also acts as a nucleus for the crystallization of the silica [165]. The iron-silicate exists only in the crystalline phase [48]. For the ultra-thin germania-silica films only crystalline films were observed.

5.3 Conclusion

The spectro-microscopy studies of ultra-thin germania-silica films on Ru(0001) show that those films can be successfully prepared with different preparation approaches. The XPS measurements and the similarities of the LEEM-IV curves to the silica bilayer indicate a silica bilayer-like structure of the germania-silica films on Ru(0001). The germania can be integrated into the silica matrix due to comparable structural and chemical properties of both oxides. The misfit introduced by the germania could lead to distortions in the film. The initial crystallinity of the first deposited film has a huge influence on the final film. The intensity increase of the LEED spots at around 800 K during the oxidation indicates a successful preparation in contrast to of around 1000 K of a fail approach. A chemical connection between germania and silica can be only observed for a initially disordered film. The addition of germania to a crystalline silica film leads to the desorption of germania. Two separated oxides coexist at lower oxidation temperature. The different deposition sequences indicate a low mobility of germania and silica in the mixed films. The presents of germania leads to lower crystallization temperatures of the germania-silica films compared to pure silica films on Ru(0001). Only the formation of crystalline germania-silica films could be observed.

6 Effects of H_2 exposure on ultra-thin GeO_2 and GeO_2-SiO_2 films

In this chapter, the chemical reaction of molecular hydrogen with ultra-thin germania and mixed germania-silica films will be presented. In a previous work of M. Prieto and co-workers the silica bilayer system was used as a model system for the water formation reaction in a physically confined space [55]. Chemistry in a physically confined space offers many opportunities for tuning chemical reactions [167] [168]. Heterogeneous catalysis is related strongly to chemical reactions on solid surfaces [169]. In model systems for heterogeneous catalysis, the support is typically a flat metal single crystal [10]. Those metal single crystals have been modified by adding oxides on top and additionally nanoparticles [10].

The kinetics of a chemical reaction is influenced by a catalyst [170][169]. The catalyst decreases the activation energy of a chemical reaction [170]. Chemical reactions can happen at lower temperatures with the presence of a catalyst. A catalyst can open alternative pathways of a chemical reaction and can change the selectivity [169]. In addition, a physical confinement can influence the reaction kinetics and then the physical confinement might even act as a catalyst. A physical confinement is not per se a catalyst or improves the selectivity of a chemical reaction. In the special case of the silica bilayer, the hexagonal silica acts as a molecular sieve [171]. The confinement can increase the interactions with the educts to the support and, by this, the probability of the chemical reaction. This is the case for a non-reactive confinement like the silica bilayer system for the water formation on Ru(0001) [55]. The confinement can inhibit the desorption of the product of chemical reaction, which shifts the concentration on the metal support [55] [172]. In addition, the diffusion into the confinement can be inhibited.

An example for chemistry in a confined space are zeolites [173]. Zeolites are complex porous silicates, mainly aluminosilicate compounds [173]. Those pores act as a confinement and as a catalyst for chemical reactions and influence the kinetics [173]. Due to the complex structures of the zeolite, the study of the working catalyst and the identification of the active sites are very difficult. A confinement can be also a macromolecular structure like carbon nanotubes [168]. There are theoretical calculations that a physical confinement can affect chemical reactions, like Diels-Alder reactions in carbon nanotubes [174].

In surface science, a physical confinement can be realized by using, for example, graphene [175] [176] or the silica bilayer system [55]. The silica is chemically inactive to the water formation, only the ruthenium support is chemically active [55]. The silica is chemically inert to hydrogen treatments [55]. A chemically active confinement is also possible like chemically modified silica bilayer. For silica bilayer system, the chemical reaction is localized in the space between the physisorbed silica bilayer and the ruthenium support [55]. The bilayer interacts weakly with the support by van-der-Waals interaction, so the top layer of the silica is different from the bottom layer. Small molecules, like hydrogen, can penetrate into the space between the silica and the ruthenium. The silica bilayer confinement leads to longer contact times of the penetrated small molecules with the ruthenium support. This penetration of small molecules through the silica was calculated by DFT [171] and measured [56]. The formation of water below ultra-thin silica films was measured by spectro-microscopy [55] and by IRAS [56]. Hydrogen can diffuse much easier through the silica network compared to the water. The molecular hydrogen dissociates on the ruthenium [177] and reacts with the oxygen of the oxygen covered 3O-(2x2)-Ru(0001) surface. The water formation below the silica bilayer forms a moving reaction front [55]. A reaction front is observed also for the water formation on bare Ru(0001). The origin of the moving reaction front is related to hydrogen dissociation and the co-adsorption and reaction with oxygen. The adsorbed oxygen has to react or leave the site so that more hydrogen dissociates. The experimentally observed apparent activation energies of the water formation are 0.27 eV for the confined reaction and 0.59 eV on Ru(0001) [55]. Hence, due to the confinement, the activation energy decreases by a factor of around 2.

Theoretical calculations suggest that a chemical reaction in a physically confined space is independent of the chemical nature of the confinement as long as the wall materials are inert to the reactants [57]. Therefore, a chemical reaction in a chemically modified confinement would be similar to the non-modified confinement. The modification of silica films by germania is a candidate for the modification of the silica confinement.

With the LEEM setup, the chemical reaction can be observed in real-time and in-situ [54] [55]. In this chapter the effect of hydrogen treatments on ultra-thin germania and mixed germania-silica films on Ru(0001) is investigated for the first time. For preventing contaminations during the hydrogen dosing, the gas inlet system was purged by alternating the dosing hydrogen into the gas inlet system, with the valve to the specimen chamber closed, and subsequent pumping down this volume. The molecular hydrogen was dosed up to a pressure to $1 \cdot 10^{-6}$ mbar and the germania and germania-silica films were annealed to 470 K.

6.1 Germania

6.1.1 Hydrogen treatment of germania

The chemical reaction between molecular hydrogen and ultra-thin germania films on Ru(0001) is presented in this paragraph. Dosing molecular hydrogen on GeO_2 / Ru(0001) at room temperature leads to an increasing intensity of the LEEM images (E_{kin} = 12 eV). The adsorption of hydrogen changes the surface dipole and the work function [177]. The change of the surface dipole influences the reflectivity for electrons and changes the measured intensity of the LEEM images.

A sequence of LEEM images, taken during a hydrogen treatment, is displayed in figure 6.1. The chemical reaction between H_2 and GeO_2 on Ru(0001) was observed in real-time at 470 K and at $1 \cdot 10^{-6}$ mbar hydrogen pressure. The initial germania film is homogeneously bright in LEEM (E_{kin} = 12 eV). Only atomic steps of the ruthenium support are visible as grey lines. In figure 6.1a, one large dark area is visible in the right center surrounded by the bright germania film. The dark area has a circular shape with a diameter of around 1 μm and can be related to a reacted area. In figure 6.1b, this large dark area has grown in size and additionally small dark spots appear, mainly at step edges. They are not connected to each other. The time difference of figure 6.1a and 6.1b is 32 s. In figure 6.1c, 3 seconds later, the quantity of small dark spots increases compared to figure 6.1b. New dark spots are formed and some spots are now connected and form larger dark areas. The size of the small spots is around 100 nm to 250 nm. The growth of the dark areas continues in the following figures 6.1d to 6.1f. The growth itself is inhomogeneous and in some regions, the dark areas follow the atomically flat terraces of the ruthenium support. The mainly bright image 6.1e turns mainly dark in figure 6.1f. In figure 6.1g, except for a few small bright areas, the complete image shows the dark areas. The dark areas show two slightly different levels of intensity , one deep dark and one slightly brighter. The image is fully dark without contrast in figure 6.1j, due to a rescaling the image looks brighter than image 6.1g. Figure 6.1i and 6.1j show a structured surface with small areas. In figure 6.1k, these initially small areas agglomerate to larger areas and the zoomed image 6.1l shows clearly a separation of two phases.

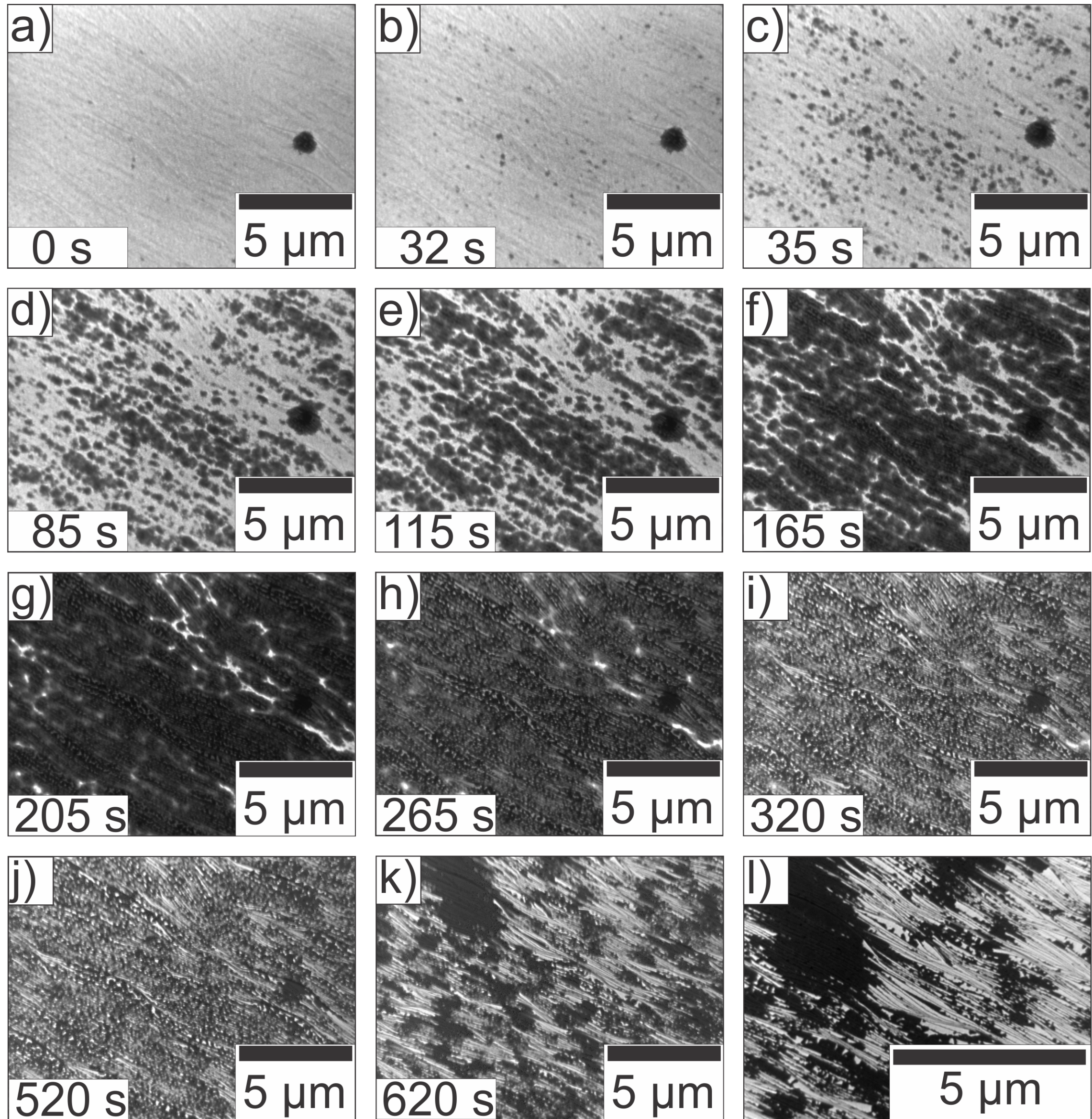

Figure 6.1: a) - k) LEEM (E_{kin} = 12 eV) sequence of the hydrogen treatment at 470 K and $p(H_2) = 1 \cdot 10^{-6}$ mbar on a pure germania film on Ru(0001). Zoomed in between k) and l).

The LEEM images in figure 6.1k and 6.1l clearly show two separated phases. The elemental distribution on the surface was determined by XPEEM of the Ge3d core level. A detailed LEEM and XPEEM comparison at the same surface region of the separated phases is shown in figure 6.2a and 6.2b. The bright areas in LEEM are dark in the Ge3d XPEEM. Therefore, the dark areas in LEEM are covered with germanium. The oxidation state was determined by XPS and shows a complete reduction of germanium (see figure 6.3). The germanium rich phase has a higher kinetic energy than the germanium poor phase.

The XPEEM and LEEM images show very sharp borders of the agglomerated germanium. The agglomeration follows mainly the atomic steps. The analysis of selected areas in XPEEM also shows a minimal Ge concentration in the dark areas in the XPEEM (red curve in figure 6.2c). The Ge concentration is ten times higher in the XPEEM bright areas (green curve in figure 6.2c) compared to in the dark areas. The direct comparison of the intensities in XPEEM is possible because of the similar x-ray beam conditions in the XPEEM scan. The local Ge3d spectra are slightly shifted. The germanium in the lower dense phase has a lower kinetic energy.

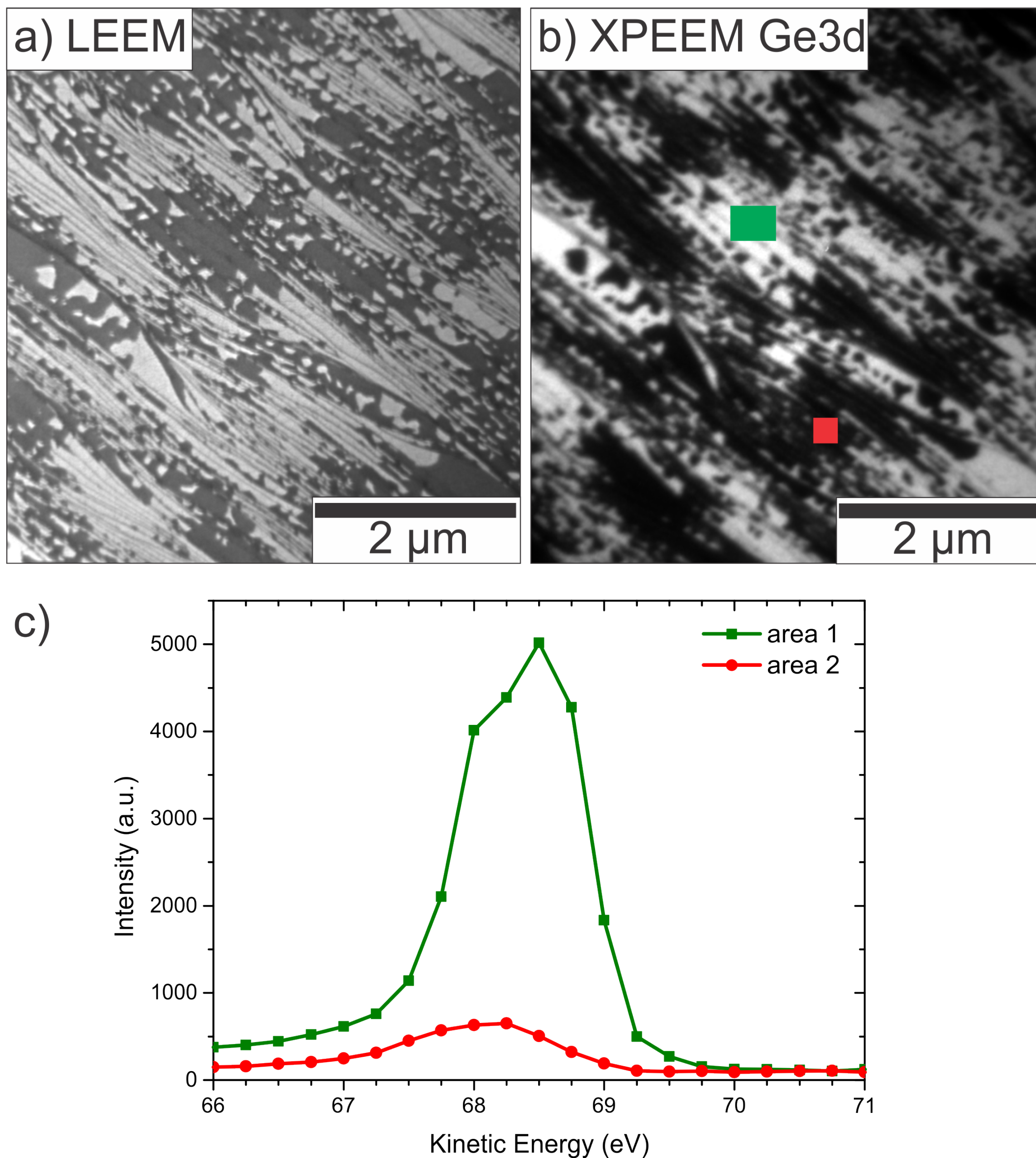

Figure 6.2: LEEM and XPEEM comparison of germania after hydrogen treatment a) LEEM (E_{kin} = 13eV); b) XPEEM Ge3d (E_{kin} = 68.4 eV, hν = 100 eV); c) XPEEM Ge3d scan for selected areas labeled in b). The dark area in LEEM has a ten times higher germanium concentration compared to the bright area.

The comparison of the Ge3d and O1s core levels before and after the hydrogen treatment are shown in figure 6.3. The black XP spectrum shows the Ge3d core level before the hydrogen treatment. The germania XP spectrum shows a single peak due to the broadening in the oxide. The measured binding energy is 31.5 eV for the Ge^{4+} which is the oxidation state of GeO_2.

The spectrum of the Ge3d core level shifted after the hydrogen treatment by around 2.6 eV, from the oxidized Ge3d to $Ge3d_{3/2}$ in the elemental state (see figure 6.3a). The spin-orbit splitting of the Ge3d core level of the germanium is resolved. The peak width of the $Ge3d_{5/2}$ and $Ge3d_{3/2}$ in the oxide is broader compared to the elemental germanium. The binding energy of the $Ge3d_{5/2}$ is 28.4 eV and of the $Ge3d_{3/2}$ is 28.9eV. After the hydrogen treatment the germanium is completely reduced.

The figure 6.3b presents the O1s core level spectra before and after the hydrogen treatment of the GeO_2 film. The binding energy of the O1s in GeO_2 is 530 eV and of oxygen bound to ruthenium 529 eV. The O1s core level shows an asymmetric shape due to the two oxygen components. After the hydrogen treatment the O1s spectrum has nearly vanished. Only some residual oxygen can be determined by XPS, with a binding energy corresponding to oxygen on ruthenium.

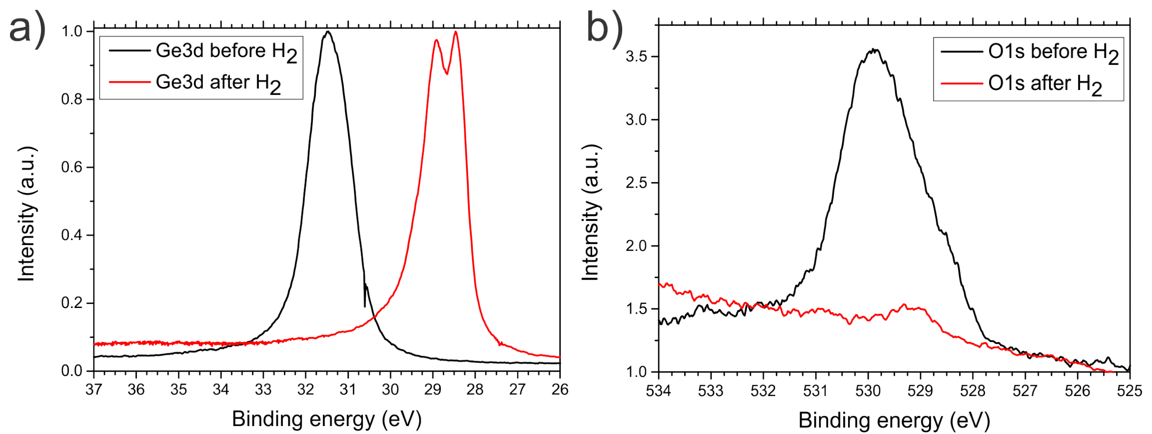

Figure 6.3: a) XPS of Ge3d (hν = 100 eV) and b) XPS of O1s (hν = 600 eV) core level of GeO_2 / Ru(0001) before and after hydrogen treatment, in red and black, respectively. The XP spectra show the complete reduction of germanium, most likely by formation and desorption of water.

Figure 6.4 presents a detailed LEEM analysis of the sample before and after the hydrogen treatment. The germania film before the hydrogen treatment is shown in figure 6.4a. The LEEM image is very homogeneous, only the atomic steps of the Ru(0001) surface are visible. In figure 6.4b and 6.4c LEEM images after the hydrogen treatment are presented. The LEEM image at 9 eV (see figure 6.4b) shows a very strong contrast between the germanium rich and germanium poor phases. For a direct comparison to the initial germania film, a LEEM image (see figure 6.4c) at 13 eV is presented; here the contrast is less strong.

The LEEM-IV curves of the different phases are shown in figure 6.4d. The blue curve is the LEEM-IV measurement before the hydrogen treatment and shows the characteristic double peak between 4 eV and 7 eV of the germania film and a strong dip of the reflectivity at 8 eV. The MEM-LEEM transition before the hydrogen treatment is at 3.5 eV. The dark phase in figure 6.4b shows the green labeled LEEM-IV curve. This phase shows the highest MEM-LEEM transition energy of around 4.6 eV. The red LEEM-IV curve shows the mainly ruthenium covered phase (Ge poor phase). This phase has the lowest MEM-LEEM transition at 2.55 eV. All LEEM-IV curves show significant differences between each other and to the Ru(0001) LEEM-IV. This is in line with the XPEEM measurements.

The reduced film shows a (2x2) LEED pattern with sharp LEED spots (see figure 6.4e). The pattern shows that the germanium has a good large-range order after the hydrogen treatment, comparable to the intitial GeO_2 film. The half-integer (2x2) spots show a blurry surrounding.

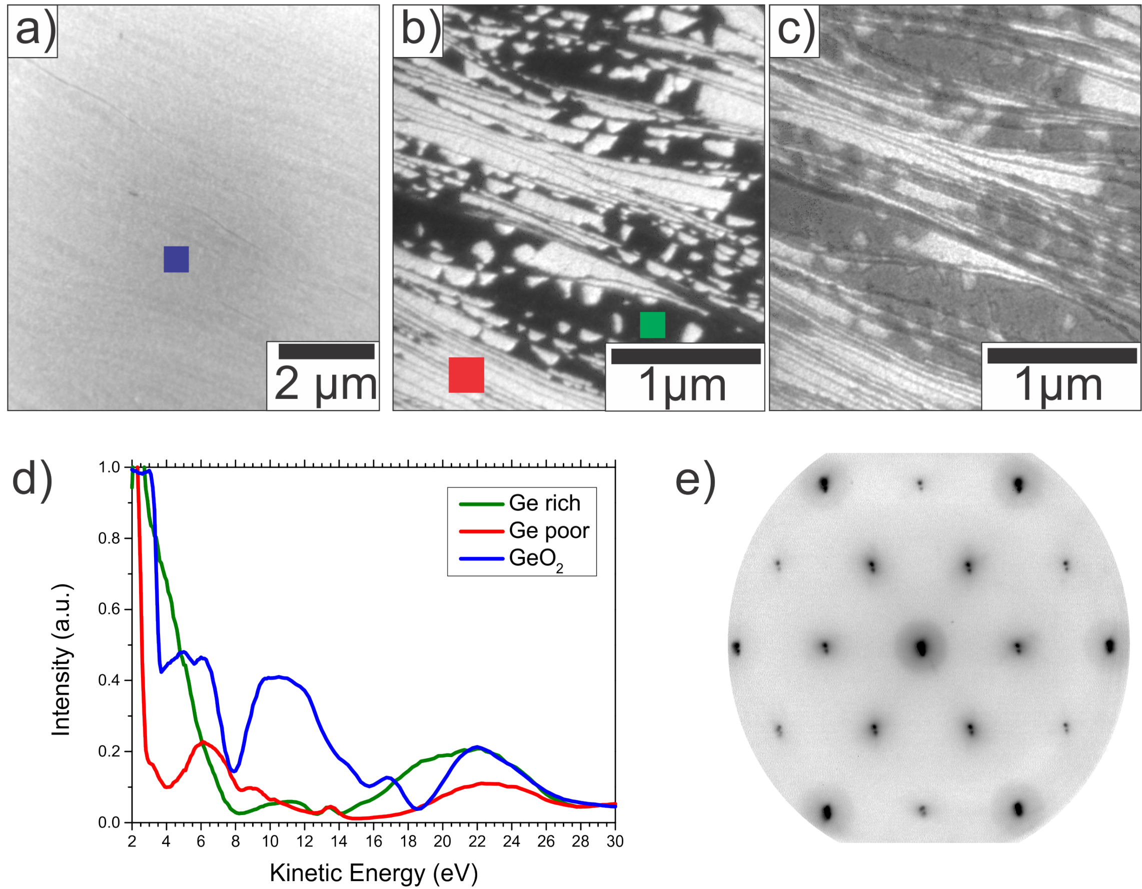

Figure 6.4: a) LEEM of germania before H_2 treatment (E_{kin} = 13 eV), b) LEEM (E_{kin} = 9 eV) and c) LEEM (E_{kin} = 13 eV) after H_2 treatment, d) LEEM-IV of selected areas, e) (2x2) LEED pattern (E_{kin} = 42 eV) after H_2 treatment

6.1.2 Interpretation

Summarizing the experimental results, ultra-thin germania films on Ru(0001) react with molecular hydrogen at 470 K and become completely reduced. The change of contrast in LEEM (see figure 6.1) during the reaction is related to the change of the LEEM-IV curve (see figure 6.4). The work function changes as well. This is confirmed by the detailed LEEM-IV analysis in figure 6.4, which compares the different phases on the surface before and after the chemical reaction. For pure silica films on Ru(0001) the contrast changes due to a work function change [55]. The silica LEEM-IV curve is not changed but shifted by the work function change. In contrast to silica bilayer the germania film is reduced by the hydrogen which changes the LEEM-IV curve.

The full reduction by hydrogen of GeO_2 to Ge is different to the observed chemical reaction of hydrogen with chemisorbed monolayer [178] and physisorbed bilayer SiO_2 on Ru(0001) [55]. For the formation of water the interface oxygen between the silica bilayer and ruthenium is used [55].

The removal of interface oxygen changes the surface dipole and this leads to a shift of 0.8 eV of the Si2p core level [55]. In the germania case, the oxygen signal vanished completely. Consequently the tetrahedral GeO_4 building units of the GeO_2 are destroyed. The formation of hydrogen-oxygen bonds is thermodynamically preferred compared to germanium-oxygen bonds. The XPS measurements show a full reduction of GeO_2 to Ge. The vanished oxygen signal indicates the formation of water. The reaction front of the reduction can be observed clearly by LEEM in real-time and in-situ.

Note that the results of the hydrogen treatment on germania-silica films show an influence of the low-energy electrons of the microscope on the chemical reaction, as will be reported in the following part. For the pure germania films the effect of electron irradiation on the reduction of germania due to the hydrogen treatment could not be determined. The germania is fully reduced on the entire sample, therefore it can be concluded that the reduction of germanium is independent of electron irradiation, however the dynamics could still be locally influenced by the electron beam. These influences cannot be separated in the present study.

The initial chemical reaction might start at defects or holes of a few nanometer sizes, e.g. below the instrumental resolution in these experiments. The initial start of the reaction could be influenced by the electron beam. The dark areas, appearing during the chemical reaction (see figure 6.1), have a circular shape. This indicates that the initial reaction between hydrogen and germania is isotropic. With increasing size of the dark areas, the influence of the atomic steps of the Ru(0001) support increases. The dark areas follow the atomic steps. The initially homogeneous films separate into two phases during the chemical reaction.

The elemental distribution on the surface was determined by XPEEM of the Ge3d core level (see figure 6.2). By the XPEEM measurements, the different contrasts in LEEM can be understood. After the reaction, the dark areas in figure 6.1k and 6.1l are covered with germanium. The bright areas also contain germanium but with a ten times lower concentration compared to the dark areas (see figure 6.2). The LEED pattern in figure 6.4e shows a (2x2) structure, the germanium film after the hydrogen treatment is different compared to the germanium film grown on bare Ru(0001) (see chapter 3). The lattice constant changes from germania to germanium on Ru(0001) by the removal of oxygen. Therefore, a different LEED pattern would be expected like a (3x3) structure. If the lattice constant decreases by a factor of $1/\sqrt{2}$, the surface coverage would decrease by a factor of around 2. That would lead to a (3x3) LEED pattern.

6.2 Germania-Silica

6.2.1 Hydrogen treatment of germania-silica

The chemical reaction between molecular hydrogen and mixed germania-silica films on Ru(0001) is presented in this part. The reaction conditions of the hydrogen treatments are fully comparable to the hydrogen treatments of pure germania and silica films. The mixed germania-silica films for the hydrogen treatments have a stoichiometry of 1.5 ML silica and 0.5 ML germania, e.g., ratio between silica and germania of 3:1. The preparation is similar to the preparation "C" shown in chapter 5. The germania-silica films used for hydrogen treatments show a homogeneous contrast in LEEM at 12 eV kinetic energy. The germanium is homogeneously distributed in the silica matrix; areas with higher germanium concentration could not be found by spectro-microscopy within the resolution limit of the SMART microscope.

Figure 6.5 presents a LEEM image sequence of the chemical reaction between H_2 and ultra-thin GeO_2-SiO_2 film on Ru(0001). The reaction was observed in real-time at 450 K at hydrogen pressure of $1 \cdot 10^{-6}$ mbar. After a reaction time of 40 s, the films shows dark circular areas (see figure 6.5a). In figure 6.5b, the dark areas have grown and some new small areas have formed. In 6.5c, many new small dark spots appeared within 20 s. Mainly the formation of small new dark spots happened close to the existing larger dark spots. The already existing spots and the new spots grow in size and merge (see figures 6.5d and 6.5e) until the complete image is dark (see figure 6.5f).
To see the effect of electron irradiation, the sample was moved from figure 6.5f to 6.5g by a distance of half the beam diameter (20 μm) to a non-irradiated area. The image 6.5g contains the formerly irradiated area and a non-irradiated area. The bright area and the 3 μm circular dark area were not irradiated by electrons before, only the partially visible dark area on top of the image was irradiated. The bright area is free of small dark areas. Within the next 40 s (see figure 6.5g to 6.5h), the large dark area merge with the small dark area. The formation of new small dark areas starts in figure 6.5j after 95 s of electron irradiation. The small dark areas are very similar to the small dark areas observed in figure 6.5d. The new dark areas grow and the complete image is covered with the dark area within 60 s. In figure 6.5k, the borders of the already existing dark areas are still visible (compared to figure 6.5h). Finally, within 15 seconds the image becomes homogeneously dark (see figure 6.5l).

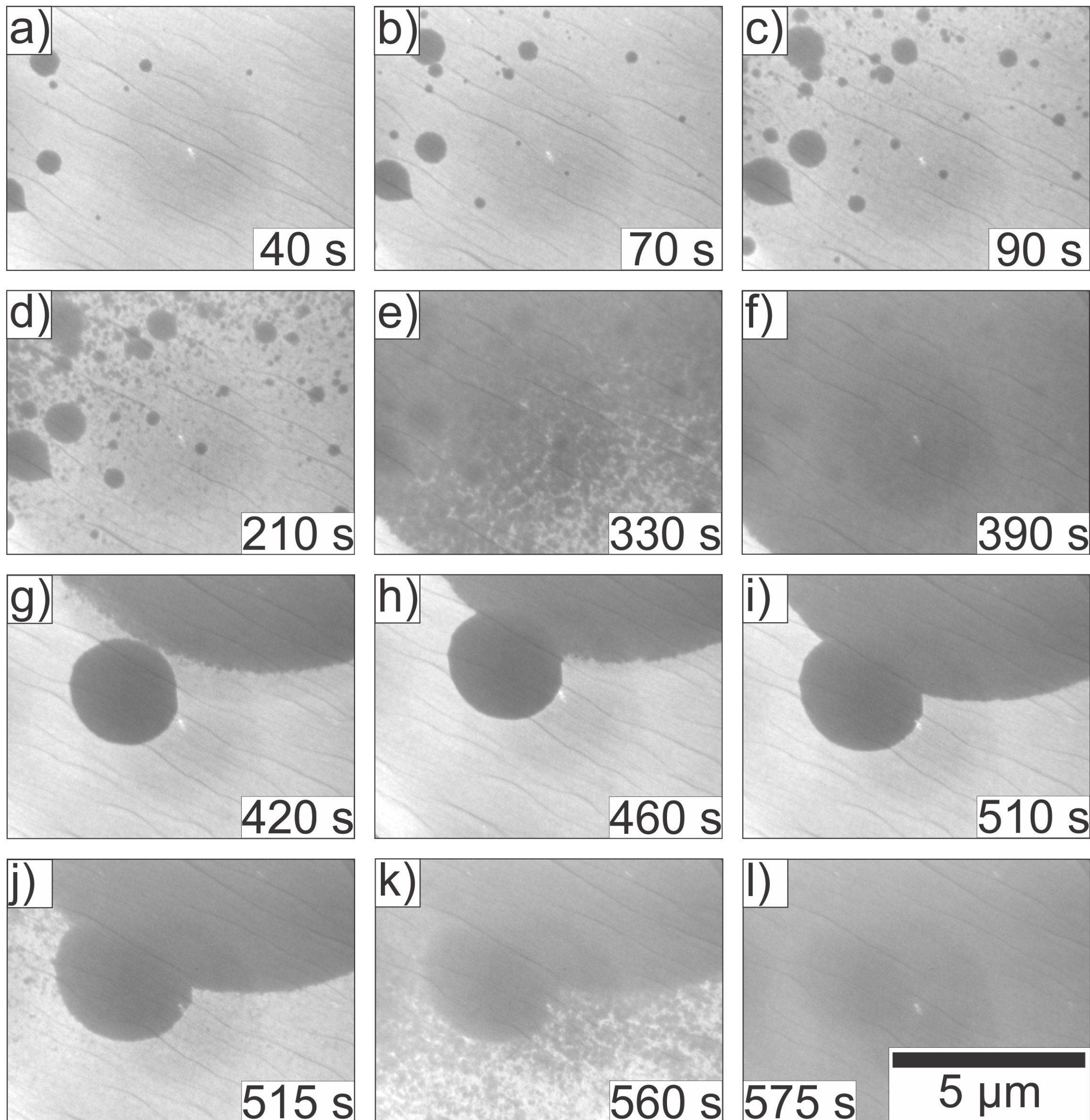

Figure 6.5: a) - l) Hydrogen treatment of GeO_2-SiO_2 on Ru(0001) (p(H_2) = 1 · 10^{-6} mbar, T = 450 K) in followed in LEEM (E_{kin} = 12 eV). a) - c) some dark areas are visible, d) many small dark areas are visible, e) - f) complete illuminated area becomes dark g) effect of electron irradiation (sample moved), bright area and the completely imaged dark area are not irradiated before, h) - i) growth of the dark areas, j) - k) small dark areas appear, l) complete image dark and reacted

The real-time LEEM measurements show strong differences of the contrast change during the hydrogen treatment and electron irradiation. The local chemical information of the Ge3d core level, measured by XPEEM, is presented in figure 6.6 combined with LEEM. Note that the sample area in figure 6.6 was not irradiated by electrons before the XPEEM measurement. The XPEEM measurement was done in UHV and at room temperature.

In figure 6.6a, a Ge3d XPEEM image (E_{kin} = 64.8 eV) is shown with clearly bright and dark areas. The direct comparison of figure 6.6a and the LEEM image 6.6c shows that the bright area in XPEEM is also bright in LEEM. The intensity distribution of the Ge3d XPEEM changes from figure 6.6a to 6.6b. In figure 6.6b, the difference between the two different areas is not as strong as in figure 6.6a. The kinetic energy of the electrons from the reduced germanium is 66.7 eV. The XPEEM scan is presented in figure 6.6d. The black labeled curve is taken in the bright area in figure 6.6a and 6.6c, and the red labeled curve shows the dark area in figure 6.6a and 6.6c, which is bright in figure 6.6b.

The XPEEM scan (see figure 6.6d) of the area bright in LEEM shows mainly non-reduced germanium at a kinetic energy at 65 eV. The second peak (black curve) 66.75 eV is related to beam induced reduction of the germania. The acquisition time of each image is 10 s with a scan direction from lower kinetic energies to higher ones. The sample was irradiated by photons for about 3 min when the signal at E_{kin} = 66.75 eV was detected.

In the XPS measurements, the reduced germanium in the bright phase is missing. Possible irradiation effects come from the photons as well as all exiting electrons. The fast (direct) imaging of the dispersive plane of the energy filter of the SMART microscope avoids or, at least, reduces beam-induced effects. The comparison of the XPEEM scan in figure 6.6d with the μXPS of the Ge3d core level in figure 6.6a shows that the Ge in the bright area (LEEM see 6.6c) is oxidized completely to Ge^{4+}. The LEEM image in figure 6.6c shows small dark spots in the bright area. Those dark spots also contribute to the local XPEEM scan. The LEEM image in figure 6.6c shows dark spots in the bright area, which are also resolved in the XPEEM image of figure 6.6a. The spots are not visible in the XPEEM image in figure 6.6b.

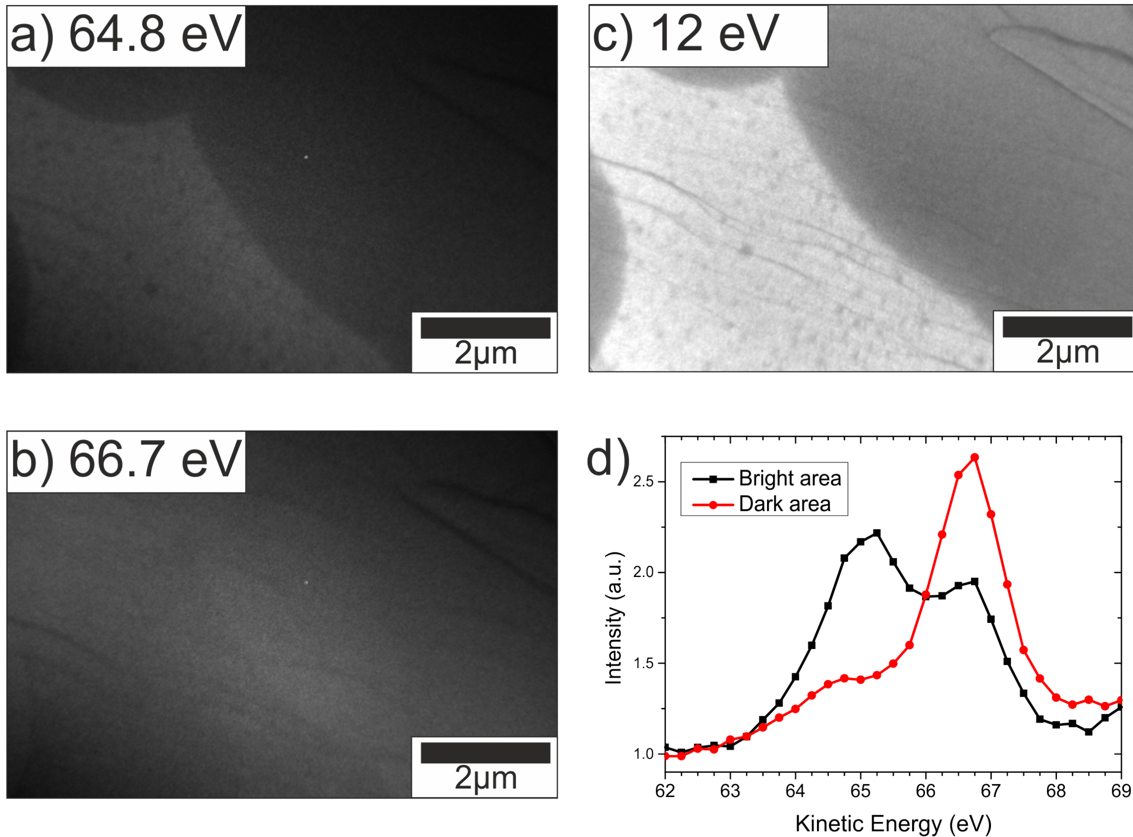

Figure 6.6: XPEEM of GeO_2-SiO_2 after the H_2 treatment (measurement in UHV at RT) a) XPEEM of Ge3d at (E_{kin} = 64.8 eV, hν = 100 eV); b) XPEEM of Ge3d (high intensity in partially reduced area) (E_{kin} = 66.7 eV, hν = 100 eV); c) LEEM (E_{kin} = 12 eV); d) XPEEM scan Ge3d of selected areas. The XPEEM scan of the bright areas shows an x-ray induced partial reduction, due to the long acquisition time.

The XPEEM scan of germania-silica film shows two different germanium species after the hydrogen treatment. The sizes of the different phases, observed in LEEM and XPEEM, are large enough for μXPS. The μXPS for Ge3d, Si2p and O1s for the bright and dark areas are presented in figure 6.7. The Ge3d core level of the in LEEM bright area shows a germanium component in the Ge^{4+} oxidation state with a binding energy of 32.5 eV. The influence of hydrogen on germanium in the bright areas is negligible. The reduced component in the bright area, which is visible in the XPEEM scan, is not visible in the XPS, due to the faster acquisition time.

The Ge3d core level spectrum of the dark area shows clearly the reduced Ge^{2+} component at 30 eV binding energy. The Ge^{4+} component is also present. The ratio between the reduced and non-reduced components is around 1:1.25. So the dark area contains a mixture of reduced and non-reduced germanium.

The difference of the bright area in μXPS (see figure 6.7a) and the Ge3d XPEEM scan in figure 6.6d is related to x-ray induced partial reduction of the germania during the XPEEM measurement.

The XPS of the Si2p is shown in figure 6.7b. The Si2p spectra show one oxidation state of the silicon: the Si^{4+} oxidation state in both the dark and bright areas. The Si2p core level is shifted to higher binding energies(0.2 eV) from the bright to the dark area. The change could be related to the change of the germanium oxidation state. In contrast, for the pure silica bilayer system the Si2p line shifts by 0.79 eV due to the removed dipole in interface between the silica and the ruthenium [55].

Figure 6.7c shows the O1s core level spectra of the bright and dark areas. In contrast to the pure germania film, the mixed oxide is partially reduced and the oxygen signal in XPS is measured. The O1s core level shifts by 0.2 eV to higher binding energies from the bright to the dark area. The oxygen component at 529 eV (related to O-Ru) binding energy is missing in both phases. The initial film shows this component (see preparation "C" chapter 5).

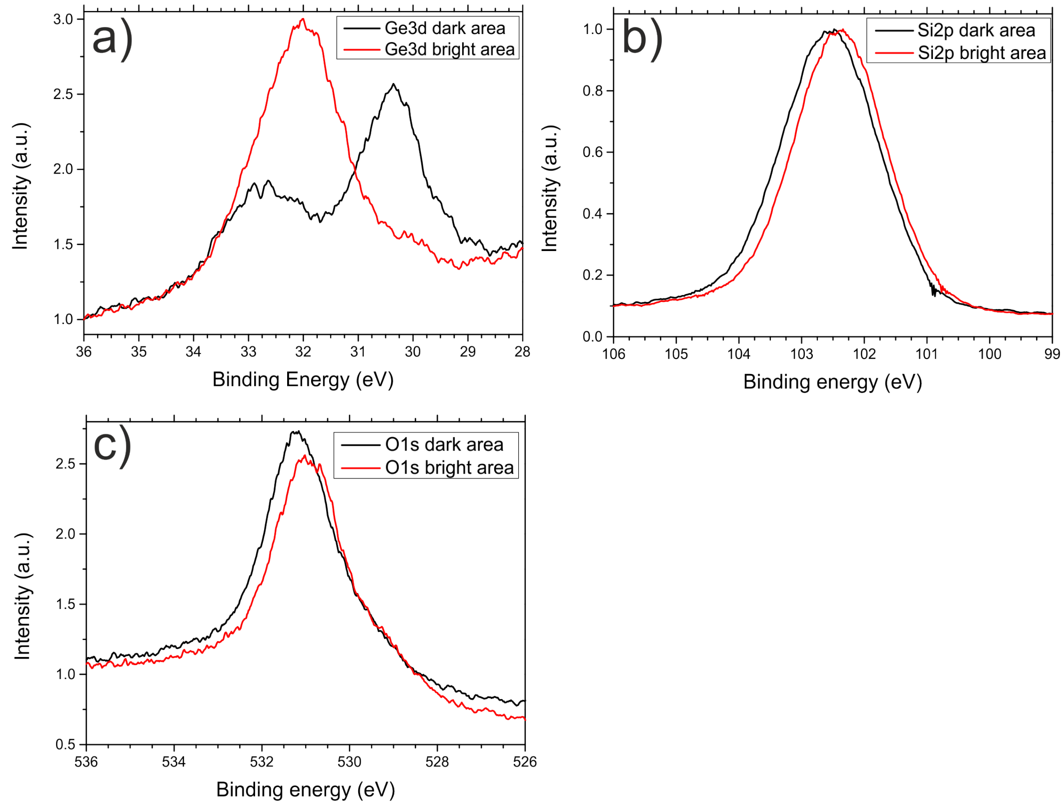

Figure 6.7: XPS (measurement in UHV at RT) of GeO_2-SiO_2 after the hydrogen treatment a) Ge3d (hν = 100 eV) with Ge^{4+} in the bright area and partially reduced germanium in the dark area; b) Si2p (hν = 175 eV) with a shift of 0.2 eV; c) O1s (hν = 600 eV) with a shift of 0.2 eV

The peak shape of the $Ru3d_{5/2}$ core level changes with the amount of oxygen on the ruthenium surface [32] [26]. Therefore, the $Ru3d_{5/2}$ core level also allows the identification of interfacial oxygen underneath the silica bilayer. As shown in figure 6.7c, the O1s component at 529 eV is missing, which can be related to interfacial oxygen between the silica bilayer and the ruthenium [32]. A comparison of the $Ru3d_{5/2}$ core level is presented in figure 6.8. The $Ru3d_{5/2}$ core level is constant during the hydrogen treatment and shows a binding energy of 280 eV.

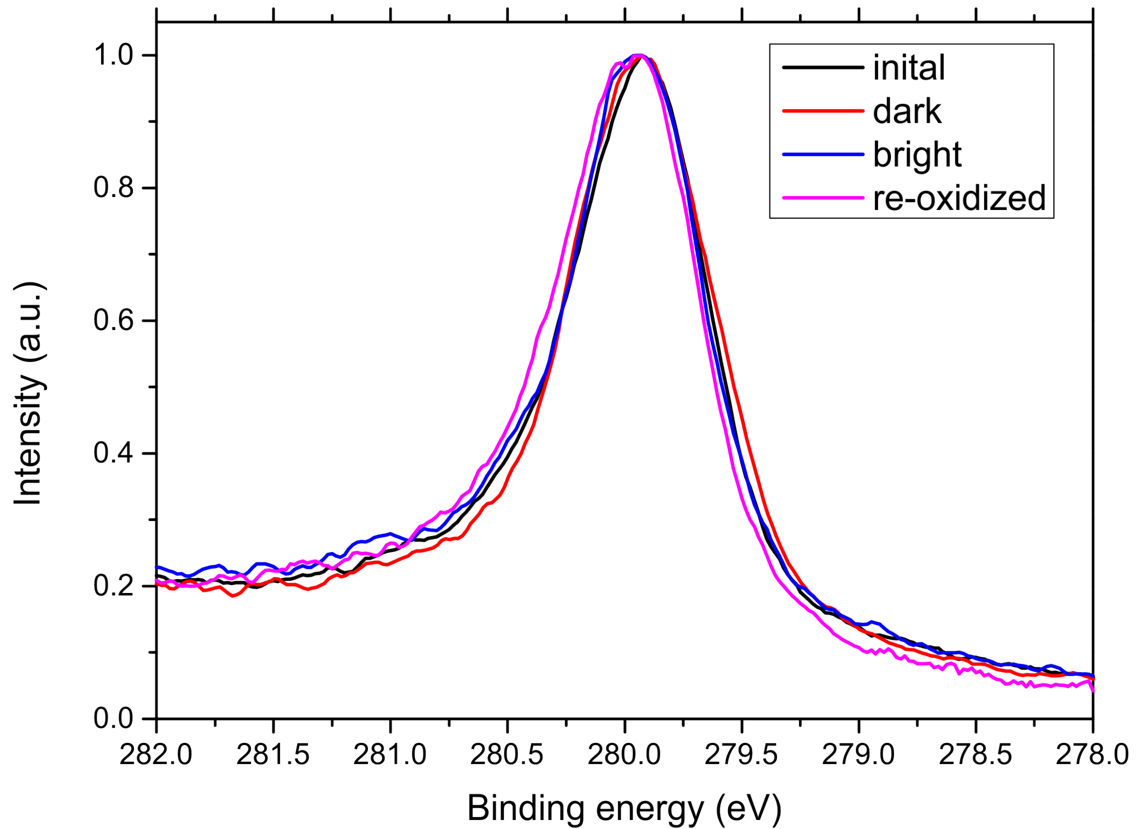

Figure 6.8: Evolution of $Ru3d_{5/2}$ core level during the hydrogen treatment ($h\nu$ = 360 eV).

Figure 6.9 summarizes LEEM, LEEM-IV and LEED measurements of the mixed germania-silica films on Ru(0001) after the hydrogen treatment. In figure 6.9a, a representative LEEM image after the hydrogen treatment with the dark and bright areas is shown. The large dark areas have a circular shape. The shape of the top area shows that two initial circles merged to one large dark area. A detailed view on the bright area shows small dark spots surrounded by the bright phase.

The LEEM-IV curves for both phases are displayed in figure 6.9b. The LEEM-IV curves of the dark and bright phase exhibit the same characteristics, both without very prominent features. The peak positions are very similar to crystalline silica bilayer but less prominent.

The main difference is the shift of the work function by 0.27 eV, the work function of the bright phase is higher than for the dark phase. For kinetic energies lower than 17 eV, the non-reduced phase is bright.

The LEED patterns of the different phases are presented in figure 6.9c for the dark phase and in 6.9d for the bright phase. The bright, non-reduced phase, shows a (2x2) LEED pattern. The LEED pattern of the bright phase is not changed by the hydrogen treatment compared to the initial film. The partially reduced dark phase shows a diffuse (2x2) LEED pattern.

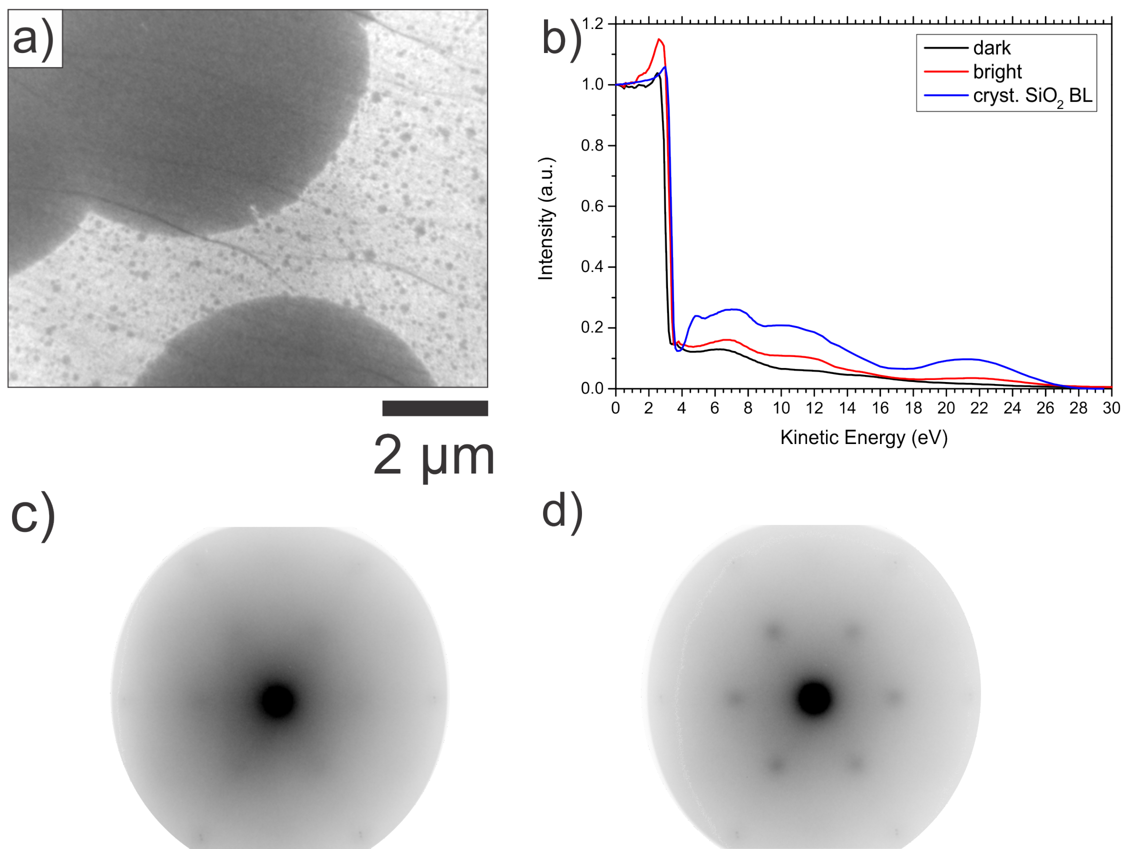

Figure 6.9: a) LEEM image (E_{kin} = 12eV) with the bright and dark phase, b) LEEM-IV of the different areas. The work function is shifted by 0.27 eV from the bright to the dark phase. c) diffuse LEED pattern (E_{kin} = 42eV) of the dark area; d) (2x2) LEED pattern (E_{kin} = 42eV) of the bright area

6.2.2 Reoxidation of germania-silica films

The partially reduced germania-silica films can be reoxidized by annealing in oxygen atmosphere ($1 \cdot 10^{-6}$ mbar O_2) at 690 K. The reoxidized film shows a homogeneous LEEM contrast, the dark areas vanish completely. The LEED pattern of the reoxidized germania-silica film shows (2x2) spots, comparable to the LEED pattern of the initial film. In addition, the LEEM-IV shows the same characteristics of the bright phase, but the MEM-LEEM transition is at 3.36 eV. I.e., the work function shifts by 0.08 eV to higher values compared to the bright phase.
Figure 6.10 presents the XPS measurements after the reoxidation. The XPS of the Ge3d core level shows a peak at 32 eV binding energy. The component of the partially reduced germanium at 30 eV binding energy vanished completely. The XPS of Ge3d after the reoxidation is similar to the initial film. The Si2p core level has a binding energy of 102.3 eV. The binding energy of the bright phase is 102.4 eV. The difference in binding energies is similar to the difference in the MEM-LEEM transition between the non-reduced bright germania-silica film and reoxidized film.

The O1s core level shows a component at 529 eV and the main peak at 531 eV (see figure 6.10c). The O1s peak is similar to that one of the initial germania-silica film (see preparation “C” in chapter 5). The oxygen component at 529 eV is missing in both O1s XPS spectra of the bright and dark areas after the hydrogen treatment (see figure 6.7). Therefore, this oxygen component, with the lowest binding energy, reacts with the hydrogen before the germania becomes reduced.

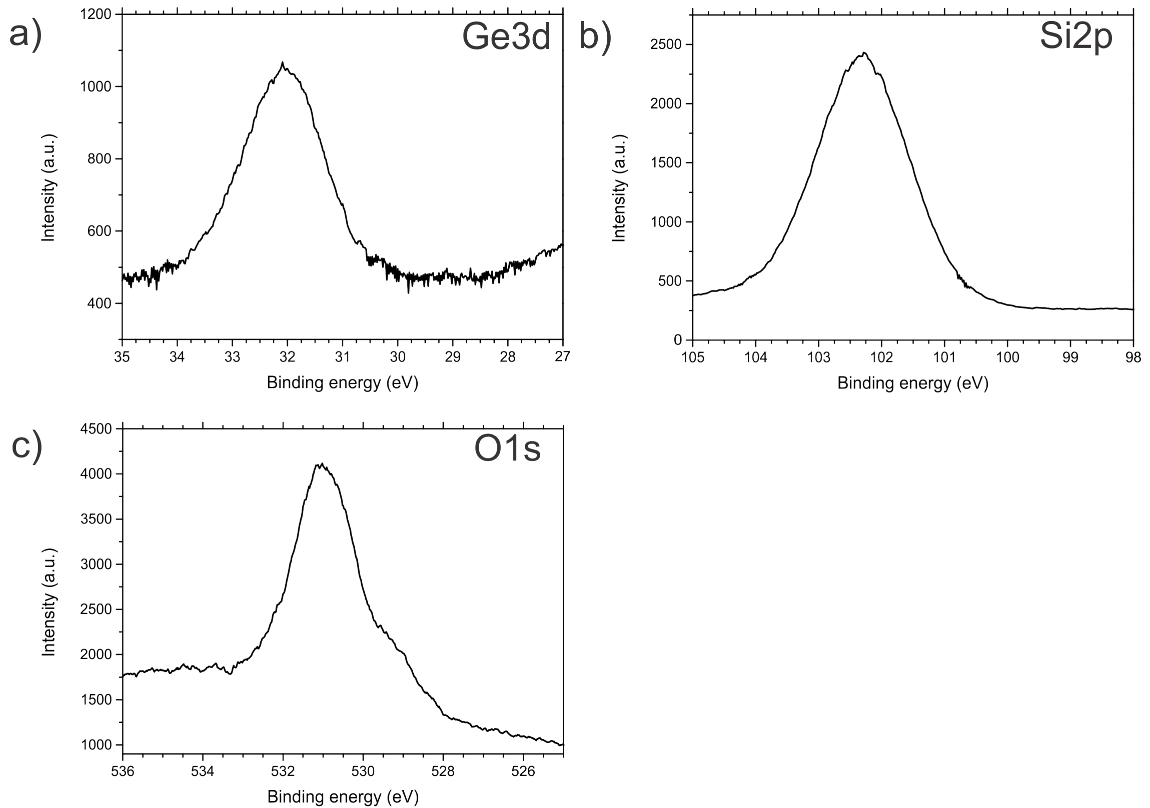

Figure 6.10: XPS of reoxidized germania-silica ($1 \cdot 10^{-6}$ mbar O_2 at 690 K): a) Ge3d (hν = 100 eV) with completely oxidized Ge; b) Si2p (hν = 175 eV); c) O1s (hν = 600 eV) with the oxygen component at 529 eV binding energy

The LEEM-IV and LEED results of the reoxidized film are collected in figure 6.11. The MEM-LEEM transition are presented in figure 6.11a for the reoxidized, the bright and dark phase. The MEM-LEEM transition for the reoxidized film is 3.38 eV, in contrast the MEM-LEEM transition of the bright phase is 3.29 eV and for the dark phase 3.0 eV. The LEEM-IV curves of the reoxidized film and for the bright phase are very similar (see figure 6.11b). The dark phase shows a lower reflectivity compared to the reoxidized film. The LEED pattern of the reoxidized films shows (2x2) spots, similar to the initial film and the bright phase (see figure 6.11c). The sample shows a homogeneous LEEM image (see figure 6.11d). The dark phase vanished completely during the reoxidation.

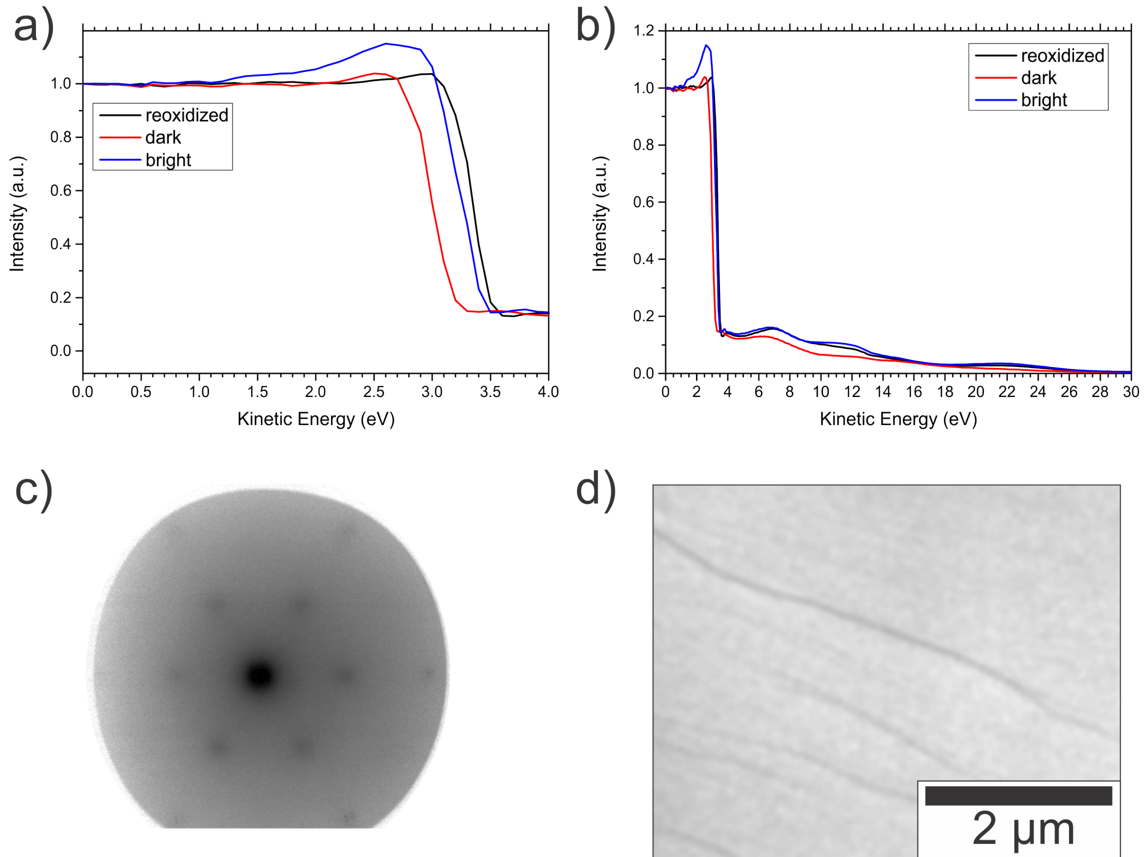

Figure 6.11: Reoxidation of germania-silica a) comparison of MEM-LEEM transitions of the reoxidized film compared with the two phases of the reacted film. b) LEEM-IV comparison; c) (2x2) LEED pattern (E_{kin} = 42 eV); d) LEEM image of the reoxidized film (E_{kin} = 12 eV)

6.2.3 Interpretation

The results of the multi-method study of the chemical reaction between ultra-thin germania-silica with molecular hydrogen will be discussed in the following part. During the experiments it turned out that germania and germania-silica film are more sensitive to beam induced effects than pure silica. The electron beam of the microscope shows a strong influence on the chemical reaction between the germania-silica film and the hydrogen. This can be related to the chemical activity of the germania compared to the chemically inert silica. The chemical reaction is locally enhanced at the electron irradiated area. However, the entire surface reacts in a similar way. The effect of low energy electrons (E_{kin} = 12 eV) during the hydrogen treatment of ultra-thin germania-silica films is shown in figure 6.5. The electron irradiation leads to the formation of small dark areas that grow with the reaction time and form a completely dark surface (see figure 6.5). Also the non-irradiated surface area reacts with hydrogen to the dark phase (see figure 6.6).

The bombardment with electrons can change the structure of an oxide [179]. The effect of the electron irradiation depends on the dose and the energy of the electron beam [180]. Electrons with a few hundred electron volts can change the composition and structure of samples, which are used for Auger electron spectroscopy [91] and LEED [181]. Electron bombardment is used for hydroxylation of the chemically inert silica bilayer [182].

The electron flux of the SMART microscope on the sample is 200 nA. The electron beam is focused on a surface area with a diameter of 20 μm. This corresponds to a flux of 4000 e^- / (s $\cdot$ nm^2) [183]. The electron impact on a SiO_2 unit cell is 250 electrons per second and unit cell (e^- / (s $\cdot$ SiO_2)) [183]. D. Gottlob and co-workers studied the effects of electron irradiation on silica [183]. On pure silica, the effect of low energy electrons in the energy range below 50 eV is very weak. Electron beam induced effects on silica become observable starting at energies around 50 eV in the times used in the present case, and become strong only above 100 eV. Beam induced effects of low energy electrons in UHV cannot be observed for LEEM and LEED measurement for silica if the time scale is short (minutes).

One possible explanation could be that the molecular hydrogen is ionized by the electron beam in the gas phase. The hydrogen molecules can be ionized in the vacuum between the objective lens and the sample and accelerated on the sample. This would lead to a bombardment of protons with energy of up to 15 keV. This effect is independent of the sample. However, for pure silica this effect has not been observed.

The XPEEM scan (see figure 6.6d) shows a partial reduction of the germanium from Ge^{4+} to Ge^{2+}, which was studied in more detail by μXPS (see figure 6.7). Due to beam damage effects, the XPEEM scan contains also reduced germanium in the bright area. The Ge3d μXPS of the bright phase contains only non-reduced germanium in the Ge^{4+} oxidation state (see figure 6.7a). The dark phase contains mainly Ge^{2+} but also Ge^{4+}. The reduction of the germania is incomplete.

The Si2p core level is shifted by 0.2 eV from the bright to the dark phase (see figure 6.7b). The silicon is not reduced by the hydrogen. The shift of the Si2p core level can be related to the change of the chemical environment of the silicon due to the partial reduction of the germanium and to the change of the dipole at the germania-silica / ruthenium interface. For the silica bilayer, the Si2p core level shifts due to the removal of of the oxygen - ruthenium dipoles at the silica / ruthenium interface [55] [184] [185].

The O1s core level shifts from the bright to the dark phase by 0.2 eV (see figure 6.7c). During the hydrogen treatment, the difference of the O1s core levels during the hydrogen treatment (see figure 6.7c) compared to the initial (see chapter 5) and reoxidized film (see figure 6.10c) is the oxygen component with a binding energy of 529 eV (O-Ru [146]).

This oxygen component is present in the initial film and in the reoxidized one. This 529 eV oxygen component is associated with oxygen which is removed in the bright and dark areas by hydrogen without the reduction of germania (see figure 6.7c).

For pure silica the contrast change in LEEM is related to a change of the work-function, due to the removal of the interfacial oxygen in a physically confined space [55]. The structure of the silica is unaffected to the hydrogen [55] and the LEEM-IV curves are similar before and after the hydrogen treatment, only shifted by the work function change [55]. In contrast to the silica system, the change of the LEEM image during the hydrogen treatment of germania-silica films is related to the change of the LEEM-IV curve (see figure 6.11b) due to a structural change of the film (see change of the LEED pattern 6.9c and 6.9d).

The partially reduced dark phase has a 0.29 eV lower work function than the non-reduced bright phase of the germania-silica film (see figure 6.9b and 6.11a). The shift of the MEM-LEEM transition is slightly larger than the shift in the Si2p XPS core levels (0.2 eV). In addition, the increase of the work function of the reoxidized film compared to the non-reduced bright phase indicates the formation of interfacial oxygen due to the reoxidation and the reaction of hydrogen with interfacial oxygen in a chemically confined space between the ultra-thin germania-silica film and the oxygen covered ruthenium. Figure 6.11 shows that the work function of the sample increases with an increasing oxygen amount which correlates with the XPS measurements (see figures 6.7 and 6.10).

The hydrogen reacts with interfacial oxygen between the silica bilayer an the ruthenium support [55]. Due to the removal of interfacial oxygen by the hydrogen, a change of the Ru3d core level is expected, which can be observed of the different oxygen phases on Ru(0001) underneath the silica bilayer [26]. Therefore, a change of the Ru3d core level for the germania-silica system on Ru(0001) can be expected similar to the silica bilayer system [26]. The Ru3d core level in figure 6.8 shows that the Ru3d is constant and independent of the different oxidation states and phases of the germania-silica film.

This would contradict the assumption of the reaction of hydrogen with interfacial oxygen if the Ru3d core level shows a similar behavior as observed for the pure silica system. However, the Ge3d shows the Ge^{4+} oxidation state and the oxygen component at 529 eV binding energy (see figure 6.7) is missing due to the hydrogen treatment. The removing of the oxygen bond does not influence the structure of the bright phase but shifts the Si2p and O1s core level by 0.2 eV and the work function by around 0.1 eV. This would indicate the water formation reaction in the physically confined space between the germania-silica film and the ruthenium.

The H_2 dissociates at the Ru(0001) surface [177] and reacts with the oxygen on the ruthenium. A direct chemical reaction between H_2 and Ge^{4+} is unlikely. The XPS results of the bright phase show that the oxygen component at 529 eV binding energy is missing and the germanium is completely oxidized. The reaction continues with the partial reduction of the germania after the reaction of dissociated hydrogen with the oxygen on the ruthenium. A possible explanation could be that after the reaction of the hydrogen with the oxygen on the ruthenium the confinement effect is lost and the hydrogen can react with the germania-silica film at the germania sites. Further research is required to clarify the reaction step from the reaction at the oxygen on ruthenium to the Ge^{4+} and the role of the low-energy electron during the reaction.

The μLEED on the dark and bright phase demonstrate that the structure during the hydrogen treatment changes in the reduced areas. The bright non-reduced bright phase shows a (2x2) LEED pattern (see figure 6.9d), similar to the initial LEED pattern of the germania-silica film. The structure of the bright phase is stable but the oxygen component with 529 eV binding energy is missing. The partially reduced dark phase has a diffuse (2x2) LEED pattern (see figure 6.9c). A diffuse LEED is observed for structures if a long-range order is missing. Due to the presence of the Si^{4+} state, the presence of SiO_4 tetrahedral building units can be assumed. For the partially reduced germania, the tetrahedral building units of the reduced germania-silica were destroyed by the hydrogen. Due to the stoichiometry of the initial film ($Ge_{0.25}$ $Si_{0.75}O_2$), the silica structure is stable in the hydrogen treatment and the germania is partially reduced. Therefore the majority of the oxygen bonds and tetrahedral building units are still present. Due to the partial reduction of the germania, partially the Ge-O bonds were removed, which lead to a loss of order but the structure is only distorted and may relax which changes the (2x2) LEED pattern to a diffuse one.

For germania-silica films on Ru(0001) with 10 % germania, a very similar behavior was observed [186]. The hydrogen removes the interfacial oxygen and in a following step the germania becomes reduced. A reaction front similar to pure silica can be observed [186]. The activation energy of the water formation reaction is similar to the activation energy of the water formation reaction on pure silica, however a pre-exponential factor is observed [186].

6.3 Conclusion

The chemical reaction between hydrogen and ultra-thin germania and germania-silica films on Ru(0001) show different results as the well-known hydrogen treatment on pure silica films on Ru(0001). The germania-silica films show a chemical behavior between the bare silica and germania films on Ru(0001). The germania films become completely reduced and the germanium segregates after the hydrogen treatment. That can be expected by the low activation energy for the GeO_2 reduction by H_2 (18.4 kcal/mol) [58] compared to 85 kcal/mol for SiO_2 [59], which is chemically inert within the used reaction parameters. Also, the germania-silica films are chemically active to the hydrogen treatment. Therefore the prove of the assumption of Marx and co-workers [57] cannot be done with the used system. The low-energy electron beam of the LEEM microscope influences the chemical reaction. The electron beam leads to local enhanced reaction. However, the entire surface reacts. Different mechanisms are possible of the locally enhanced reaction of the irradiated area. The hydrogen reacted with the oxygen in the confined space between the germania-silica film and in a following reaction the germania-silica film becomes partially reduced at the germania sites.

Bibliography

[1] H.-J. Freund and G. Pacchioni. Oxide ultra-thin films on metals: new materials for the design of supported metal catalysts. *Chemical Society Reviews*, 37(10):2224, 2008.

[2] A. H. Castro Neto, F. Guinea, N. M. R. Peres, K. S. Novoselov, and A. K. Geim. The electronic properties of graphene. *Reviews of Modern Physics*, 81(1):109–162, 2009.

[3] B. Lalmi, H. Oughaddou, H. Enriquez, A. Kara, S. Vizzini, B. Ealet, and B. Aufray. Epitaxial growth of a silicene sheet. *Applied Physics Letters*, 97(22):223109, 2010.

[4] M. E. Dávila, L. Xian, S. Cahangirov, A. Rubio, and G. Le Lay. Germanene: a novel two-dimensional germanium allotrope akin to graphene and silicene. *New Journal of Physics*, 16(9):095002, 2014.

[5] A. Goriachko, He, M. Knapp, H. Over, M. Corso, Th. Brugger, S. Berner, J. Osterwalder, and Th. Greber. Self-Assembly of a Hexagonal Boron Nitride Nanomesh on Ru(0001). *Langmuir*, 23(6):2928–2931, 2007.

[6] J. A. Miwa, S. Ulstrup, S. G. Sørensen, M. Dendzik, A. Grubišić Čabo, M. Bianchi, J. Vang Lauritsen, and P. Hofmann. Electronic Structure of Epitaxial Single-Layer MoS_2. *Physical Review Letters*, 114(4), 2015.

[7] Alessandro Sala. *Characterization of iron oxide thin films as a support for catalytically active nanoparticles*. PhD thesis, FU Berlin, 2013.

[8] S. Shaikhutdinov and H.-J. Freund. Ultrathin Silica Films on Metals: The Long and Winding Road to Understanding the Atomic Structure. *Advanced Materials*, 25(1):49 – 67, 2013.

[9] A. L. Lewandowski, P. Schlexer, C. Büchner, E. M. Davis, H. Burrall, K. M. Burson, W.-D. Schneider, M. Heyde, G. Pacchioni, and H.-J. Freund. Atomic structure of a metal-supported two-dimensional germania film. *Phys. Rev. B*, 97:115406, 2018.

[10] J. Sauer and H.-J. Freund. Models in Catalysis. *Catalysis Letters*, 145(1):109–125, 2014.

[11] G. Ertl, H. Knözinger, F. Schüth, and J. Weitkamp, editors. *Handbook of Heterogeneous Catalysis*. Wiley-VCH Verlag, 2008.

[12] N. Mizuno and M. Misono. Heterogeneous catalysis. *Chemical Reviews*, 98(1):199–218, 1998.

[13] J. Weitkamp. Zeolites and catalysis. *Solid State Ionics*, 131(1-2):175–188, 2000.

[14] J. G. Bendoraitis, A. W. Chester, F. G. Dwyer, and W. E. Garwood. Pore Size and Shape Effects in Zeolite Catalysis. In *Studies in Surface Science and Catalysis*, pages 669–675. Elsevier, 1986.

[15] N. Kasian, E. Verheyen, G. Vanbutsele, K. Houthoofd, T. I. Koranyi, J. A. Martens, and C. E. A. Kirschhock. Catalytic activity of germanosilicate UTL zeolite in bifunctional hydroisomerisation of n-decane. *Microporous and Mesoporous Materials*, 166:153–160, 2013.

[16] R. Yuan, N. Claes, E. Verheyen, A. Tuel, S. Bals, E. Breynaert, J. A. Martens, and C. E. A. Kirschhock. Synthesis of an IWW-type germanosilicate zeolite using 5-azonia-spiro[4,4]nonane as a structure directing agent. *New Journal of Chemistry*, 40(5):4319–4324, 2016.

[17] N. Kasian, G. Vanbutsele, K. Houthoofd, T. I. Koranyi, J. A. Martens, and C. E. A. Kirschhock. Catalytic activity and extra-large pores of germanosilicate UTL zeolite demonstrated with decane test reaction. *Catalysis Science & Technology*, 1(2):246, 2011.

[18] M. Micoulaut, L. Cormier, and G. S. Henderson. The structure of amorphous, crystalline and liquid GeO_2. *Journal of Physics: Condensed Matter*, 18(45):753–784, 2006.

[19] A. L. Lewandowski, P. Schlexer, S. Tosoni, L. Gura, P. Marschalik, C. Büchner, H. Burrall, K. M. Burson, W.-D.Schneider, G. Pacchioni, and M. Heyde. Determination of Silica and Germania Film Network Structures on Ru(0001) at the Atomic Scale. *The Journal of Physical Chemistry C*, 2018.

[20] Y. Y. Huang, A. Sarkar, and P. C. Schultz. Relationship between composition, density and refractive index for germania silica glasses. *Journal of Non-Crystalline Solids*, 27(1):29–37, 1978.

[21] O. Majérus, L. Cormier, D. R. Neuville, L. Galoisy, and G. Calas. The structure of SiO_2-GeO_2 glasses: A spectroscopic study. *Journal of Non-Crystalline Solids*, 354(18):2004–2009, 2008.

[22] E. Bauer. *Surface Microscopy with Low Energy Electrons*. Springer New York, 2014.

[23] J. I. Flege and D. C. Grinter. In situ studies of oxide nucleation, growth, and transformation using slow electrons. *Progress in Surface Science*, 93(2):21–45, 2018.

[24] B. Yang, W.E. Kaden, X. Yu, J. A. Boscoboinik, Y. Martynova, L. Lichtenstein, M. Heyde, M. Sterrer, R. Włodarczyk, M. Sierka, J. Sauer, S. Shaikhutdinov, and H.-J. Freund. Thin silica films on Ru(0001): monolayer, bilayer and three-dimensional networks of [SiO4] tetrahedra. *Phys. Chem. Chem. Phys.*, 14:11344 – 11351, 2012.

[25] J. Weissenrieder, S. Kaya, J.-L. Lu, H.-J. Gao, S. Shaikhutdinov, H.-J. Freund, M. Sierka, T. K. Todorova, and J. Sauer. Atomic Structure of a Thin Silica Film on a Mo(112) Substrate: A Two-Dimensional Network of SiO_4 Tetrahedra. *Phys. Rev. Lett.*, 95:076103, 2005.

[26] H. W. Klemm, M. J. Prieto, G. Peschel, A. Fuhrich, E. Madej, F. Xiong, D. Menzel, Th. Schmidt, and H.-J. Freund. Formation and Evolution of Ultrathin Silica Polymorphs on Ru(0001) Studied with Combined in Situ, Real-Time Methods. *The Journal of Physical Chemistry C*, 123(13):8228–8243, 2018.

[27] H. Tissot, X. Weng, P. Schlexer, G. Pacchioni, S. Shaikhutdinov, and H.-J. Freund. Ultrathin silica films on Pd(111): Structure and adsorption properties. *Surface Science*, 2018.

[28] A. S. Crampton, C. J. Ridge, M. D. Rötzer, G. Zwaschka, T. Braun, V. D'Elia, J.-M. Basset, F. F. Schweinberger, S. Günther, and U. Heiz. Atomic Structure Control of Silica Thin Films on Pt(111). *The Journal of Physical Chemistry C*, 119(24):13665–13669, 2015.

[29] D. Löffler, J. J. Uhlrich, M. Baron, B. Yang, X. Yu, L. Lichtenstein, L. Heinke, C. Büchner, M. Heyde, S. Shaikhutdinov, H.-J. Freund, R. Włodarczyk, M. Sierka, and J. Sauer. Growth and Structure of Crystalline Silica Sheet on Ru(0001). *Phys. Rev. Lett.*, 105:146104, 2010.

[30] L. Lichtenstein, M. Heyde, and H.-J. Freund. Atomic Arrangement in Two-Dimensional Silica: From Crystalline to Vitreous Structures. *The Journal of Physical Chemistry C*, 116(38):20426–20432, 2012.

[31] H.W. Klemm, G. Peschel, E. Madej, A. Fuhrich, M. Timm, D. Menzel, Th. Schmidt, and H.-J. Freund. Preparation of silica films on Ru(0001): A LEEM/PEEM study. *Surface Science*, 643:45–51, 2016.

[32] Hagen W. Klemm. *Formation and properties of ultrathin silicon dioxide films on Ru(0001).* Phd thesis, TU Berlin, 2018.

[33] W. H. Zachariasen. THE ATOMIC ARRANGEMENT IN GLASS. *Journal of the American Chemical Society*, 54(10):3841–3851, 1932.

[34] L. Lichtenstein, C. Büchner, B. Yang, S. Shaikhutdinov, M. Heyde, M. Sierka, R. Włodarczyk, J. Sauer, and H.-J. Freund. The atomic structure of a metal-supported vitreous thin silica film. *Angewandte Chemie International Edition*, 51(2):404 – 407, 2012.

[35] G. S. Hutchings, J.-H. Jhang, C. Zhou, D. Hynek, U. D. Schwarz, and E. I. Altman. Epitaxial Ni_xPd_{1-x} (111) Alloy Substrates with Continuously Tunable Lattice Constants for 2D Materials Growth. *ACS Applied Materials & Interfaces*, 9(12):11266–11271, 2017.

[36] X. Yu, B. Yang, J. A. Boscoboinik, S. Shaikhutdinov, and H.-J. Freund. Support effects on the atomic structure of ultrathin silica films on metals. *Applied Physics Letters*, 100(15):151608, 2012.

[37] C. Büchner, L. Lichtenstein, X. Yu, J. A. Boscoboinik, B. Yang, W. E. Kaden, M. Heyde, S. Shaikhutdinov, R. Włodarczyk, M. Sierka, J.Sauer, and H.-J. Freund. Ultrathin Silica Films: The Atomic Structure of Two-Dimensional Crystals and Glasses. *Chemistry - A European Journal*, 20(30):9176–9183, 2014.

[38] D.Kuhness, H. J. Yang, H. W. Klemm, M. Prieto, G. Peschel, A. Fuhrich, D. Menzel, Th. Schmidt, X. Yu, S. Shaikhutdinov, A. Lewandowski, M. Heyde, A. Kelemen, R. Włodarczyk, D. Usvyat, M. Schütz, J. Sauer, and H.-J. Freund. A Two-Dimensional 'Zigzag' Silica Polymorph on a Metal Support. *Journal of the American Chemical Society*, 140(19):6164–6168, 2018.

[39] C. Büchner and M. Heyde. Two-dimensional silica opens new perspectives. *Progress in Surface Science*, 92(4):341–374, 2017.

[40] A. Malashevich, S. Ismail-Beigi, and E. I. Altman. Directing the Structure of Two-Dimensional Silica and Silicates. *The Journal of Physical Chemistry C*, 120(47):26770–26781, 2016.

[41] M. P. McDaniel. A Review of the Phillips Supported Chromium Catalyst and Its Commercial Use for Ethylene Polymerization. *Advances in Catalysis*, 53:123–606, 2010.

[42] H.-J. Freund. Models for heterogeneous catalysts: studies at the atomic level. *Rendiconti Lincei*, 28(S1):5–18, 2016.

[43] Q. Pan, L. Li, S. Shaikhutdinov, and H.-J. Freund. Planar model system of the Phillips (Cr/SiO_2) catalyst based on a well-defined thin silicate film. *Journal of Catalysis*, 357:12–19, 2018.

[44] N. Stanley, Th. Chenal, Th. Delaunay, R. Saint-Loup, N. Jacquel, and Ph. Zinck. Bimetallic Catalytic Systems Based on Sb, Ge and Ti for the Synthesis of Poly(ethylene terephthalate-co-isosorbide terephthalate). *Polymers*, 9(11):590, 2017.

[45] S. Shaikhutdinov and H.-J. Freund. Metal-Supported Aluminosilicate Ultrathin Films as a Versatile Tool for Studying the Surface Chemistry of Zeolites. *Chem. Phys. Chem.*, 14(1):71 – 77, 2013.

[46] F. D. Fischer, J. Sauer, X. Yu, J. A. Boscoboinik, S. Shaikhutdinov, and H.-J. Freund. Ultrathin Ti-Silicate Film on a Ru(0001) Surface. *The Journal of Physical Chemistry C*, 119(27):15443–15448, 2015.

[47] R. Włodarczyk, J. Sauer, X. Yu, J. A. Boscoboinik, B. Yang, S. Shaikhutdinov, and H.-J. Freund. Atomic Structure of an Ultrathin Fe-Silicate Film Grown on a Metal: A Monolayer of Clay? *Journal of the American Chemical Society*, 135(51):19222–19228, 2013.

[48] Gina Peschel. *Growth and structure of ultrathin silicates and germanates containing iron oxide.* Phd thesis, FU Berlin, 2018.

[49] M. P. McDaniel. A Review of the Phillips Supported Chromium Catalyst and Its Commercial Use for Ethylene Polymerization. In *Advances in Catalysis*, pages 123–606. Elsevier, 2010.

[50] W. Loewenstein. The distribution of aluminium in the tetrahedra of silicates and aluminates. *American Mineralogist*, 39:92 – 96, 1954.

[51] M. Mundschau, M. E. Kordesch, B. Rausenberger, W. Engel, A. M. Bradshaw, and E. Zeitler. Real-time observation of the nucleation and propagation of reaction fronts on surfaces using photoemission electron microscopy. *Surface Science*, 227(3):246 – 260, 1990.

[52] H. H. Rotermund, W. Engel, M. Kordesch, and G. Ertl. Imaging of spatio-temporal pattern evolution during carbon monoxide oxidation on platinum. *Nature*, 343(6256):355 – 357, 1990.

[53] F. Lovis and R. Imbihl. Self-Organization of Ultrathin Vanadium Oxide Layers on a Rh(111) Surface during a Catalytic Reaction. Part I: A PEEM Study. *The Journal of Physical Chemistry C*, 115(39):19141–19148, 2011.

[54] M. J. Prieto and Th. Schmidt. LEEM and PEEM as Probing Tools to Address Questions in Catalysis. *Catalysis Letters*, 147(10):2487–2497, 2017.

[55] M. J. Prieto, H. W. Klemm, F. Xiong, D. M. Gottlob, D. Menzel, Th. Schmidt, and H.-J. Freund. Water Formation under Silica Thin Films: Real-Time Observation of a Chemical Reaction in a Physically Confined Space. *Angewandte Chemie International Edition*, 2018.

[56] E. Emmez, B. Yang, S. Shaikhutdinov, and H.-J. Freund. Permeation of a Single-Layer SiO_2 Membrane and Chemistry in Confined Space. *The Journal of Physical Chemistry C*, 118(50):29034–29042, 2014.

[57] D. Muñoz-Santiburcio and D. Marx. Nanoconfinement in Slit Pores Enhances Water Self-Dissociation. *Physical Review Letters*, 119(5), 2017.

[58] R. Hasegawa, T. Kurosawa, and T. Yagihashi. Hydrogen Reduction of Germanium Dioxide. *Transactions of the Japan Institute of Metals*, 13(1):39–44, 1972.

[59] R. A. Gardner. The kinetics of silica reduction in hydrogen. *Journal of Solid State Chemistry*, 9(4):336–344, 1974.

[60] E. Bauer. LEEM and UHV-PEEM: A retrospective. *Ultramicroscopy*, 119(0):18 – 23, 2012.

[61] R. Fink, M. R. Weiss, E. Umbach, D. Preikszas, H. Rose, R. Spehr, P. Hartel, W. Engel, R. Degenhardt, R. Wichtendahl, H. Kuhlenbeck, W. Erlebach, K. Ihmann, R. Schlögl, H.-J. Freund, A. M. Bradshaw, G. Lilienkamp, Th. Schmidt, E. Bauer, and G. Benner. SMART: a planned ultrahigh-resolution spectromicroscope for BESSY II. *Journal of Electron Spectroscopy and Related Phenomena*, 84(1-3):231–250, 1997.

[62] Th. Schmidt, H. Marchetto, P. L. Lévesque, U. Groh, F. Maier, D. Preikszas, P. Hartel, R. Spehr, G. Lilienkamp, W. Engel, R. Fink, E. Bauer, H. Rose, E. Umbach, and H.-J. Freund. Double aberration correction in a low-energy electron microscope. *Ultramicroscopy*, 110(11):1358 – 1361, 2010.

[63] Th. Schmidt, A. Sala, H. Marchetto, E. Umbach, and H.-J. Freund. First experimental proof for aberration correction in XPEEM: Resolution, transmission enhancement, and limitation by space charge effects. *Ultramicroscopy*, 126:23 – 32, 2013.

[64] R. M. Tromp, J. B. Hannon, A. W. Ellis, W. Wan, A. Berghaus, and O. Schaff. A new aberration-corrected, energy-filtered LEEM/PEEM instrument. I. Principles and design. *Ultramicroscopy*, 110(7):852–861, 2010.

[65] L. de Broglie. Researches on the quantum theory. *Ann. Phys. (Paris)*, 3(22), 1925.

[66] W. Göpel and M. Henzler. *Oberflächenphysik des Festkörpers*. Vieweg Teubner Verlag, 1994.

[67] Th. Schmidt. private communication.

[68] H. Müller and D. Preikszasand H. Rose. A beam separator with small aberrations. *Journal of Electron Microscopy*, 48(3):191–204, 1999.

[69] D. Preikszas and H. Rose. Correction properties of electron mirrors. *Journal of Electron Microscopy*, 46(1):1–9, 1997.

[70] H. Rose. *Advances in Electron Optics*. Springer Berlin Heidelberg, Berlin, Heidelberg, 2003.

[71] H. Rose and D. Krahl. Electron Optics of Imaging Energy Filters. In *Springer Series in Optical Sciences*, pages 43–149. Springer Berlin Heidelberg, 1995.

[72] Th. Schmidt, U. Groh, R. Fink, E. Umbach, O. Schaff, W. Engel, B. Richter, H. Kuhlenbeck, R. Schlögl, H.-J. Freund, A. M. Bradshaw, D. Preiskszas, P. Hartel, R. Spehr, H. Rose, G. Lilienkamp, E. Bauer, and G. Benner. XPEEM with energy-filtering: Advantages and first results from the SMART project. *Surface Review and Letters*, 09(01):223–232, 2002.

[73] G. Tinti, H. Marchetto, C. A. F. Vaz, A. Kleibert, M. Andrä, R. Barten, A. Bergamaschi, M. Brückner, S. Cartier, R. Dinapoli, T. Franz, E. Fröjdh, D. Greiffenberg, C. Lopez-Cuenca, D. Mezza, A. Mozzanica, F. Nolting, M. Ramilli, S. Redford, M. Ruat, Ch. Ruder, L. Schädler, Th. Schmidt, B. Schmitt, F. Schütz, X. Shi, D. Thattil, S. Vetter, and J. Zhang. The EIGER detector for low-energy electron microscopy and photoemission electron microscopy. *Journal of Synchrotron Radiation*, 24(5):963–974, 2017.

[74] S. Mobilio, F. Boscherini, and C. Meneghini, editors. *Synchrotron Radiation*. Springer Berlin Heidelberg, 2015.

[75] O. Scherzer. Über einige Fehler von Elektronenlinsen. *Zeitschrift für Physik*, 101(9-10):593–603, 1936.

[76] O. Scherzer. Zur Korrigierbarkeit von Elektronenlinsen. *Physik Journal*, 2(5):110–110, 1946.

[77] W. Telieps and E. Bauer. An analytical reflection and emission UHV surface electron microscope. *Ultramicroscopy*, 17(1):57–65, 1985.

[78] J. Kirschner, H. Engelhard, and D. Hartung. An evaporation source for ion beam assisted deposition in ultrahigh vacuum. *Review of Scientific Instruments*, 73(11):3853–3860, 2002.

[79] R. T. Bayard and D. Alpert. Extension of the Low Pressure Range of the Ionization Gauge. *Review of Scientific Instruments*, 21(6):571–572, 1950.

[80] M. P. Seah and W. A. Dench. Quantitative electron spectroscopy of surfaces: A standard data base for electron inelastic mean free paths in solids. *Surface and Interface Analysis*, 1(1):2 – 11, 1979.

[81] G. Ertl and J. Küppers. *Low Energy Electrons and Surface Chemistry*. Wiley-VCH, 1986.

[82] M. A. Van Hove, W. H. Weinberg, and C.-M. Chan. *Low-Energy Electron Diffraction*, volume 6 of *Surface Sciences*. Springer Verlag, Berlin, 2 edition, 1986.

[83] M. Horn von Hoegen. Growth of semiconductor layers studied by spot profile analysing low energy electron diffraction. *Zeitschrift für Kristallographie*, 214(11):591–629 and 684–721, 1999.

[84] Ch. Kittel. *Einführung in die Festkörperphysik*. Gruyter, de Oldenbourg, 2013.

[85] N. W. Ashcroft and D. N. Mermin. *Festkörperphysik*. Gruyter, de Oldenbourg, 2013.

[86] A. Einstein. Über einen die Erzeugung und Verwandlung des Lichtes betreffenden heuristischen Gesichtspunkt. *Annalen der Physik*, 322(6):132–148, 1905.

[87] S. Hüfner. *Photoelectron Spectroscopy*. Springer, 3 edition, 2013.

[88] H. Haken and H. C. Wolf. *Atom- und Quantenphysik*. Springer-Verlag GmbH, 2010.

[89] J. J. Yeh and I. Lindau. Atomic subshell photoionization cross sections and asymmetry parameters: $1 \leqslant Z \leqslant 103$. *Atomic Data and Nuclear Data Tables*, 32(1):1–155, 1985.

[90] J. C. Vickerman and I. S. Gilmore. *Surface Analysis The Principal Techniques*. John Wiley & Sons, 2 edition, 2009.

[91] C. G. Pantano and T. E. Madey. Electron beam damage in Auger electron spectroscopy. *Applications of Surface Science*, 7(1-2):115 – 141, 1981.

[92] T. E. Madey, D. L. Doering, E. Bertel, and R. Stockbauer. Electron- and photon-stimulated desorption: Benefits and pitfalls. *Ultramicroscopy*, 11(2-3):187–198, 1983.

[93] T. E. Madey, D. E. Ramaker, and R. Stockbauer. Characterization of Surfaces Through Electron and Photon Stimulated Desorption. *Annual Review of Physical Chemistry*, 35(1):215–240, 1984.

[94] D. Menzel and R. Gomer. Desorption from Metal Surfaces by Low-Energy Electrons. *The Journal of Chemical Physics*, 41(11):3311–3328, 1964.

[95] P. A. Redhead. INTERACTION OF SLOW ELECTRONS WITH CHEMISORBED OXYGEN. *Canadian Journal of Physics*, 42(5):886–905, 1964.

[96] L. Gregoratti, T. O. Mentes, A. Locatelli, and M. Kiskinova. Beam-induced effects in soft X-ray photoelectron emission microscopy experiments. *Journal of Electron Spectroscopy and Related Phenomena*, 170(1-3):13 – 18, 2009.

[97] C. R. Arumainayagam, H.-L. Lee, R. B. Nelson, D. R. Haines, and R. P. Gunawardane. Low-energy electron-induced reactions in condensed matter. *Surface Science Reports*, 65(1):1 – 44, 2010.

[98] E. Bauer, M. Mundschau, W. Swiech, and W. Telieps. Surface studies by low-energy electron microscopy (LEEM) and conventional UV photoemission electron microscopy (PEEM). *Ultramicroscopy*, 31(1):49–57, 1989.

[99] G. Rupprechter. Surface Science Approach to Heterogeneous Catalysis. In *Surface and Interface Science*, pages 459–528. Wiley-VCH Verlag GmbH & Co. KGaA, 2015.

[100] H.-J. Freund, H. Kuhlenbeck, J. Libuda, G. Rupprechter, M. Bäumer, and H. Hamann. Bridging the pressure and materials gaps between catalysis and surface science: clean and modified oxide surfaces. *Topics in Catalysis*, 15(2/4):201–209, 2001.

[101] G. Pacchioni and H.-J. Freund. Controlling the charge state of supported nanoparticles in catalysis: lessons from model systems. *Chemical Society Reviews*, 2018.

[102] S. J. Tauster. Strong metal-support interactions. *Accounts of Chemical Research*, 20(11):389–394, 1987.

[103] J. A. Venables, G. D. T. Spiller, and M. Hanbücken. Nucleation and growth of thin films. *Reports on Progress in Physics*, 47(4):399–459, 1984.

[104] E. Bauer. Phänomenologische Theorie der Kristallabscheidung an Oberflächen. I. *Zeitschrift für Kristallographie - Crystalline Materials*, 110(1-6), 1958.

[105] E. Bauer. Phänomenologische Theorie der Kristallabscheidung an Oberflächen. II. *Zeitschrift für Kristallographie - Crystalline Materials*, 110(1-6), 1958.

[106] K. W. Kolasinski. *Surface Science*. Wiley John + Sons, 2012.

[107] Thomas Schmidt. *Strukturelle Untersuchungen zur Homoepitaxie auf Pt(111)*. Phd thesis, Universität Hannover, 1994.

[108] Z. Zhang and M. G. Lagally. Atomistic Processes in the Early Stages of Thin-Film Growth. *Science*, 276(5311):377–383, 1997.

[109] G. Ehrlich and F. G. Hudda. Atomic View of Surface Self-Diffusion: Tungsten on Tungsten. *The Journal of Chemical Physics*, 44(3):1039–1049, 1966.

[110] R. L. Schwoebel and E. J. Shipsey. Step Motion on Crystal Surfaces . *Journal of Applied Physics*, 37(10):3682–3686, 1966.

[111] J. W. Evans. Random-deposition models for thin-film epitaxial growth. *Physical Review B*, 39(9):5655–5664, 1989.

[112] J. W. Arblaster. Crystallographic Properties of Ruthenium. *Platinum Metals Review*, 57(2):127–136, 2013.

[113] K. Aika, H. Hori, and A. Ozaki. Activation of nitrogen by alkali metal promoted transition metal I. Ammonia synthesis over ruthenium promoted by alkali metal. *Journal of Catalysis*, 27(3):424–431, 1972.

[114] T. Naota, H. Takaya, and S. Murahashi. Ruthenium-Catalyzed Reactions for Organic Synthesis. *Chemical Reviews*, 98(7):2599–2660, 1998.

[115] J. Levec and A. Pintar. Catalytic wet-air oxidation processes: A review. *Catalysis Today*, 124(3-4):172–184, 2007.

[116] I. Palacio and O. Rodríguez de la Fuente. Methanol decomposition on Ru(0001) during continuous exposure at room temperature. *Surface Science*, 606(15-16):1152–1159, 2012.

[117] J. Assmann, V. Narkhede, N. A. Breuer, M. Muhler, A. P. Seitsonen, M. Knapp, D. Crihan, A. Farkas, G. Mellau, and H. Over. Heterogeneous oxidation catalysis on ruthenium: bridging the pressure and materials gaps and beyond. *Journal of Physics: Condensed Matter*, 20(18):184017, 2008.

[118] C. N. R. Rao, P. Vishnu Kamath, and S. Yashonath. Molecularly adsorbed oxygen on metals: electron spectroscopic studies. *Chemical Physics Letters*, 88(1):13–16, 1982.

[119] K. L. Kostov, M. Gsell, P. Jakob, T. Moritz, W. Widdra, and D. Menzel. Observation of a novel high density 3O(2x2) structure on Ru(001). *Surface Science*, 394(1-3):L138–L144, 1997.

[120] M. Gsell, M. Stichler, P. Jakob, and D. Menzel. Formation and Geometry of a High-Coverage Oxygen Adlayer on Ru(001), the p(2 × 2)-3O Phase. *Israel Journal of Chemistry*, 38(4):339–348, 1998.

[121] M. Lindroos, H. Pfnür, G. Held, and D. Menzel. Adsorbate induced reconstruction by strong chemisorption: Ru(001)p(2x2)-O. *Surface Science*, 222(2-3):451 – 463, 1989.

[122] H. Pfnür, G. Held, M. Lindroos, and D. Menzel. Oxygen induced reconstruction of a close-packed surface: A LEED IV study on Ru(001)-p(2x1)O. *Surface Science*, 220(1):43 – 58, 1989.

[123] C. Stampfl, S. Schwegmann, H. Over, M. Scheffler, and G. Ertl. Structure and Stability of a High-Coverage (1×1) Oxygen Phase on Ru(0001). *Physical Review Letters*, 77(16):3371–3374, 1996.

[124] T. E. Madey, H. A. Engelhardt, and D. Menzel. Adsorption of oxygen and oxidation of CO on the ruthenium (001) surface. *Surface Science*, 48(2):304 – 328, 1975.

[125] L. Li, S. Lu, J. Pan, Z. Qin, Y. Wang, Y. Wang, G. Cao, S. Du, and H. Gao. Buckled Germanene Formation on Pt(111). *Advanced Materials*, 26(28):4820–4824, 2014.

[126] M. Derivaz, D. Dentel, R. Stephan, M.-Ch. Hanf, A. Mehdaoui, P. Sonnet, and C. Pirri. Continuous Germanene Layer on Al(111). *Nano Letters*, 15(4):2510–2516, 2015.

[127] Y.Fukaya, I. Matsuda, B. Feng, I. Mochizuki, T. Hyodo, and S. Shamoto. Asymmetric structure of germanene on an Al(111) surface studied by total-reflection high-energy positron diffraction. *2D Materials*, 3(3):035019, 2016.

[128] J. Yuhara, H. Shimazu, K. Ito, A. Ohta, M. Araidai, M. Kurosawa, M. Nakatake, and G. Le Lay. Germanene Epitaxial Growth by Segregation through Ag(111) Thin Films on Ge(111). *ACS Nano*, 12(11):11632–11637, 2018.

[129] C. Lin, A. Huang, W. Wu Pai, W. Chen, T. Chen, T. Chang, R. Yukawa, C. Cheng, C. Mou, I. Matsuda, T.-C. Chiang, H.-T. Jeng, and S.-J. Tang. Single-layer dual germanene phases on Ag(111). *Physical Review Materials*, 2(2), 2018.

[130] F. Li, W. Wei, X. Lv, B. Huang, and Y. Dai. Evolution of the linear band dispersion of monolayer and bilayer germanene on Cu(111). *Physical Chemistry Chemical Physics*, 19(34):22844–22851, 2017.

[131] P. W. Sutter, J. I. Flege, and E. A. Sutter. Epitaxial graphene on ruthenium. *Nature Materials*, 7(5):406 – 411, 2008.

[132] D. Martoccia, P. R. Willmott, T. Brugger, M. Björck, S. Günther, C. M. Schlepütz, A. Cervellino, S. A. Pauli, B. D. Patterson, S. Marchini, J. Wintterlin, W. Moritz, and T. Greber. Graphene on Ru(0001): A 25x25 Supercell. *Physical Review Letters*, 101:126102, 2008.

[133] H. J. Zhang, B. Lu, X.-S. Wang, F. Hu, H. Y. Li, S. N. Bao, and P. He. Film growth of germanium on Ru(0001) studies by scanning tunneling microscopy. *Physical Review B*, 70(23), 2004.

[134] Y. H. Lu, Y. Jia, H. J. Zhang, B. Song, H. Y. Li, S. N. Bao, and P. He. Adsorption structure of germanium on the Ru(0001) surface. *Applied Surface Science*, 254(2):431–435, 2007.

[135] Y. Lu, Q. Sun, Y. Jia, and P. He. Adsorption and diffusion of adatoms on Ru(0001): A first-principles study. *Surface Science*, 602(14):2502–2507, 2008.

[136] R. Topolnicki and R. Kucharczyk. Early stages of growth of Pb, Sn and Ge on Ru(0001): A comparative density functional theory study. *Thin Solid Films*, 665:123–130, 2018.

[137] W. Wang and R. I. G. Uhrberg. Coexistence of strongly buckled germanene phases on Al(111). *Beilstein Journal of Nanotechnology*, 8:1946–1951, 2017.

[138] E. A. Martínez, J. D. Fuhr, O. Grizzi, E. A. Sánchez, and E. D. Cantero. Growth of Germanene on Al(111) Hindered by Surface Alloy Formation. *The Journal of Physical Chemistry C*, 2019.

[139] M. Švec, P. Hapala, M. Ondráček, P. Merino, M. Blanco-Rey, P. Mutombo, M. Vondráček, Y. Polyak, V. Cháb, J. A. Martín Gago, and P. Jelínek. Silicene versus two-dimensional ordered silicide: Atomic and electronic structure of Si-$(\sqrt{19} \times \sqrt{19})$R23.4 °/Pt(111). *Physical Review B*, 89(20), 2014.

[140] E. E. Krasovskii, J. Höcker, J. Falta, and J. I. Flege. Surface resonances in electron reflection from overlayers. *Journal of Physics: Condensed Matter*, 27(3):035501, 2015.

[141] K. Wandelt, J. Hulse, and J. Küppers. Site-selective adsorption of xenon on a stepped Ru(0001) surface. *Surface Science*, 104(1):212–239, mar 1981.

[142] N. R. Murphy, J. T. Grant, L. Sun, J. G. Jones, R. Jakubiak, V. Shutthanandan, and C. V. Ramana. Correlation between optical properties and chemical composition of sputter-deposited germanium oxide GeO_x films. *Optical Materials*, 36(7):1177–1182, 2014.

[143] A. J. Mc Evoy and W. Gissler. ESCA Spectra and Electronic Properties of Some Ruthenium Compounds. *physica status solidi (a)*, 69(1):K91–K96, 1982.

[144] T. Sugama, N. Carciello, and C. Taylor. Pyrogenic polygermanosiloxane coatings for aluminum substrates. *Journal of Non-Crystalline Solids*, 134(1-2):58–70, 1991.

[145] C. D. Wagner, D. A. Zatko, and R. H. Raymond. Use of the oxygen KLL Auger lines in identification of surface chemical states by electron spectroscopy for chemical analysis. *Analytical Chemistry*, 52(9):1445–1451, 1980.

[146] S. Lizzit, A. Baraldi, A. Groso, K. Reuter, M. V. Ganduglia-Pirovano, C. Stampfl, M. Scheffler, M. Stichler, C. Keller, W. Wurth, and D. Menzel. Surface core-level shifts of clean and oxygen-covered Ru(0001). *Physical Review B*, 63(20), 2001.

[147] A. Santoni, V. R. Dhanak, A. Goldoni, M. Sancrotti, and S. Modesti. High-temperature metallization of the Ge(111) surface detected by photoemission spectroscopy. *Europhysics Letters (EPL)*, 34(4):275–280, 1996.

[148] D. Schmeisser, R. D. Schnell, A. Bogen, F. J. Himpsel, D. Rieger, G. Landgren, and J. F. Morar. Surface oxidation states of germanium. *Surface Science*, 172(2):455 – 465, 1986.

[149] K. Fukutani, Y. Murata, J. Brillo, H. Kuhlenbeck, H.-J. Freund, and M. Taguchi. Electronic structure of a Pt-Ge surface alloy. *Surface Science*, 464(2-3):48–56, 2000.

[150] S. Cahangirov, M. Topsakal, E. Aktürk, H. Şahin, and S. Ciraci. Two- and One-Dimensional Honeycomb Structures of Silicon and Germanium. *Physical Review Letters*, 102(23), 2009.

[151] F. Li, W. Wei, L. Yu, B. Huang, and Y. Dai. Interface effects between germanene and Au(111) from first principles. *Journal of Physics D: Applied Physics*, 50(11):115301, 2017.

[152] S. Endo, O. Kubo, N. Nakashima, S. Iwaguma, R. Yamamoto, Y. Kamakura, H. Tabata, and M. Katayama. $\sqrt{3}\times\sqrt{3}$ germanene on Al(111) grown at nearly room temperature. *Applied Physics Express*, 11(1):015502, 2017.

[153] M. E. Dávila and G. Le Lay. Few layer epitaxial germanene: a novel two-dimensional Dirac material. *Scientific Reports*, 6(1), 2016.

[154] P. Heilmann, K. Heinz, and K. Müller. Temperature dependence of W(100) LEED intensities. *Surface Science*, 89(1-3):84–94, 1979.

[155] M. Henzler. LEED studies of surface imperfections. *Applications of Surface Science*, 11-12:450–469, 1982.

[156] A. L. Lewandowski, S. Tosoni, L. Gura, P. Schlexer, P. Marschalik, W.-D. Schneider, M. Heyde, G. Pacchioni, and H.-J. Freund. From Crystalline to Amorphous Germania Bilayer Films at the Atomic Scale: Preparation and Characterization. *Angewandte Chemie International Edition*, DOI: 10.1002/anie.201903922, 2019.

[157] K. Prabhakaran and T. Ogino. Oxidation of Ge(100) and Ge(111) surfaces: an UPS and XPS study. *Surface Science*, 325(3):263–271, 1995.

[158] M. Lindroos, H. Pfnür, and D. Menzel. Theoretical and experimental study of the unoccupied electronic band structure of Ru(001) by electron reflection. *Phys. Rev. B*, 33:6684–6693, 1986.

[159] K. Okumura, K. Asakura, and Y. Iwasawa. Characterization of GeO_2 Submonolayers on SiO_2 Prepared by Chemical Vapor Deposition of $Ge(OMe)_4$ by EXAFS, FT-IR, and XRD. *Langmuir*, 14(13):3607–3613, 1998.

[160] H. Hosono, Y. Abe, D. L. Kinser, R. A. Weeks, K. Muta, and H. Kawazoe. Nature and origin of the 5 eV band in $SiO_2 : GeO_2$ glasses. *Physical Review B*, 46(18):11445–11451, 1992.

[161] T. L. Barr, M. Mohsenian, and Li Mei Chen. XPS valence band studies of the bonding chemistry of germanium oxides and related systems. *Applied Surface Science*, 51(1-2):71–87, 1991.

[162] M. Delfino, S. Salimian, D. Hodul, A. Ellingboe, and W. Tsai. Plasma cleaned Si analyzedinsituby x-ray photoelectron spectroscopy, secondary ion mass spectrometry, and actinometry. *Journal of Applied Physics*, 71(2):1001–1009, 1992.

[163] S. K. Ray and K. Das. Luminescence characteristics of Ge nanocrystals embedded in SiO_2 matrix. *Optical Materials*, 27(5):948–952, 2005.

[164] H. G. Chew, W. K. Choi, Y. L. Foo, F. Zheng, W. K. Chim, Z. J. Voon, K. C. Seow, E. A. Fitzgerald, and D. M. Y. Lai. Effect of germanium concentration and oxide diffusion barrier on the formation and distribution of germanium nanocrystals in silicon oxide matrix. *Nanotechnology*, 17(8):1964–1968, 2006.

[165] L. Li, H. Tissot, S. Shaikhutdinov, and H.-J. Freund. Transition Metal Induced Crystallization of Ultrathin Silica Films. *Chemistry of Materials*, 29(3):931–934, 2017.

[166] L. Perring, P. Feschotte, and J. C. Gachon. The germanium-ruthenium system. *Journal of Phase Equilibria*, 17(2):101–106, 1996.

[167] H. Li, J. Xiao, Q. Fu, and X. Bao. Confined catalysis under two-dimensional materials. *Proceedings of the National Academy of Sciences*, 114(23):5930–5934, 2017.

[168] S. A. Miners, G. A. Rance, and A. N. Khlobystov. Regioselective control of aromatic halogenation reactions in carbon nanotube nanoreactors. *Chemical Communications*, 49(49):5586, 2013.

[169] Gerhard Ertl. *Reactions at Solid Surfaces*. JOHN WILEY & SONS INC, 2009.

[170] G. Wedler and H.-J. Freund. *Lehr- und Arbeitsbuch Physikalische Chemie*. Wiley VCH Verlag GmbH, 2018.

[171] B. Yao, S. Mandrà, J. O. Curry, S. Shaikhutdinov, H.-J. Freund, and J. Schrier. Gas Separation through Bilayer Silica, the Thinnest Possible Silica Membrane. *ACS Applied Materials & Interfaces*, 9(49):43061–43071, 2017.

[172] J.-H. Jhang and E. I. Altman. Water chemistry on two-dimensional silicates studied by density functional theory and temperature-programmed desorption. *Surface Science*, 679:99–109, 2019.

[173] J. Sauer. Brønsted activity of two-dimensional zeolites compared to bulk materials. *Faraday Discussions*, 188:227–234, 2016.

[174] N. M. Smith, K. Swaminathan Iyer, and B. Corry. The confined space inside carbon nanotubes can dictate the stereo- and regioselectivity of Diels-Alder reactions. *Physical Chemistry Chemical Physics*, 16(15):6986, 2014.

[175] P. Sutter, J. T. Sadowski, and E. A. Sutter. Chemistry under Cover: Tuning Metal-Graphene Interaction by Reactive Intercalation. *Journal of the American Chemical Society*, 132(23):8175 – 8179, 2010.

[176] R. Mu, Q. Fu, L. Jin, L. Yu, G. Fang, D. Tan, and X. Bao. Visualizing Chemical Reactions Confined under Graphene. *Angewandte Chemie International Edition*, 51(20):4856 – 4859, 2012.

[177] P. Feulner and D. Menzel. The adsorption of hydrogen on ruthenium (001): Adsorption states, dipole moments and kinetics of adsorption and desorption. *Surface Science*, 154(2-3):465–488, 1985.

[178] M. J. Prieto et. al. to be published. 2019.

[179] M. I. Buckett, J. Strane, D. E. Luzzi, J. P. Zhang, B. W. Wessels, and L. D. Marks. Electron irradiation damage in oxides. *Ultramicroscopy*, 29(1-4):217–227, 1989.

[180] N. Jiang. Electron beam damage in oxides: a review. *Reports on Progress in Physics*, 79(1):016501, 2015.

[181] F. E. Feiten, H. Kuhlenbeck, and H.-J. Freund. Reducing the V_2O_3(0001) surface through electron bombardment - a quantitative structure determination with I/V-LEED. *Physical Chemistry Chemical Physics*, 18(4):3124–3130, 2016.

[182] X. Yu, E. Emmez, Q. Pan, B. Yang, S. Pomp, W. E. Kaden, M. Sterrer, S. Shaikhutdinov, H.-J. Freund, I. Goikoetxea, R. Wlodarczyk, and J. Sauer. Electron stimulated hydroxylation of a metal supported silicate film. *Physical Chemistry Chemical Physics*, 18(5):3755–3764, 2016.

[183] D. M. Gottlob et. al. to be published. 2019.

[184] R. Włodarczyk, M. Sierka, J. Sauer, D. Löffler, J. J. Uhlrich, X. Yu, B. Yang, I. M. N. Groot, S. Shaikhutdinov, and H.-J.Freund. Tuning the electronic structure of ultrathin crystalline silica films on Ru(0001). *Phys. Rev. B*, 85:085403, 2012.

[185] M. Wang, J.-Q. Zhong, J. Kestell, I. Waluyo, D. J. Stacchiola, J. A. Boscoboinik, and D. Lu. Energy Level Shifts at the Silica/Ru(0001) Heterojunction Driven by Surface and Interface Dipoles. *Topics in Catalysis*, 60(6-7):481–491, 2016.

[186] Mauricio Prieto and Thomas Schmidt. private communication. 2019.

Danksagung

Mein erster und besonderer Dank gilt meinem Doktorvater Prof. Dr. Hans-Joachim Freund für die Ermöglichung und die Unterstüzung für diese Arbeit. Am Fritz-Haber-Institut fand ich einmalige und exzellente wissenschaftliche Möglichkeiten vor. Ich bin dankbar am einmaligen wissenschaftlichen Austausch am FHI und der exzellenten Forschungsatmosphäre partizipieren zu können.

Meinem Zweitgutachter Prof. Dr. Paul Fumagalli möchte ich für die Betreuung und Begutachtung meiner Arbeit danken.

Besonders danken möchte ich Prof. Dr. Dietrich Menzel für die wertvollen fachlichen Diskussionen meiner Arbeit, sowie ausdrücklich für das unermüdliche Korrekturlesen. Sein enormes Wissen war eine Bereicherung für mich.

Einen besonderen Dank möchte ich meinem Arbeitsgruppenleiter Dr. Thomas Schmidt aussprechen, der mir stets mit Rat und Tat zur Seite stand. Seine kritischen Fragen und Anmerkungen haben diese Arbeit voran gebracht. Ich bin dankbar, von seinem großen physikalischen und technischen Wissen lernen zu können.

Bedanken möchte ich mich auch bei den Mitgliedern der Spektro-Mikroskopie Arbeitsgruppe: Dr. Gina Peschel, Dr. Mauricio Prieto, Dr. Daniel Gottlob, Dr. Liviu Tanase, Dr. Francesca Genuzio, Dr. Hagen Klemm, Dr. Eva Madej und Dr. Helder Marchetto. Für die technische Hilfe bedanke ich mich bei Marcel Springer und Stephan Pohl.

Für die wissenschaftlichen Diskussionen danke ich Dr. Markus Heyde und Adrian Lewandowski.

Ich bedanke mich bei der International Max Planck Research School for „Complex Surfaces in Material Sciences“ für die ideelle und finanzielle Unterstützung.

Nicht zuletzt möchte ich meiner Familie und meinen Freunden danken, die mich immer unterstützt haben. Ganz besonders möchte ich meiner Freundin Maike danken, für ihre Unterstützung in einer nicht immer einfachen Zeit.

Vielen Dank!

Curriculum Vitae

Der Lebenslauf ist in der Online-Version aus Gründen des Datenschutzes nicht enthalten.

List of publications

- H. W. Klemm, M. J. Prieto, G. Peschel, A. Fuhrich, E. Madej, F. Xiong, D. Menzel, Th. Schmidt, H.-J. Freund, Formation and Evolution of Ultrathin Silica Polymorphs on Ru(0001) Studied with Combined in Situ, Real-Time Methods, J. Chem. Phys. C, 123(2018) 8244-8255
- D. Kuhness, H. J. Yang, H. W. Klemm, M. Prieto, G. Peschel, A. Fuhrich, D. Menzel, Th. Schmidt, X. Yu, S. Shaikhutdinov, A. Lewandowski, M. Heyde, A. Kelemen, R. Włodarczyk, D. Usvyat, M. Schütz, J. Sauer, H.-J. Freund, A Two-Dimensional 'Zigzag' Silica Polymorph on a Metal Support, J. Am. Chem. Soc. 140 (2018) 6164-6168
- C. Hartmann, G. Sadoughi, R. Félix, E. Handick, H. W. Klemm, G. Peschel, E. Madej, A. B. Fuhrich, X. Liao, S. Raoux, D. Abou-Ras, D. Wargulski, Th. Schmidt, R. G. Wilks, H. Snaith, M. Bär, Spatially Resolved Insight into the Chemical and Electronic Structure of Solution-Processed Perovskites-Why to (Not) Worry about Pinholes, Adv. Mater. Interfaces 5 (2018) 1701420/1-9
- T. Breuer, A. Karthäuser, H. Klemm, F. Genuzio, G. Peschel, A. Fuhrich, Th. Schmidt, G. Witte, Exceptional Dewetting of Organic Semiconductor Films: The Case of Dinaphthothienothiophene (DNTT) at Dielectric Interfaces, ACS Appl. Mater. Interfaces 9 (2017) 8384-8392
- S. P. Cooil, E. A. Mørtsell, F. Mazzola, M. Jorge, S. Wenner, M.T. Edmonds, L. Thomsen, H. W. Klemm, G. Peschel, A. Fuhrich, M. Prieto, Th. Schmidt, J. A. Miwa, R. Holmestad, J. W. Wells, Thermal migration of alloying agents in aluminium, Mater. Res. Express 3 (2016) 116501
- H. Klemm, G. Peschel, E. Madej, A. Fuhrich, M. Timm, D. Menzel, Th. Schmidt, H.-J. Freund, Preparation of silica films on Ru(0001): A LEEM/PEEM study, Surf. Sci. 643 (2016) 45–51
- Z. Balogh, M. Ibrahim, A.B. Fuhrich, B. Parditka, R. Schlesiger, P. Stender, Z. Erdélyi, G. Schmitz, Interfacial Reaction and Phase Growth for Various Metal/Amorphous Silicon System, TMS 2014 Supplemental Proceedings, 2014
- M. Ibrahim, B. Parditka, A. Fuhrich, Z. Balogh, P. Stender, Z. Erdélyi, G. Schmitz, Growth kinetics and interface structure of copper silicides studied by atom probe tomography, Phys. Stat. Sol. C 10 (2013) 1724-1727

Selbstständigkeitserklärung

Hiermit versichere ich, dass ich die vorliegende Arbeit selbstständig verfasst und alle verwendeten Hilfsmittel und Hilfen angegeben habe. Die vorliegende Arbeit wurde nicht in einem früheren Promotionsverfahren eingereicht.

Berlin, den 22.08.2019